UNIVERSITÀ DELLA CALABRIA

UNIVERSITA' DELLA CALABRIA

Dipartimento di Fisica

Dottorato di Ricerca in

Scienze e Tecnologie Fisiche, Chimiche e dei Materiali

CICLO

XXIX

Waves and turbulence in plasmas: from MHD to Vlasov end beyond

Settore Scientifico Disciplinare FIS/03

Coordinatore: Ch.mo Prof. Vincenzo Carbone

Vincenzo Carbone

Supervisore/Tutor: Ch.mo Dott. Francesco Valentini

Francesco Valentini

Dottorando: Dott. Oreste Pezzi

Oreste Pezzi

Ai miei genitori, Brunello e Lia

If the future isn't bright at least it's colorful
so burn the ship come spring

Abstract

This thesis focuses on the physical connection of large, fluid scales with small, kinetic wavelenghts and on the introduction of collisional effects in weakly-collisional plasmas.

In the first part, the Moffatt & Parker problem, namely the collision of two counter-propagating Alfvénic wave packets, has been revisited by means of magnetohydrodynamics (MHD), Hall MHD and hybrid kinetic simulations. The goal of this study was to extend the Moffatt & Parker problem to the realm of kinetic physics and show that, when introducing more complex physical ingredients, the dynamics is quite different with respect to the pure ideal MHD case. When the energy is transferred towards kinetic scales through nonlinear coupling mechanisms, the distribution function is strongly perturbed and departs from local thermodynamical equilibrium. The wave packets interaction has been also characterized in terms of strong and weak turbulence, showing that features explained in terms of both kinds of turbulence theories coexist.

In the second part, a special attention has been devoted to weakly collisional plasma systems, in which kinetic effects and particle collisions coexist and compete in shaping the particle velocity distribution. By means of numerical simulations of relaxation towards equilibrium in presence of the full Landau collisional integral, it has been pointed out that collisionality can be effectively enhanced by the presence of fine velocity structures in the particle distribution function.

However, due to the high computational cost of the Landau integral, simplified collisional operators have been employed to simulate self-consistently the dynamics of weakly-collisional plasmas. In particular, the Dougherty operator has been employed in $1D$–$3V$ phase space configuration ($1D$ in physical space, $3D$ in velocity space) to address the role of electron-electron collisions in the nonlinear regime of electrostatic waves propagation. Finally, with the aim of simulating realistic physical conditions in experiments with plasmas trapped in longitudinal machines, numerical simulations in reduced $1D$–$1V$ phase space have been run to reproduce the process of wave launching in real plasma devices.

The ultimate goal of this work was to support the idea that the competition between kinetic effects, which tend to drive the system away from equilibrium, and collisions, which work to thermalize the plasma, could be the physical ingredient underlying the mechanism of particle heating in weakly collisional systems, such as the solar wind.

Sommario

Questa tesi riguarda l'analisi della connessione delle scale fluide con le scale cinetiche e la descrizione degli effetti collisionali in un plasma debolmente collisionale.

Nella prima parte, il problema di Moffatt & Parker, riguardante la collisione di due pacchetti d'onda Alfvénici, è stato rivisitato mediante simulazioni magnetoidrodinamiche (MHD), Hall MHD e cinetiche. L'obiettivo è di estendere l'analisi del problema a scale cinetiche e mostrare che, quando si introducono effetti più complessi (compressibilità, dispersione, effetti cinetici), la dinamica è molto diversa rispetto al caso MHD. Quando l'energia è trasferita a scale cinetiche mediante accoppiamenti nonlineari, la funzione di distribuzione protonica mostra strutture lontane dall'equilibrio termodinamico. L'interazione dei pacchetti è inoltre caratterizzata in termini di turbolenza forte e debole, mostrando che, a valle dell'interazione dei pacchetti, coesistono caratteristiche spiegabili attraverso entrambe le teorie della turbolenza.

La seconda parte ha riguardato invece la descrizione di un plasma debolmente collisionale, caratterizzato dalla competizione di effetti cinetici e collisioni nel determinare l'evoluzione della funzione di distribuzione particellare. Attraverso simulazioni numeriche di rilassamento verso l'equilibrio in presenza dell'integrale collisionale di Landau, è stato mostrato che la collisionalità può essere effettivamente intensificata dalla presenza di forti gradienti nello spazio delle velocità.

Tuttavia, per l'eccessivo costo computazionale dell'integrale di Landau, sono stati sviluppati alcuni operatori collisionali semplificati al fine di simulare, in modo auto-consistente, la dinamica dei plasmi debolmente collisionali. In particolare l'operatore di Dougherty è stato utilizzato nello spazio delle fasi $1D$–$3V$ (una dimensione nello spazio fisico, tre in velocità) per studiare l'effetto delle collisioni elettrone-elettrone sulla propagazione di onde elettrostatiche nonlineari. Infine, con lo scopo di simulare le condizioni fisiche realistiche ottenute negli esperimenti con plasmi intrappolati in macchine longitudinali, sono state effettuate simulazioni numeriche nello spazio delle fasi ridotto $1D$–$1V$ che riproducono il processo di eccitazione di un'onda nelle macchine a plasma.

Lo scopo ultimo di questo lavoro era di supportare l'idea che la competizione tra gli effetti cinetici, che tendono a guidare il sistema lontano dall'equilibrio, e le collisioni, che termalizzano il plasma, potrebbe essere l'ingrediente fisico alla base dei meccanismi di riscaldamento delle particelle in un sistema debolmente collisionale, come, ad esempio, il vento solare.

Contents

Introduction

The plasma represents one of the most captivating and, at the same time, common physical systems in the Universe. Since the last Century, several efforts have been devoted to analyze plasmas in order to understand the dynamics of natural systems - such as the inner matter of the stars or the solar wind - or for reproducing the nuclear fusion in laboratory devices for engineering purposes.

Despite some studies recently focused on the presence of quantum effects, plasmas are usually treated as classical gases, composed by a consistent part of ionized particles (electrons and ions). Within this framework, the particles motion is affected by electromagnetic fields through the Lorentz force, but particles contemporaneously modify electromagnetic fields through the sources terms (i.e. charges and currents) of the Maxwell equations. This last aspect, the so–called *self-consistency*, introduces a certain degree of complexity in modeling plasmas. For example, the coupling of charged particles and fields allows the system to exhibit some collective effects such as waves and instabilities. Particles are also correlated due to the presence of microscopical interaction, i.e. collisions, which - as we will discuss in detail - complicates the analysis of the plasma dynamics. Moreover, any plasma model shows the presence of strong nonlinearities in the characteristic equations, thus leaving the door open to a huge branch of nonlinear physics phenomena such as the propagation and the interaction of nonlinear waves or the onset of turbulent flows. Ultimately, the presence of turbulence in plasmas draws a subtle line that connects the study of a *per se* difficult physical system like the plasma with the turbulence, which is one of the most historically analyzed but still not completely understood phenomenon.

This huge physical complexity reduces the possibility of deriving analytical results to few simple cases while, for a deeper comprehension, a numerical approach is mandatory. In this perspective, numerous methods have been developed to study plasmas through a numerical approach, that allowed to achieve significant improvements in understanding the system dynamics. In several cases, numerical simulations have predicted results later confirmed by means of laboratory experiments or through *in-situ* spacecraft measurements, thus reinforcing the role of numerical simulations as valid tools to lead scientific discoveries in plasma physics.

However, the physical complexity is also reflected in the numerical description of the system. Indeed, even though nonlinearities recovered in the equations can be taken into account easier numerically than analytically, one should also remember that the introduction of nonlinearities - often associated with the energy transfer towards small scales - raises important numerical issues related to the adopted resolution and to the computational cost of numerical simulations.

From this point of view, it is important to review the methods usually employed to model plasmas - within the "mean-field" assumption - by also highlighting their computational weight. The different approaches correspond to a description which is appropriate for a particular range of scales (frequencies and wavevectors). At the lowest frequencies, ions and electrons are locked together by electrostatic forces and behave like an electrically conducting fluid; this is the regime of the magnetohydrodynamics (MHD). Historically the MHD represents one of the first attempts to model plasma and assumes that i) plasma is a neutral conducting fluid where collisions are sufficiently strong to maintain a local thermodynamical equilibrium, i.e the particle velocity distribution function shape is close to the equilibrium Maxwellian, and ii) the fluid is coupled to the magnetic field through the induction equation. This model is still widely adopted to analyze plasmas at large scales. Several phenomenologies have been developed to study the features of the MHD turbulence [1, 2, 3, 4, 5, 6, 7, 8, 9, 10, 11, 12, 13, 14] with a particular attention to applications to the solar wind, that is a low-density, high-temperature plasma which flows from the Sun in the heliosphere and

is strongly turbulent. Several extension of the MHD approach have been proposed to include other physical ingredients which occur at smaller scales such as the Hall correction (HMHD) [15, 16, 17]. All these fluid models have a similar computational cost, that is proportional to N^3, being N the number of gridpoints along each spatial direction. At somewhat higher frequencies, electrons and ions can move relatively to each other, behaving like two separate and inter-penetrating fluids: this is the two-fluid regime, whose computational cost is also proportional to N^3.

However, solar wind *in-situ* measurements revealed much complex features which go beyond the fluid treatment. Indeed, once the energy is transferred by turbulence towards smaller scales near the ion inertial lengths, kinetic physics signatures are often observed [12, 18, 19, 20]. Collisions are in general weak and wave-particle interactions and turbulence mechanisms tend to modify the particle VDF shape, which displays a strongly distorted out-of-equilibrium profile characterized by the presence of non-Maxwellian features (temperature anisotropies, beams, rings-like structures etc. etc.) [21, 22, 23, 24, 25]. Numerous kinetic models have been developed to understand the dynamics at such scales [26, 27, 28, 29, 30, 31, 32, 33, 34, 35, 36, 37]. Most of these models are collisionless: collisions are assumed to be far too weak to produce any significant effect on the plasma dynamics and the plasma obeys the Vlasov equation.

We will later come back to the role of collisions in weakly collisional plasmas, since this point deserves - in our opinion - a separate discussion. It is worth to highlight instead the computational cost of the collisionless models. We would also point out that, historically, two main families of numerical approaches have been developed to integrate the Vlasov equation: the Particle-In-Cell (PIC) [38, 39] and the Eulerian (HVM) [40, 41] algorithms. The latter methods directly integrate the Vlasov equation, while the former solve the characteristics equations of the Vlasov equation for an ensemble of quasi-particles. PIC methods have been widely adopted since their implementation is relatively straightforward and the requested memory is not huge. However they suffer the presence of a statistical noise due to the finite number of quasi-particles. Indeed, it is necessary to "count" the quasi-

particles in a discretized phase space for evaluating moments of the distribution function on a spatial grid, thus introducing the noise which especially affects the dynamics at small scales. On the other hand, Eulerian Vlasov codes are noise-free but their implementation is more difficult and, since the full distribution function is evolved in phase space, the memory requirements are significantly larger than for PIC. Recently different methods have been also proposed to investigate the plasma dynamics [42, 43, 44, 45, 46, 47].

Focusing on collisionless Eulerian kinetic approaches, going from large to small scales, one initially finds the hybrid kinetic models, which are successfully adopted to model the range of scales around the proton inertial scale. These models assume that protons are kinetic and their Vlasov equation is numerically integrated; electrons are instead considered as a background fluid that comes into play only in the Ohm's law for the electric field. The computational cost for solving the full six-dimensional phase space (three dimensions in physical space, three dimensions in velocity space) is about N^6, being N the number of gridpoints along a generic phase space direction. This computational cost currently represents the present limit which can be achieved through modern HPC clusters and the resolution of such simulations is often limited by the memory capacity. Then, when one approaches the electron scales, collisionless fully kinetic simulations, which solve the Vlasov equation for both species, are needed. The computational cost of such simulations is always about N^6 and the required memory is only slightly bigger (a factor 2) compared to the one of hybrid methods. However, describing electrons scales by maintaining a realistic mass ratio implies that these simulations should have an enough high resolution and also a very small time step. Based on these considerations, we may argue that only with the next generation of HPC clusters these simulations will be affordable.

Let us discuss now the importance of collisions and the complications that this physical effect introduces in the system description. The collisionless assumption, often adopted for analyzing plasmas with high temperature and low density, is justified with the fact that the particles mean free path is comparable with the plasma macroscopic length scales [12]. However, in order to show that collisions can be neglected, one usually assumes that

the shape of the particle VDF is close to Maxwellian [22, 23, 24, 48]. In principle, this could be a problem for weakly-collisional turbulent media such as the solar wind, where kinetic physics strongly distort the particle VDFs [21, 22, 23, 24, 25, 29, 30, 31, 33, 35, 41].

For such systems, where kinetic effects compete with the presence of collisions which tend to restore the thermal equilibrium, collisional effects are usually introduced through a "collisional operator" at the right-hand side of the Vlasov equation. These operators often include derivatives in velocity space, therefore the presence of strong gradients and non-Maxwellian features in the velocity distribution function may enhance the effects of collisions [49]. We would also highlight that collisions are the unique mechanism, from a thermodynamic point of view, able to produce irreversible heating in accordance to the H theorem and, hence, to dissipate energy. Therefore, to properly describe such scenarios or to analyze laboratory plasmas, where collisionality is instead significant [50, 51], collisions should be taken into account in the plasma description. However, it is extremely difficult to handle collisions: the presence of velocity space derivatives and multi-dimensional integrals in the collisional operators significantly increases their computational complexity [52, 53, 54, 55, 56]. For example, by considering the Landau operator - which represents one of the most "natural" collisional operators (it can be derived by the Liouville theorem) and choosing the full $3D$–$3V$ phase space (three dimensions in physical space and three dimensions in velocity space), the computational cost would be proportional to N^9 (a three dimensional integral must be computed for each point of the grid). Nowadays such simulations cannot be afforded and only approximated models (reduced phase space or simplified operators) can be adopted [57, 58, 59, 60, 61, 62, 63, 64].

This thesis is composed by two main parts which respectively focus on the connection of large, fluid scales with small, kinetic ones and on the introduction of collisional effects in plasmas. In Part I, the well-known problem of the interaction of two colliding Alfvén wave packets is revisited by means of MHD, HMHD and hybrid kinetic simulations. The aim of this part is to extend the Moffatt & Parker problem to the realm of kinetic physics and exhibit that, when one introduces more complex physical ingredients, the dy-

namics becomes quite different with respect to the pure MHD treatment. It is shown that when the energy is transferred towards kinetic scales, the distribution function is strongly perturbed and exhibits an out-of-equilibrium shape. Moreover the wave packets interaction is investigated in terms of strong and weak turbulence and it is found that features explained in terms of both kinds of turbulence theory coexist. Then, in Part II, we focus on the study of collisions in plasmas. We first show, by modeling collisions through the fully nonlinear Landau operator, that the collisionality is effectively enhanced by the presence of strong gradients in the particle distribution function. In fact, fine structures are dissipated much faster than other global quantities as temperature anisotropies. Nonlinearities present in the collisional operator are also significant to give to collisions the proper importance in terms of characteristic times associated with the dissipation of such structures. However, since the Landau operator is too demanding from a computational cost point of view, we describe the dynamics of weakly-collisional plasmas by means of self-consistent collisional simulation being collisions modeled with simplified collisional operators. In particular, by retaining a three-dimensional velocity space, we model collisions through the Dougherty operator [58, 59] and we establish a successfully comparison with the Landau operator; this allows to perform self-consistent simulations in the $1D$–$3V$ phase space concerning the nonlinear regime of electrostatic waves in presence of electron-electron collisions. Finally, we restrict to the $1D$–$1V$ phase space and we describe i) the problem of the initial state recurrence in a weakly collisional plasma, showing that collisions cannot in general prevent numerical recurrence without affecting the physical solution; ii) the waves launching mechanism commonly adopted in laboratory plasmas, showing that secondary waves branch can be generated at arbitrary phase speeds if the driver perturbs the distribution function close to such velocity. However collisions quickly dissipate these fluctuations.

Part I

The Parker-Moffatt problem as a case study from fluid to kinetic scales

In this first part of the thesis we revisit the well-known problem concerning the interaction of two Aflvénic wave packets, already approached by Moffatt [5] and Parker [6] in the late Seventies. Our principal aim is to extend the analysis from the ideal incompressible MHD treatment to more complex plasma scenarios and, hence, to show that, when one moves beyond the MHD, numerous intriguing features are recovered as the result of the presence of other physical effects such as compressibility, dispersion and kinetic physics.

One should also bear in mind that the interaction of oppositely propagating large amplitude incompressible Alfvénic wave packets represents a familiar perspective on the hydromagnetic description of astrophysical and laboratory plasma turbulence [3, 4]. Indeed, various nonlinear phenomenologies are built on this paradigm [7, 8, 9, 10, 11, 13, 65, 66, 67, 68, 69]. The relevance of this phenomenon is due to the fact that Alfvénic perturbations represent the main component of fluctuations in natural plasmas, as directly measured in the fast streams of solar wind [12, 70] and inferred in the solar corona by remote sensing observations [71, 72, 73]. Therefore the interaction between oppositely propagating Alfvénic packets can be considered as a sort of "building block" of nonlinear phenomena taking place in incompressible MHD turbulence. An essential feature is that large amplitude perturbations in which velocity $\mathbf{u}$ and magnetic field $\mathbf{b}$ fluctuations are Alfvénically correlated, i.e. either $\mathbf{u} = (c_A/B_0)\mathbf{b}$ or $\mathbf{u} = -(c_A/B_0)\mathbf{b}$ (where c_A and B_0 are uniform background Alfvén velocity and magnetic field, respectively), are exact stable solutions to the equations of incompressible magnetohydrodynamics (MHD) [1, 2]. Hence, to induce nonlinear couplings among the fluctuations and to excite turbulence, it is necessary to simultaneously consider magnetic fluctuations $\mathbf{b}$ and velocity fluctuations $\mathbf{u}$ that have an arbitrary sense of correlation. This may be accomplished by superposing the two senses of correlation, in Alfvén units, $\mathbf{u} = +(c_A/B_0)\mathbf{b}$ and $\mathbf{u} = -(c_A/B_0)\mathbf{b}$. One thread emerging from this concerns the analysis of colliding wave packets to reveal properties of the MHD turbulence spectrum [4].

A different emphasis was given by Moffatt [5] and Parker [6]. Both of these treatments analyzed the collision of large amplitude incompressible, ideal

Alfvén wave packets noting that nonlinear interaction and mutual distortion of the wave packets are limited to the span of time during which they spatially overlap. Both *Moffatt* and *Parker* argued that the packets eventually separate and propagate once again undisturbed without further interactions.

The present part of this thesis addresses two questions that arise when trying to apply this physical insight to high temperature extraterrestrial plasmas such as the solar wind, where such large amplitude Alfvénic fluctuations are routinely observed [70], or solar corona, where the interaction of Alfvénic wave packets is thought to occur [71, 72]. First, compressibility, dispersion and kinetic plasma effects are likely to be important in space applications, and we ask if these give rise to significant departures from the the Parker-Moffatt scenario. Second, we ask whether the proposed separation of the packets after collision is realized as envisioned, or if a wake of non-propagating disturbances might remain after very long times. We address these specific questions using a compressible MHD model, a compressible Hall MHD model and two hybrid Vlasov models.

Beyond the assumption of incompressibility, we may anticipate genuinely compressible, dispersive and kinetic effects that warrant examination in the large amplitude wave packets collision problem. In the solar wind for example, many intervals, especially within 1 AU [74] or at high latitudes [75], are highly Alfvénic, but even within such intervals there are mixtures of Elsässer amplitudes, small density variations, and a small parallel variance, as in the well-quoted "5:4:1" variance ratio reported by [70]. There have also been reports of interplanetary magnetosonic wave packets interaction [76], while the great power-law in the interstellar medium [77] is associated with electron density fluctuations that may be either propagating or non-propagating [78]. Furthermore in plasmas such as the solar wind, at smaller scales near the ion inertial scale, one expects kinetic properties [19] such as spectral steepening [12], dispersive wave effects [18, 20, 79] of both Kinetic Alfvén Wave and whistler types, along with temperature anisotropy, beams and other distortions of the proton velocity distribution function (VDF) [21, 29, 30, 33, 35]. These complications place the problem of collisions of Alfvén wave packets in a much more complex framework.

In dealing with low Mach number quasi-incompressible fluid or MHD models, either in numerical simulations [80, 81, 82], applications [8, 71], or in analytical theory [83, 84], one routinely deals with two significant properties: first, the dominant quadratic couplings are of the form $\mathbf{k} = \mathbf{p} + \mathbf{q}$, transferring energy into (or from) Fourier mode with wave-vector $\mathbf{k}$ due to nonlinear interactions with modes at wave-vectors $\mathbf{p}$ and $\mathbf{q}$. One concludes that in general (unless, e.g., all excited wave vectors are co-linear) one expects excitations to spread rapidly among many wave-vectors, a process that over time can produce complex mixing and turbulent flows. Second, incompressible MHD nonlinear evolution proceeds as $\partial z_i^+/\partial t \sim -z_j^- \nabla_j z_i^+$ and $\partial z_i^-/\partial t \sim -z_j^+ \nabla_j z_i^-$ in terms of Elsässer variables $z_j^\pm = u_j \pm b_j$ (jth components of velocity field u_j and magnetic field b_j in Alfvén speed units), thus allowing the immediate conclusion that nonlinear couplings vanish unless the Elsässer fields $\mathbf{z}^+$ and $\mathbf{z}^-$ have nonzero overlap somewhere in space.

A similar problem, namely, the interaction between non-localized moderate amplitude Alfvén waves at spatial scales comparable with the ion inertial length, has been approached within the weak turbulence framework [13] and gyro-kinetic numerical simulations [69] as well as laboratory experiments [85, 86, 87] have been performed. This approach, based on the assumption of small-amplitude fluctuations, describes turbulence in terms of nonlinear couplings among waves, each belonging to a well-defined propagating mode and keeping its own properties, like the dispersion relation. The theory of weak turbulence in plasmas have been widely studied within MHD [66, 68], including dispersive effects [16] and also for high-frequency waves [88, 89, 90]. Strong and weak turbulence theories can be considered somehow complementary [67, 91], and there is a debate on the applicability of a "wave approach" to describe, for instance, turbulence in the solar wind [92, 93, 94, 95, 96, 97]. These properties not only provide motivation for the Alfvén wave packet collision problem, but also enter into some of its complexity as an elementary interaction that generates turbulence.

The present part of this thesis is divided as follows. In Chapter 1 we revisit the Parker-Moffatt problem by focusing on some global “fluid”-like diagnostics which allow to identify which features are introduced moving

beyond the ideal MHD treatment. The MHD evolution revisits the theoretical insights described by Moffatt, Parker, Kraichnan, Chandrasekhar and Elsässer in which the oppositely propagating large amplitude wave packets interact for a finite time, initiating turbulence. The extension to include compressive and kinetic effects maintains the gross characteristics of the simpler classic formulation, but also reveals intriguing features. The physical effects taken into account in the more realistic simulations play a significant role. After the wave packets collision, the complexity of the structures seems to suggest that, probably, wave packets may remain also connected after their interaction. Moreover, the comparison of four different models which evolve the same initial condition contribute to the spirit of "Turbulence Dissipation Challenge" that has been recently discussed in the space plasma community [98].

In Chapter 2 we focus on two features recovered in the Eulerian Vlasov-Maxwell simulation, which is noise-free compared to the PIC simulation. We report evidences of the presence of non-Maxwellian signatures during the wave packets evolution and interaction. Regions characterized by strong temperature anisotropies and nongyrotropies are recovered and the proton distribution function displays a beam along the direction of the local magnetic field, similar to some recent observations of the solar wind [76]. Moreover, by analyzing the features of the turbulence produced by the interaction of two colliding Alfvénic wave packets, we find that weak and strong turbulence scenarios seem to coexist. The wave-like approach, based on the analysis of polarization and correlations, still helps in the characterization of some low-energy fluctuations. However, several signatures of a strong turbulence regime are also recovered. Blurred $\omega - k$ relations are found instead of well-defined dispersion relations, along with a tendency to build up $\omega = 0$ structures, typical of a strong turbulence regime.

Chapter 1

Revisiting a classic: the Parker-Moffatt problem

In this Chapter we revisit the Parker-Moffatt problem by focusing on some global "fluid"-like diagnostics which allow to identify the features introduced when departing from the ideal MHD treatment. In particular, we describe how the scenario is modified by the presence of compressible, dispersive and kinetic effects. During the wave packets interaction, as prescribed by *Parker & Moffatt*, nonlinear coupling processes cause the magnetic energy spectra to evolve towards isotropy, while energy is transferred towards smaller spatial scales. The new ingredients introduced with the HMHD and kinetic simulations play a significant role and several quantities evolve differently with respect to the MHD evolution. We also anticipate that the complexity of structures produced by nonlinear interactions in the HMHD and HVM cases makes difficult to determine whether the wave packets actually attain a full separation after the collision.

We also examine this basic problem by means of a hybrid Particle-in-Cell simulation (HPIC), which allows comparison of two different numerical approaches (HVM and HPIC), which refer to the same physical model. We may anticipate that, in the HPIC case, the system dynamics at small scales is affected by the presence of particles thermal noise and only the large spatial scales features are discretely recovered during the evolution of the two wave

packets.

The structure of the Chapter is the following. In Section 1.1 the numerical models we adopted for the analysis are described in detail, then in Section 1.2 the simulations are analyzed. Finally, we summarize the results in Section 1.3. Results shown here have been collected in two scientific papers recently published in *The Astrophysical Journal* [14] and *Journal of Plasma Physics* [99].

1.1 Models and Approach

For problems such as the one we focus here on, the system dimensionality is crucial: in fact, a proper description should consider a three-dimensional physical space (i.e. three-dimensional wave vectors), where both parallel and perpendicular cascades are taken into account [100, 101, 102]. However, dynamical range of the spatial scales (wave numbers) represented in the model is equally important to capture nonlinear couplings during the wave packet interaction. Furthermore, performing a kinetic Eulerian hybrid Vlasov-Maxwell simulation in a full $3D$–$3V$ phase space retaining a good spatial resolution is too demanding for the present High Performance Computing capability. Given that several runs are required to complete a study such as the present one, a fully $3D$ approach would be prohibitive. Therefore we restrict to the case of a $2.5D$ physical space, where vectorial fields are three-dimensional but their variations depend only on two spatial coordinates (x and y). The HVM model has also a three dimensional velocity space grid. It is worth noting that $2.5D$ captures the qualitative nature of many processes very well and it allows for a large system size, that, in turn, ensures a large Reynolds number; however there might be some quantitative differences for some processes [103, 104, 105].

The fluid models considered here are MHD and Hall MHD, whose dimen-

sionless equations are:

$$\partial_t \rho + \nabla \cdot (\rho \mathbf{u}) = 0 \tag{1.1}$$

$$\partial_t \mathbf{u} + (\mathbf{u} \cdot \nabla)\mathbf{u} = -\frac{\tilde{\beta}}{2\rho}\nabla(\rho T) + \frac{1}{\rho}\left[(\nabla \times \mathbf{B}) \times \mathbf{B}\right] \tag{1.2}$$

$$\partial_t \mathbf{B} = \nabla \times \left[\mathbf{u} \times \mathbf{B} - \frac{\tilde{\epsilon}}{\rho}(\nabla \times \mathbf{B}) \times \mathbf{B}\right] \tag{1.3}$$

$$\partial_t T + (\mathbf{u} \cdot \nabla)T + (\gamma - 1)T(\nabla \cdot \mathbf{u}) = 0 \tag{1.4}$$

In Eqs. (1.1)–(1.4) spatial coordinates $\mathbf{x} = (x, y)$ and time t are respectively normalized to $\tilde{L}$ and $\tilde{t}_A = \tilde{L}/\tilde{c}_A$. The magnetic field $\mathbf{B} = \mathbf{B}_0 + \mathbf{b}$ is scaled to the typical magnetic field $\tilde{B}$, while mass density ρ, fluid velocity $\mathbf{u}$, temperature T and pressure $p = \rho T$ are scaled to typical values $\tilde{\rho}$, $\tilde{c}_A = \tilde{B}/(4\pi\tilde{\rho})^{1/2}$, $\tilde{T}$ and $\tilde{p} = 2\kappa_B\tilde{\rho}\tilde{T}/m_p$ (being κ_B the Boltzmann constant and m_p the proton mass), respectively. Moreover, $\tilde{\beta} = \tilde{p}/(\tilde{B}^2/8\pi)$ is a typical value for the kinetic to magnetic pressure ratio; $\gamma = 5/3$ is the adiabatic index and $\tilde{\epsilon} = \tilde{d}_p/\tilde{L}$ (being $\tilde{d}_p = \tilde{c}_A/\tilde{\Omega}_{cp}$ the proton skin depth) is the Hall parameter, which is set to zero in the pure MHD case. Details about the numerical algorithm can be found in [106, 107].

On the other hand, hybrid Vlasov-Maxwell simulations have been performed by using two different numerical codes: an Eulerian hybrid Vlasov-Maxwell (HVM) code [40] and a hybrid Particle-in-cell (HPIC) code [27]. For both cases protons are described by a kinetic equation and electrons are a Maxwellian, isothermal fluid. In the Vlasov model, an Eulerian representation of the Vlasov equation for protons is numerically integrated. In PIC method, the distribution function is Monte-Carlo discretized and the Newton-Lorentz equations are updated for the "macro-particles". Electromagnetic fields, charge density and current density are computed on a spatial grid [38, 108].

Dimensionless HVM equations are:

$$\partial_t f + \mathbf{v}\cdot\nabla f + \frac{1}{\tilde{\epsilon}}\left(\mathbf{E}+\mathbf{v}\times\mathbf{B}\right)\cdot\nabla_{\mathbf{v}} f = 0 \tag{1.5}$$

$$\mathbf{E} - \tfrac{m_e\tilde{\epsilon}^2}{m_p}\Delta\mathbf{E} = -\mathbf{u_e}\times\mathbf{B} - \frac{\tilde{\epsilon}\tilde{\beta}}{2n}\left(\nabla P_e - \frac{m_e}{m_p}\nabla\cdot\mathbf{\Pi}\right) + \frac{m_e}{m_p}\left[\mathbf{u}\times\mathbf{B} + \frac{\tilde{\epsilon}}{n}\nabla\cdot\left(n\left(\mathbf{uu}-\mathbf{u_e u_e}\right)\right)\right] \tag{1.6}$$

$$\tfrac{\partial\mathbf{B}}{\partial t} = -\nabla\times\mathbf{E} \quad ; \quad \nabla\times\mathbf{B} = \mathbf{j} \tag{1.7}$$

where $f = f(\mathbf{x},\mathbf{v},t)$ is the proton distribution function. In Eqs. (1.5)–(1.7), velocities $\mathbf{v}$ are scaled to the Alfvén speed $\tilde{c}_A$, while the proton number density $n = \int f\, d^3v$, the proton bulk velocity $\mathbf{u} = n^{-1}\int \mathbf{v} f\, d^3v$ and the proton pressure tensor $\Pi_{ij} = n^{-1}\int (v-u)_i\,(v-u)_j f\, d^3v$, obtained as moments of the distribution function, are normalized to $\tilde{n} = \tilde{\rho}/m_p$, $\tilde{c}_A$ and $\tilde{p}$, respectively. The electric field $\mathbf{E}$, the current density $\mathbf{j} = \nabla\times\mathbf{B}$ and the electron pressure P_e are scaled to $\tilde{E} = (\tilde{c}_A\tilde{B})/c$, $\tilde{j} = c\tilde{B}/(4\pi\tilde{L})$ and $\tilde{p}$, respectively. Moreover, electron inertia effects have been considered in Ohm's law to prevent numerical instabilities (being $m_e/m_p = 0.01$, where m_e is the electron mass, and $\mathbf{u_e} = \mathbf{u} - \tilde{\epsilon}\mathbf{j}/n$), while no external resistivity η is introduced. A detailed description of the HVM algorithm can be found in [40, 106, 107]. On the other hand, the hybrid PIC run has been performed using the P3D hybrid code [39] and all the numerical and physical parameters are the same as the HVM run. The P3D code has been extensively used for reconnection and turbulence (See, for example, Refs. [27, 109]).

In both classes of performed simulations (fluid and kinetic), the spatial domain $D(x,y) = [0, 8\pi]\times[0, 2\pi]$ is discretized with $(N_x, N_y) = (1024, 256)$ in such a way that $\Delta x = \Delta y$ and spatial boundary conditions are periodic. For the HVM run, the velocity space is discretized with a uniform grid with 51 points in each direction, in the region $v_i = [-v_{max}, v_{max}]$ (being $v_{max} = 2.5\tilde{c}_A$) and velocity domain boundary conditions assume $f = 0$ for $|v_i| > v_{max}$ $(i = x, y, z)$; while, in the HPIC case, the number of particles per cell is 400. Moreover $\beta_p = 2v_{th,p}^2/\tilde{c}_A^2 = \tilde{\beta}/2 = 0.5$ (i.e. $v_{max} = 5v_{th,p}$), $\tilde{\epsilon} = \tilde{d}_p/\tilde{L} = 9.8\times10^{-2}$, $k_{d_p} = \tilde{\epsilon}^{-1} \simeq 10$ and $k_{d_e} = \sqrt{m_p/m_e}\times\tilde{\epsilon}^{-1} \simeq 100$.

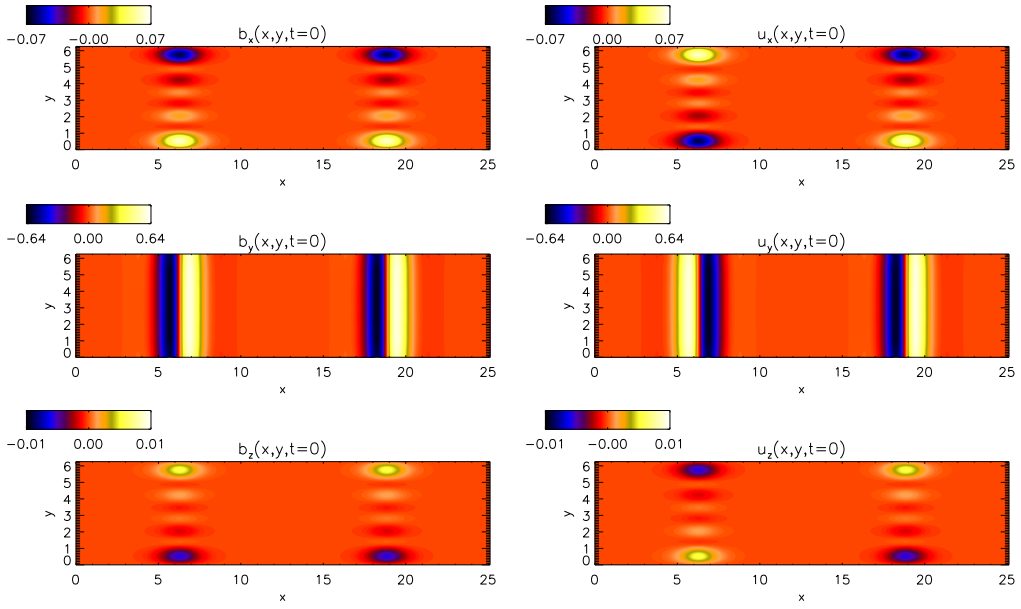

Figure 1.1: (Color online) Contour plots of the initial perturbations. Left and right columns refer respectively to **b** and **u**. Top, central and bottom rows indicate the x, y and z components of the perturbations.

The background magnetic field is mainly perpendicular to the $x-y$ plane: $\mathbf{B}_0 = B_0(\sin\theta, 0, \cos\theta)$, where $\theta = \cos^{-1}\left[(\mathbf{B_0}\cdot\hat{\mathbf{z}})/B_0\right] = 6°$ and $B_0 = |\mathbf{B_0}|$.

In the initial conditions, ions are isotropic and homogeneous (Maxwellian velocity distribution function in each spatial point) for both kinetic simulations. Then, large amplitude magnetic **b** and bulk velocity **u** perturbations are introduced. Density perturbations are not imposed, which implies nonzero total pressure fluctuations. Initial perturbations consist of two Alfvénic wave packets with opposite velocity-magnetic field correlation. The packets are separated along x and, since $B_{0,x} \neq 0$, they counter-propagate. The nominal time for the collision, evaluated with respect to the center of each wave packet, is $\tau \simeq 58.9$.

The magnetic field perturbation **b** has been created by initializing energy in the first four wave-numbers in the y direction while, due to the x spatial localization (enforced by projection), many wave-numbers along x are excited initially. Then, a small $b_z(x,y)$ component has been introduced in such a way that the transverse condition, $\mathbf{B_0}\cdot\mathbf{b} = 0$, is hold in each domain point.

Finally, the velocity field perturbation $\mathbf{u}$ is generated by imposing that $\mathbf{u}$ and $\mathbf{b}$ are correlated (anti-correlated) for the wave packet which moves against (along) the magnetic field B_{0x}. The contour plots of the initial condition are shown in Fig. 1.1, where left (right) column refers to $\mathbf{b}$ ($\mathbf{u}$) perturbations. The intensity of the perturbation is $\langle b \rangle_{rms}/B_0 = 0.2$, therefore the Mach number is $M_s = \langle u \rangle_{rms}/v_{th,p} = 0.4$. The intensity of fluctuations with respect to the in-plane field B_{0x} is quite strong, with a value of about 2. It is worth to note that the inverse of the intensity of the fluctuations with respect to the in-plane magnetic field is related to the parameter τ_{NL}/τ_{coll}, where τ_{NL} is the characteristic nonlinear time and τ_{coll} is the characteristic collision time. If $\tau_{NL}/\tau_{coll} \ll 1$, several nonlinear times occur in a single collision and wave packets can be significantly perturbed by nonlinear effects. On the other hand, if $\tau_{NL}/\tau_{coll} > 1$, many collisions are necessary to strongly distort wave packets. By evaluating $\tau_{NL} \simeq \Delta/u$ (wave packet width Δ, perturbations amplitude u) and $\tau_{coll} \simeq \Delta/V$ (in-plane Alfvén propagation speed $V \simeq 0.1 c_A$), it turns out that $\tau_{NL}/\tau_{coll} \simeq 0.5$. Therefore our simulations stand in a parameter range where nonlinear effects can be such important that a strong turbulence scenario may be present.

1.1.1 Discussion of the Initial Conditions

The imposed initial perturbations correspond to two large amplitude Alfvén wave packets in the sense that magnetic and velocity perturbations are fully correlated in each packet, and the packets are separated in space. With zero density variation, a weak in-plane uniform magnetic field, and a relatively strong out of plane uniform magnetic field, this initial condition is one for which the reasoning of Moffatt and Parker discussed above would be applicable in the context of an incompressible model.

In addition, the initial data also exactly satisfy the transversality condition $\mathbf{B_0} \cdot \mathbf{b} = 0$, which in linear compressible MHD would correspond to the Alfvén eigenmode, if indeed the amplitude were infinitesimal. Here the amplitude is large, so small amplitude theory is unlikely to be relevant to the nonlinear evolution. Furthermore, the condition of the proper Alfvén

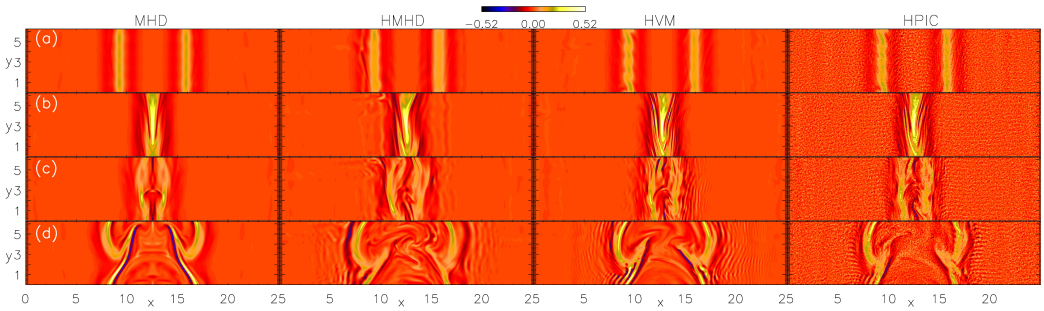

Figure 1.2: (Color online) Contour plots of the out of plane component of the current density $j_z(x, y)$ at several time instants $t = 29.5$ (a), $t = \tau = 58.9$ (b), $t = 70.7$ (c) and $t = 98.2$ (d). From left to right, each column refers to the MHD, HMHD, HVM and HPIC cases, respectively. For the HPIC simulation, $j_z(x, y)$ has been smoothed in order to remove particle noise.

eigenmode obtained in large amplitude compressible MHD theory, namely $B = |\mathbf{B}| = const$ is not satisfied by our initial perturbations [92]. This suggests that pressure and density fluctuations may be generated during the wave packets evolution. Therefore, the initial data are nonlinear eigenmodes of incompressible MHD, but not exact eigenmodes of compressible MHD. On the other hand we do not expect significant differences because the initial $B = |\mathbf{B}|$ fluctuations are not very large (less than 10%).

1.2 Numerical results: a direct comparison between different models

In this Section we focus on the description of the results of the four different simulations (MHD, HMHD, HVM and HPIC) by focusing on some "fluid"-like diagnostics which help to understand the system dynamics and, also, to highlight the differences between the adopted models.

Figure 1.2 reports a direct comparison between the simulations, showing the contour plots of the out-of-plane component of the current density $j_z = (\nabla \times \mathbf{B}) \cdot \hat{\mathbf{z}}$. Vertical columns from left to right in Fig. 1.2 refer to MHD, HMHD, HVM and HPIC simulations, respectively; while each horizontal row refers to a different time instant: $t = 29.5$ (a), $t = \tau = 58.9$ (b), $t = 70.7$ (c)

and $t = 98.2$ (d).

In each simulation the initially separated wave packets counter-propagate, approach each other [panels (a) of Fig. 1.2], and collide at $t = \tau$. During the collision [panels (b) of Fig. 1.2], j_z intensifies, and, since the overlapping wave packets interact nonlinearly, the dynamics produces small scales that can be easily appreciated by examining the width of the current structures. After the collisions [panels (c) and (d) of Fig. 1.2], the wave packets continue their motion while displaying a significantly perturbed shape. Indeed the j_z contours indicate that current structures are much more complex after that the collision occurs. Moreover, their shape exhibits also a curvature which is not anticipated prior to the collision and which indicates the presence of energy in modes with gradients along the y direction, transverse to the propagation.

Significant differences are recovered in the MHD case with respect to the HMHD, HVM and HPIC runs. While the MHD evolution is symmetric with respect to the center of the x direction, in the other cases this symmetry is broken also before the wave packets interaction due to the presence of dispersive effects which differentiate the propagation along and against B_{0x}. Moreover, during the wave packets overlap [Fig. 1.2(b)], smaller scales structures are formed in the HMHD and the HVM cases with respect to the pure MHD evolution, while the HPIC run - despite it recovers several significant features of the wave packets interaction - suffers the presence of particles thermal noise, which has been artificially smoothed out in Fig. 1.2. After the collision [Fig. 1.2 (c) and (d)], the difference between the MHD and the other simulations becomes stronger. In particular, some vortical structures at the center of the spatial domain are recovered in the HMHD and HVM cases, in contrast to the pure MHD case. Moreover, the Vlasov simulation tends to produce smaller scales during the interaction since very thin current sheet structures are formed. Furthermore, some secondary ripples are recovered, in the HVM simulation, in front of each wave packet. These secondary, low-amplitude ripples are not recovered in the other simulations: in fact, they cannot be appreciated in the HPIC run where the noise prevents the formation of such structures while, in the Hall simulation, they are only

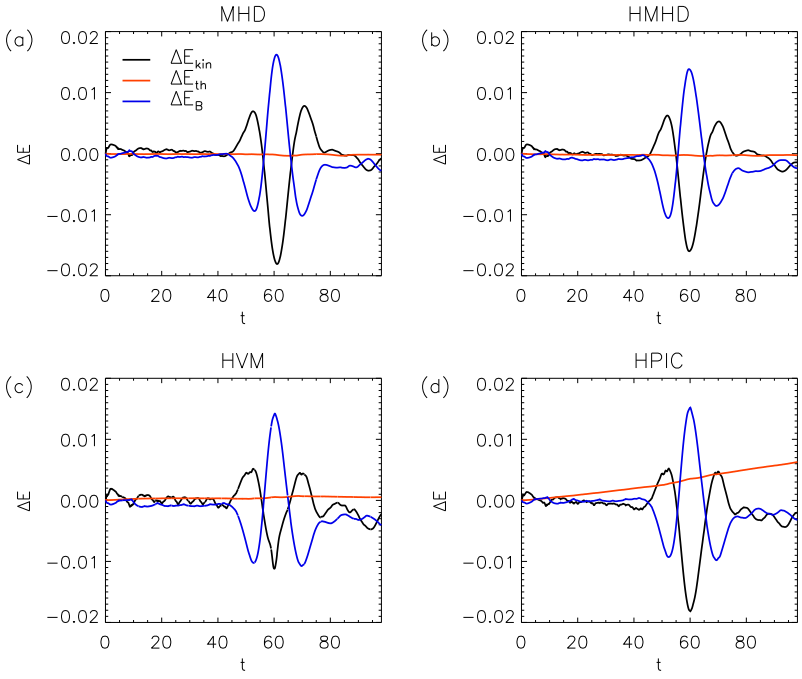

Figure 1.3: (Color online) Temporal evolution of the energy terms: ΔE_{kin} (black), ΔE_{th} (red) and ΔE_B (blue) for the MHD, HMHD, HVM and HPIC runs.

roughly visible. The nature of these low-amplitude ripples is compatible with a KAW-like activity and will be discussed in detail in the next chapter.

In order to compare models and codes, we display, in Fig. 1.3, the temporal evolution of the energy variations ΔE. Black, red and blue lines indicate respectively the kinetic ΔE_{kin}, thermal ΔE_{th} and magnetic ΔE_B energy variations, while each panel from (a) to (d) refers to the MHD, HMHD, HVM and HPIC runs, respectively. The evolution of ΔE_{kin} and ΔE_B is quite comparable in all the performed simulations and, in the temporal range where wave packets collide, magnetic and kinetic energy is exchanged. On the other hand, the evolution of the thermal energy ΔE_{th} differs in the HPIC case compared to the other simulations. Indeed, ΔE_{th} remains quite close to zero for all the simulations except for the HPIC run, where it grows almost linearly for the presence of numerical noise. It is worth to note that, as the number of particles increases, the evolution of ΔE_{th} would probably get closer to the one obtained in the MHD, HMHD and HVM simulations.

A point of comparison of our simulations with respect to the theoretical ideas given by Moffatt and Parker is to examine the behavior of cross helicity. Those theoretical treatments assume ideal non-dissipative conditions, so that the total cross helicity is conserved and moreover the expectation is that the separate wave packets after the collision have the same cross helicity as prior to the interaction. Furthermore the initial and final states, in the ideal treatment, have equipartition of flow and magnetic field energy, with departures from equipartition possible during the interaction. To examine these, Fig. 1.4 shows the temporal evolution of (a) the normalized residual energy $\sigma_r(t)$, and (b) the normalized cross-helicity $\sigma_c(t)$ [12], respectively defined as $\sigma_r = (e^u - e^b)/(e^u + e^b)$ and $\sigma_c = (e^+ - e^-)/(e^+ + e^-)$, where $e^\pm = \langle(\mathbf{z}^\pm)^2\rangle/2$, $e^u = \langle\mathbf{u}^2\rangle/2$, $e^b = \langle\mathbf{b}^2\rangle/2$ and $\mathbf{z}^\pm = \mathbf{u} \pm \mathbf{b}$. In each panel of Fig. 1.4, black, dashed blue, dashed green and red lines refer to MHD, HMHD, HVM and HPIC cases, respectively.

Figure 1.4 (a) shows the evolution of the normalized residual energy σ_r, which is similar in all the simulations. In particular $\sigma_r \simeq 0$ in the initial stage of the simulations. Then, σ_r strongly oscillates during the wave packets collisions, first to positive values indicating a positive correlation of the Elsässer fields, then moving more strongly towards negative values of correlation, and returning to positive correlation again prior to finally approaching zero once again. The σ_r oscillations are well correlated with the oscillations of ΔE_B and ΔE_{kin} seen in Fig. 1.3.

Deeper insights are revealed by the evolution of the cross-helicity σ_c, showed in Fig. 1.4 (b). Indeed, for ideal incompressible MHD, the cross helicity remains constant, and for this initial condition, $\sigma_c = 0$. Here, σ_c is well-preserved in the MHD run, despite this simulation is compressible. This means that the compressible effects, introduced here by the fact that initial perturbations are not pressured balanced, are not strong enough to break the σ_c invariance. On the other hand, for the remaining simulations (HMHD, HVM and HPIC), σ_c is not preserved: i) it shows a jump around $t = \tau = 58.9$, due to the presence of kinetic and dispersive effects, and ii) there is an initial growth of σ_c followed by a relaxation phase. It seems also significant to point out that, the initial growth of σ_c occurs faster in the

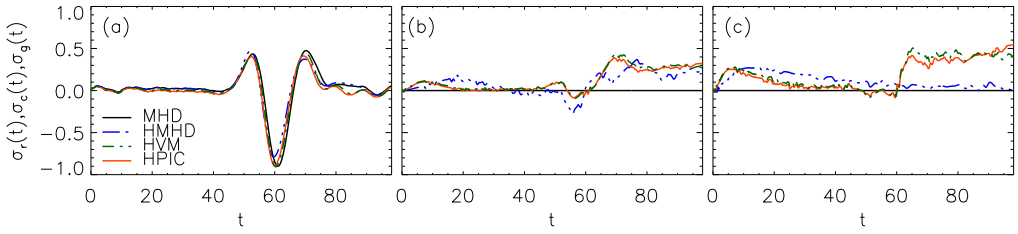

Figure 1.4: (Color online) Temporal evolution of the normalized residual energy $\sigma_r(t)$ (a), cross helicity $\sigma_c(t)$ (b) and generalized cross helicity $\sigma_g(t)$ (c). In each panel black, blue, green and red lines indicate the MHD, HMHD, HVM and HPIC simulations, respectively.

kinetic cases compared to the HMHD one. This may reflect the fact that the initial condition evolves differently in the Hall MHD simulation compared to the kinetic runs.

In order to understand the role of the Hall physics, we also computed the normalized generalized cross helicity $\sigma_g = 2e^g/(e^u + e^b)$, where $e^g = 0.5\ \langle \mathbf{u} \cdot \mathbf{b} + \tilde{\epsilon}\omega \cdot \mathbf{u}/2 \rangle$, and $\omega = \nabla \times \mathbf{u}$, which is an invariant of incompressible HMHD [15, 17]. Figure 1.4(c) displays the temporal evolution of $\sigma_g(t)$ for the MHD (black), the HMHD (dashed blue), HVM (dashed green) and HPIC (red) simulations. Note that the evolution of σ_g is trivial for the MHD simulation where, since $\tilde{\epsilon} = 0$, $\sigma_g = \sigma_c$. Moreover, it can be easily appreciated that, for the HMHD case, σ_g is almost preserved and does not exhibit any significant variation due to the collision itself, even though it shows a slight increase in the initial stages of the simulation followed by a decay towards $\sigma_g = 0$ [similar to the growth of σ_c recovered in Fig. 1.4(b)]. On the other hand the two kinetic cases, which exhibit a similar behavior, show a fast growth of σ_g in the initial stage of the simulations followed by a decay phase [similar to the growth of σ_c recovered in Fig. 1.4(b)]; then, during the collision, σ_g significantly increases. We may explain the evolution of σ_c and σ_g as follows. In the MHD run, compressive effects contained in the initial condition as well as compressible activity generated during the evolution are not strong enough to break the invariance of σ_c (i.e. of σ_g). Instead, in the Hall MHD simulation, the first break of the σ_c invariance observed in the initial stage of the simulation cannot be associated with the Hall effect since also σ_g is not

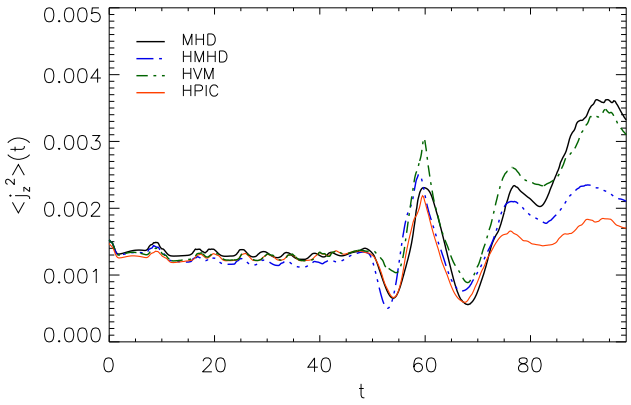

Figure 1.5: (Color online) Temporal evolution of $\langle j_z^2 \rangle$ for the MHD (black), HMHD (blue), HVM (green) and HPIC (red) simulations. For the HPIC simulation, $\langle j_z^2 \rangle$ has been smoothed in order to remove particle noise.

preserved in this temporal region and σ_c and σ_g have a similar evolution. On the other hand, the jump recovered in σ_c around $t \simeq \tau = 58.9$ is significantly related to the Hall physics. In fact, since σ_g does not exhibit a similar jump at $t \simeq \tau$, we argue that the physics which produces the growth of σ_c is the Hall physics (which is taken into account in the invariance of σ_g). Finally, the production of both σ_c and σ_g recovered in the kinetic simulations cannot be completely associated with the Hall effect (which, of course, is still present) but kinetic and compressive effects may have an important role.

In order to explore the role of small scales into the dynamics of colliding wave packets, we computed the averaged mean squared current density $\langle j_z^2 \rangle$ as a function of time. This quantity indicates the presence of small scale activity (such as production of small scale current sheets), and is reported in Figure 1.5 for all the simulations. As in the previous figures, black, blue dashed, green dashed and red lines refer to the MHD, HMHD, HVM and HPIC cases, respectively. All models show a peak of $\langle j_z^2 \rangle(t)$ around the collision time $t \simeq \tau$ due to the collision of wave packets. After the collision, some high-intensity current activity persists in all the simulations. The qualitative evolution $\langle j_z^2 \rangle(t)$ is similar in each simulation, however - after the collision - bigger values of $\langle j_z^2 \rangle$ are reached in the MHD and HVM cases with respect to the

HMHD and HPIC runs.

Other quantities that provide physical details about our simulations are $\epsilon_\rho = \langle \delta\rho^2 \rangle$ (compressibility) and the enstrophy $\epsilon_\omega = \langle \omega^2 \rangle / 2$ (fluid vorticity ω). Note that $\delta\rho = \rho - \langle \rho \rangle$. Figure 1.6 reports the temporal evolution of ϵ_ρ (a) and ϵ_ω (b) for all the runs. Black, blue dashed, green dashed and red lines indicate respectively the MHD, HMHD, HVM and HPIC cases. The ϵ_ρ evolution shows that density fluctuations peak around $t \simeq 63.8$ and $t \simeq 83.4$. The first peak is due to the interaction between the two wave packets. The second peak of density fluctuations appears to be due to propagation of magnetosonic fluctuations generated by the initial strong collision. Once generated these modes propagate across the periodic box and provide an "echo" of the original collision. Moreover, from the initial stage of the simulations, ϵ_ρ exhibits some small modulations, which are produced by the absence of a pressure balance in the initial condition. In fact, as packets start to evolve, low-amplitude fast perturbations (clearly visible in the density contour plots, not shown here) propagate across the box and collide faster compared to the "main" wave packets themselves. Moreover, by comparing the different simulations, one notices that, for $t < 20$, kinetic and Hall runs tend to produce a similar evolution of ϵ_ρ, slightly bigger compared to the MHD case. Then, around $t \simeq 20$, the HMHD run displays a stronger compressibility with respect to the kinetic cases. This difference is probably due to the presence of kinetic damping phenomena which occur in the kinetic cases.

The enstrophy ϵ_ω is displayed in Fig. 1.6(b). All the runs exhibit a similar evolution of ϵ_ω up to the wave packet collisions. Then, after the collision, a significant level of ϵ_ω is recovered in all the simulations, thus indicating that fine scale structure in the velocity, i.e., vortical structures are produced during the collisions, and these persist after the collision. Moreover, MHD and HMHD cases exhibit a quite similar level of ϵ_ω, slightly bigger compared to the one recovered in the HVM and HPIC cases, where probably kinetic damping does not allow the formation of strong vortical structures at small scales by transferring energy to the VDF [see. e.g., [110, 111]]. It is interesting to note that the general profile of enstrophy and mean square current follow similar trends in time. This can be expected as the inertial range

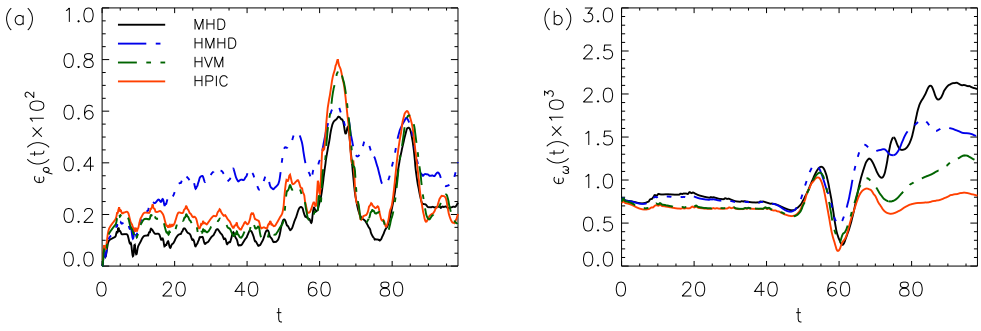

Figure 1.6: (Color online) Temporal evolution of $\epsilon_\rho(t)$ (a) and $\epsilon_\omega(t)$ (b). In each panel, black, blue, green and red lines indicate the MHD, HMHD, HVM and HPIC simulations, respectively. For the HPIC simulation, $\epsilon_\omega(t)$ has been smoothed in order to remove particle noise.

of turbulence typically provides near-equipartition of velocity and magnetic fluctuation energy, even in fairly simple configurations [112]. However, when examined in more detail, one often finds, as here, that the magnetic fluctuations are usually about a factor of two more energetic in the inertial range part of the spectrum, as they are, for example in the solar wind [113]. This inequality is here reflected in the fact that $\langle j_z^2 \rangle > \langle \omega^2/2 \rangle$.

It is interesting to compare different simulations also by looking at power spectral densities (PSDs). Figures 1.7 show the magnetic energy PSD integrated along k_y $E_{b,y}(k_x) = \sum_{k_y} E_b(k_x, k_y)$ (left column) and along k_x $E_{b,x}(k_y) = \sum_{k_x} E_b(k_x, k_y)$ (right column); while each row respectively refers to $t = 29.5$ (top row), $t = \tau = 58.9$ (center row) and $t = 98.2$ (bottom row). The cyan dashed line shows the $k^{-5/3}$ slope for reference while, in each panel, black, blue, dashed green and red lines indicate respectively MHD, HMHD, HVM and HPIC simulations. Moreover, to compare the two wave-number directions, gray lines in each panel report the corresponding PSD obtained from the MHD run, reduced in the other direction [for example, in the top row left panel, the gray line refers to $E_{b,x}(k_y)$ for the MHD simulation while other curves in the same panel report $E_{b,y}(k_x)$]. It is interesting to note that, at $t = 29.5$, all the simulations exhibit a steep spectrum in $E_{b,y}(k_x)$, related to the initial condition which requires involvement of a wide range of

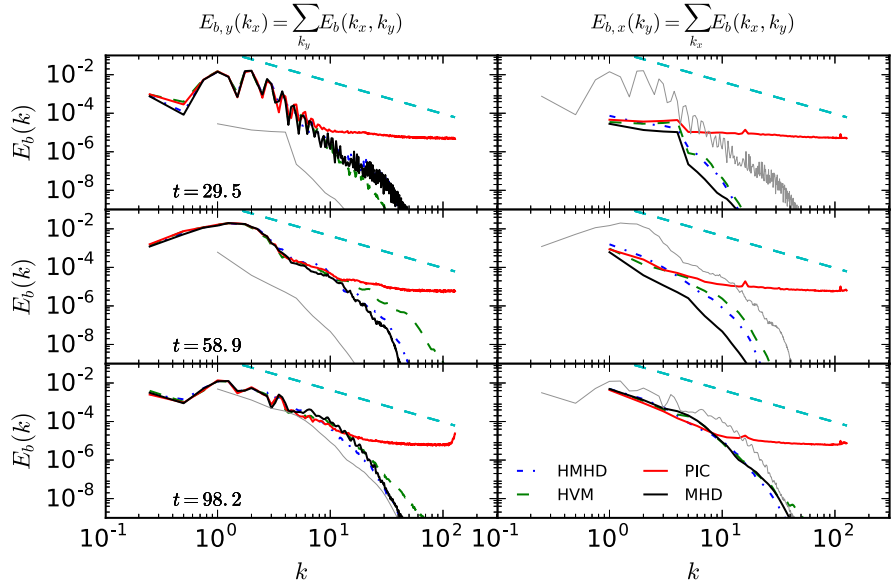

Figure 1.7: (Color online) Magnetic energy PSDs $E_{b,y}(k_x) = \sum_{k_y} E_b(k_x, k_y)$ (left column) and $E_{b,x}(k_y) = \sum_{k_x} E_b(k_x, k_y)$ (right column) at three time instants: $t = 29.5$ (top), $t = \tau = 58.9$ (middle) and $t = 98.2$ (bottom). In each panel black, blue, green and red lines refer to the MHD, HMHD, HVM and HPIC simulations, respectively; while cyan lines show the $-5/3$ slope for reference. Moreover, to compare $E_{b,y}(k_x)$ and $E_{b,x}(k_y)$, the gray lines in each panel refer only to the MHD simulation and report $E_{b,x}(k_y)$ in the left column and $E_{b,y}(k_x)$ in the right column.

wave-numbers k_x. Then, during the evolution, the spectra show a transfer of energy towards small scales, at higher k_x and at higher k_y. In fact, much of the energy $E_{b,y}(k_x)$ is contained, at $t = \tau$, in a bump around $k = 1$. At $t = 88.4$ the bump is less clear and the spectrum $E_{b,y}(k_x)$ is quite well developed and the spectral slope, at scales larger than the ion inertial scale, is close to $-5/3$. A break in $E_{b,y}(k_x)$ can be also appreciated around $k_{d_p} \simeq 10$. Moreover, the difference in power between $E_{b,y}(k_x)$ and $E_{b,x}(k_y)$ - the latter being significantly smaller than the former - tends to reduce in the final stages of the simulations, thus suggesting the presence of nonlinear couplings which efficiently transfer energy in both directions of the wavevectors space and, hence, cause spectra to become more isotropic.

1.3 Summary

To summarize, in this Chapter we compared our numerical codes by analyzing some global fluid-like diagnostics and we conclude that the Moffatt-Parker scenario is quite well satisfied by MHD. However, other intriguing features are observed when one moves beyond the MHD treatment. Indeed, several quantities (especially the cross-helicity) indicates that the evolution is different when one introduces more complex scenarios and the complexity of the structures produced by nonlinear interactions in the HMHD and HVM simulations makes it difficult to determine whether the wave packets actually attain a full separation after their collision.

Moreover, during the wave packets interaction, as prescribed by *Parker & Moffatt*, nonlinear coupling processes cause the magnetic energy spectra to evolve towards isotropy and energy is transferred towards smaller spatial scales. After the wave packets interaction magnetic energy spectra exhibits a "power law"-like profile, whose slope is close to $-5/3$ at bigger scales, while a spectral break is recovered around k_{d_p}. In the next Chapter we will focus on the nature of the interaction which produces such spectrum, trying to describe it in terms of wave-like activity and strong turbulence.

The comparison between kinetic codes suggests that HVM and HPIC simulations display qualitatively similar features at large scales. However, when one aims to analyze the dynamics at small scales, HPIC simulations suffers from thermal particle noise. Indeed, magnetic energy spectra differ in the HPIC case as compared to the HVM case, since, in the former case, spectra saturate at small scales due to the numerical noise, visible - in particular - in the contour plots of j_z. Based on these considerations, in the next Chapter we will continue the analysis of the kinetic features produced in the Alfvén wave packets collision, by focusing only on the HVM simulation.

Chapter 2

Kinetic turbulence generated by Alfvén wave collisions

In this chapter we focus on two particular aspects of the HVM simulation described previously. The former regards the production of kinetic effects during the evolution and the collision of the two wave packets [Section 2.1], while the latter concerns the characterization of the wave packets interaction in terms of wave-like activity and strong turbulence [Section 2.2].

Indeed, several indicators of kinetic effects (temperature anisotropies, nongyrotropies or non-Maxwellian indexes) have been implemented. These quantities indicate that the velocity distribution function exhibits out of equilibrium features before the wave packets interaction due to the fact that the initial condition is not an even solution of the HVM equation. Kinetic effects become more intense during the interaction and a beam along the magnetic field direction is also recovered in the velocity distribution function similarly to some recent solar wind observations [76].

We describe also the wave packets interaction as concerns the presence of weak or strong turbulence. It has been found that the presence of secondary small amplitude ripples, which are recovered after the collision at the front of each wave packet, can be successfully explained in terms of a wave-like activity and are identified as Kinetic Alfvén Waves. However the general picture is more complex and other signatures of a strong turbulence scenario

coexist with the presence of these fluctuations. Indeed, after the collision, the magnetic energy does not rigidly follow a standard wave dispersion relations, but tends to spread over a wide band of the $\omega - k$ plane. Furthermore, a large part of the energy is stored in the $\omega = 0$ "channel", thus indicating that stationary structures, typical of a strong turbulent scenario, are produced during the interaction.

Finally, in Section 2.3 we conclude by summarizing our work. The results shown here have been collected in two scientific papers: the first has been recently published in *Journal of Plasma Physics* [99] while the second is in preparation [114].

2.1 Kinetic features recovered during the wave packets interaction

We begin the description of kinetic signatures present in the Vlasov simulation by looking at the temperature anisotropy in the particle distribution function. Fig. 2.1 reports the contour plots of the temperature anisotropy $T_\perp/T_\parallel$, where the parallel and perpendicular directions are evaluated in the local magnetic field frame (LBF), at four time instants: $t = 29.5$ (a), $t = \tau = 58.9$ (b), $t = 70.7$ (c) and $t = 98.2$ (d). Clearly, temperature anisotropy is present even before the main wave packets collision [Fig. 2.1(a)], due to the fact that the initial configuration is not solution of the HVM equations and, hence, its dynamical evolution leads to anisotropy production. Moreover, a more careful analysis suggests that the left wave packet tends to produce regions where $T_\perp/T_\parallel < 1$ close to the packet itself (localized around $x \simeq 9.5$), while the right wave packet (localized around $x = 15.7$) is characterized by $T_\perp/T_\parallel > 1$. The presence of different temperature anisotropies ($T_\perp/T_\parallel < 1$ or $T_\perp/T_\parallel > 1$) is related to the asymmetry with respect to the center of the x direction. Indeed, the dynamics of the wave packets is different if they move parallel or anti-parallel to $B_{0,x}$. This produces the different temperature anisotropy recovered in the top panel of Fig. 2.1.

When the packets collide [Fig. 2.1 (b)], sheets characterized by a strong

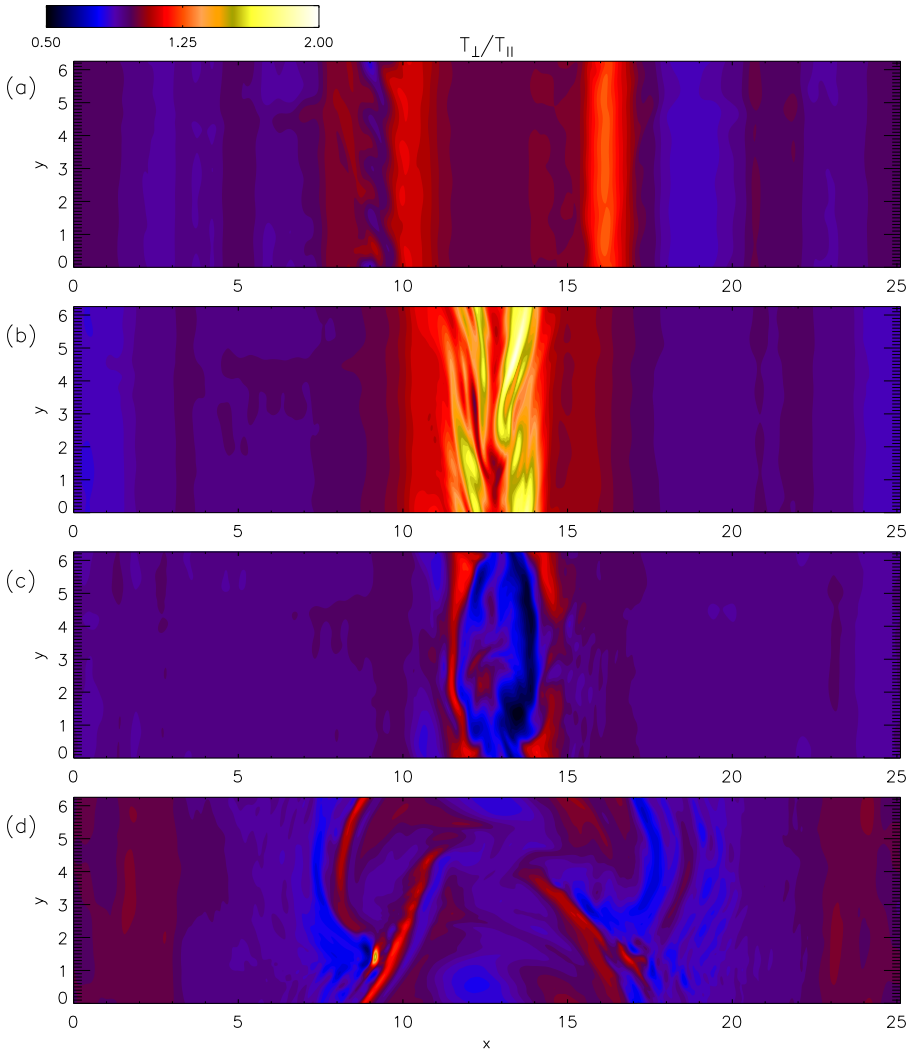

Figure 2.1: (Color online) Contour plots of the temperature anisotropy, for the HVM run, evaluated in the LBF at four time instants: (a) $t = 29.5$, (b) $t = \tau = 58.9$, (c) $t = 70.7$ and (d) $t = 98.2$.

temperature anisotropy ($T_\perp/T_\parallel > 1$) are recovered, spatially correlated with the current density structures. Then, at $t = 70.7$ [Fig. 2.1 (c)], wave packets split again and a region, localized at $(x, y) \simeq (14.3, 1.0)$, where the temperature anisotropy suddenly moves from values $T_\perp/T_\parallel < 1$ towards $T_\perp/T_\parallel > 1$ ones is present. We will show that this region also exhibits the presence of strong departures from the equilibrium Maxwellian shape. At the final stage

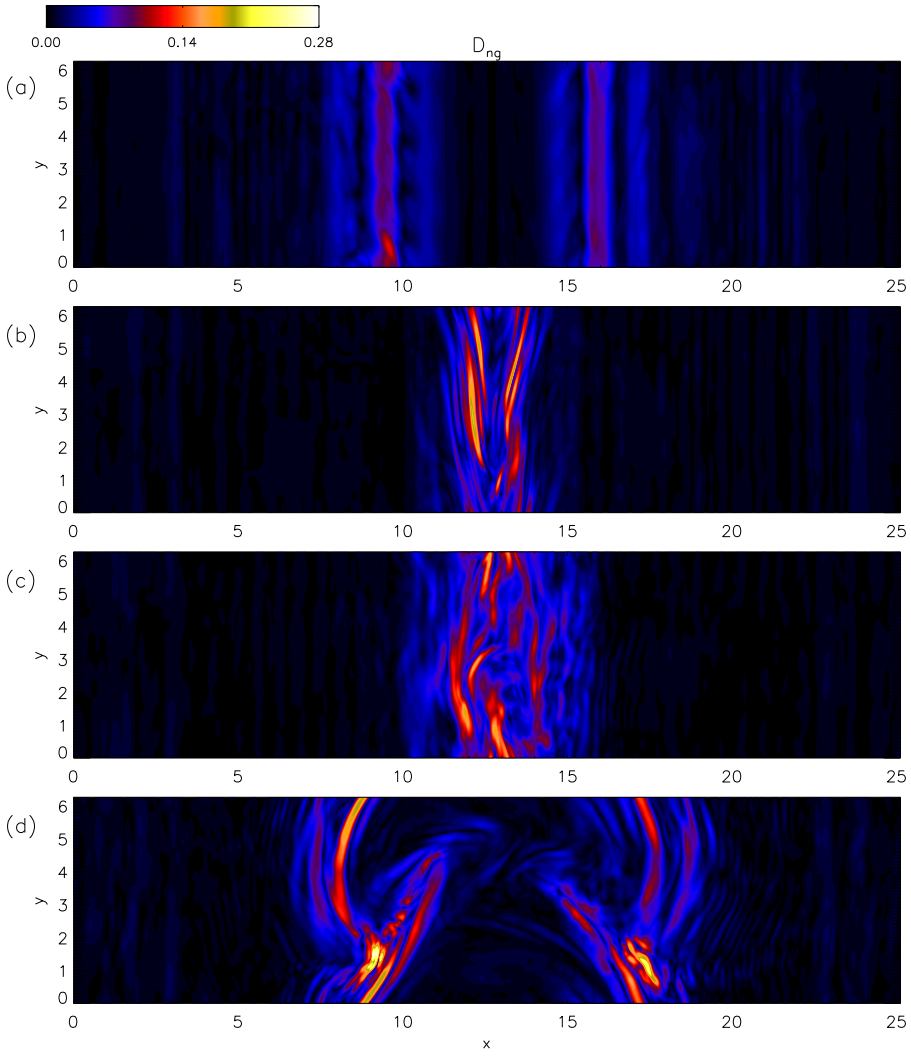

Figure 2.2: (Color online) Contour plots of the degree of temperature non-gyrotropy D_{ng}, for the HVM run, evaluated in the LBF at four time instants: (a) $t = 29.5$, (b) $t = \tau = 58.9$, (c) $t = 70.7$ and (d) $t = 98.2$.

of the simulation [Fig. 2.1 (d)], each wave packet continues traveling, accompanied by a persistent level of temperature anisotropy, which is, indeed, well correlated with the current structures [See Fig. 1.2(d)].

It is interesting to point out that, beyond the presence of temperature anisotropies, regions characterized by a nongyrotropy of the particle VDF are also recovered. Many methods have been proposed to evaluate the nongy-

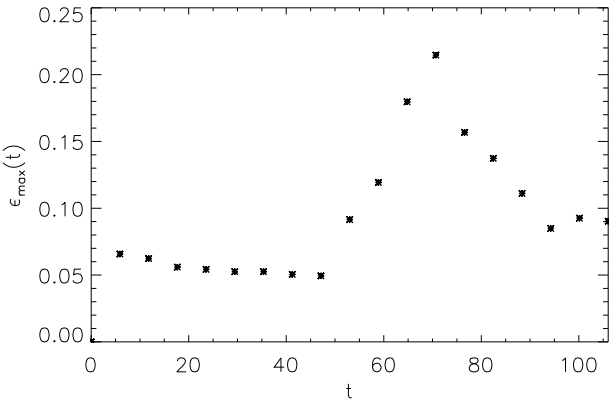

Figure 2.3: (Color online) Temporal evolution of $\epsilon_{max}(t)$ for the HVM run.

rotropy [115, 116]. Here we make use of the "nongyrotropy degree" D_{ng} [115], which is proportional to the root-mean-square of the off-diagonal elements of the pressure tensor. Fig. 2.2 reports the contour plots of nongyrotropy degree D_{ng} at four time instants: $t = 29.5$ (a), $t = \tau = 58.9$ (b), $t = 70.7$ (c) and $t = 98.2$ (d). As for the temperature anisotropy, the evolution of the two wave packets tends to produce nongyrotropyc features even before the wave packets collision [Fig. 2.2(a)]. Then, during the collision [Fig. 2.2(b)–(c)], the nongyrotropy D_{ng} becomes more intense and it is also quite well correlated with the current structures [See 1.2(b)–(c)]. At the final stage of the simulation [Fig. 2.2(d)], each wave packet is connoted by a level of nongyrotropy which is quite bigger compared to the value before the collision. The presence of nongyrotropic regions suggests that it is fundamental to retain a full velocity space where the VDF is let free to evolve and, eventually, distort. It is worth to note that the approach based on gyro-averaged assumptions lacks the presence of such nongyrotropies.

To further support the idea that kinetic effects are generated during the interaction of the wave packets, we computed the L^2 norm difference [30, 31, 35]:

$$\epsilon(x, y, t) = \frac{1}{n}\sqrt{\int \left[f(\mathbf{x}, \mathbf{v}, t) - f_M(\mathbf{x}, \mathbf{v}, t)\right]^2 d\mathbf{v}} \tag{2.1}$$

which measures the displacements of the proton VDF $f(\mathbf{x}, \mathbf{v}, t)$ with respect

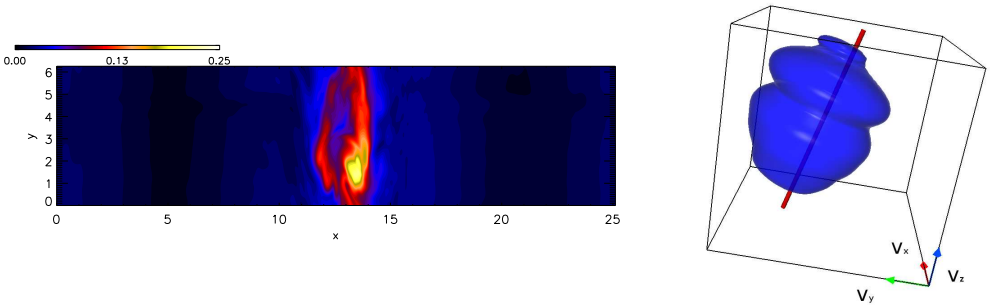

Figure 2.4: (Color online) (Left) Contour plots of $\epsilon(t)$, for the HVM run, at $t = 70.7$. (Right) Proton distribution functions, in the spatial point (x^*, y^*) where $\epsilon(x^*, y^*, t) = \max_{(x,y)} \epsilon(x, y, t)$ at $t = 70.7$. The local magnetic field direction is indicated by a red line.

to the associated Maxwellian distribution function $f_M(\mathbf{x}, \mathbf{v}, t)$, built in such a way that density, bulk speed and total temperature of the two VDFs are the same. Figure 2.3 reports the evolution of $\epsilon_{max}(t) = max_{D_{(x,y)}} \epsilon(x, y, t)$ as a function of time. As for previous non-Maxwellian indicators, also ϵ_{max} moves away from zero in the early phases of the simulation due to the fact that the initial condition is not a Vlasov solution. After the initial jump, ϵ_{max} remains almost constant up to the wave packets interaction. During the collision, ϵ_{max} grows and reaches its maximum at $t = 70.7$. Then it decreases and saturates at a value about two times bigger than the value before the collision, thus suggesting, again, that there is "net" production of non-Maxwellian features during the wave packets interaction.

The left panel of Figure 2.4 shows the contour plot of $\epsilon(x, y, t)$ at the time instant $t = 70.7$ (when ϵ reaches its maximum value). The ϵ contours are correlated with the current structures and with the anisotropic/nongyrotropic regions. Moreover, a blob-like region where ϵ reaches its maximum is present. This area is associated with the region where the temperature anisotropy moves from $T_\perp/T_\parallel < 1$ to $T_\perp/T_\parallel > 1$ [See Fig. 2.1(c)]. In this area the VDF strongly departs from the Maxwellian. The right panel of Fig. 2.4 shows the three dimensional isosurface plot of the VDF at $t = 70.7$ and in the spatial point (x^*, y^*) where ϵ is maximum. A well-defined beam, parallel to the local magnetic field direction, is observed in the VDF of Fig. 2.4. The drift speed

of the beam is about $\tilde{c}_A$. The production of a beam due to the interaction of two wave packets has been also pointed out by He et al. in a recent paper where solar wind *in-situ* observations are presented [76].

2.2 Turbulence features generated by Alfvén wave packet collisions

In this section we characterize the packets interaction in terms of wave-like activity and strong turbulence. We remind the reader that i) the ratio between the nonlinear time τ_{nl} and the collision characteristic time τ_{coll} is about $1/2$, this indicating that a strong turbulence scenario may occur and ii) power spectra resulting after the collision have slopes $\sim -5/3$, typical of a strong turbulence situation [See Fig. 1.7], and a spectral break is recovered around $k_{d_p} \simeq 10$.

Here, we focus on the description of two features recovered after the collision: i) secondary ripples appear in front of each wave packet as small amplitude fluctuations propagating almost purely along x and ii) current sheets tend to distort producing some vortical structures at the center of the spatial domain. Both features can be appreciated in Figs. 1.2(c–d) (third column) and in Fig. 2.5, that reports the shade surface of $j_z(x, y, t)$. In Fig. 2.5 The horizontal plane corresponds to the spatial coordinates x and y, while the temporal evolution is given by the vertical blue axis.

In order to understand the physical mechanism driving the production of these secondary low amplitude fluctuations, we started from the evidence that these ripples propagate mainly along x. Moreover, Fig. 2.6 (a) reports the evolution of $|\mathbf{B}|(x, y_0, t^*)$ (black) and $n(x, y_0, t^*)$ (red) as a function of x in the region where these disturbances are present $x = [17.5, 21.6]$ and for $y = y_0 = 1.2$ and $t = t^* = 98.2$: clearly, density n fluctuations are anti-correlated with the $|\mathbf{B}|$ fluctuations, this being typical of Kinetic Alfvén and slow magnetosonic waves [79, 106, 107].

A second aspect which helps to discriminate about different type of waves is the polarization [106], which can be evaluated through the hodogram of

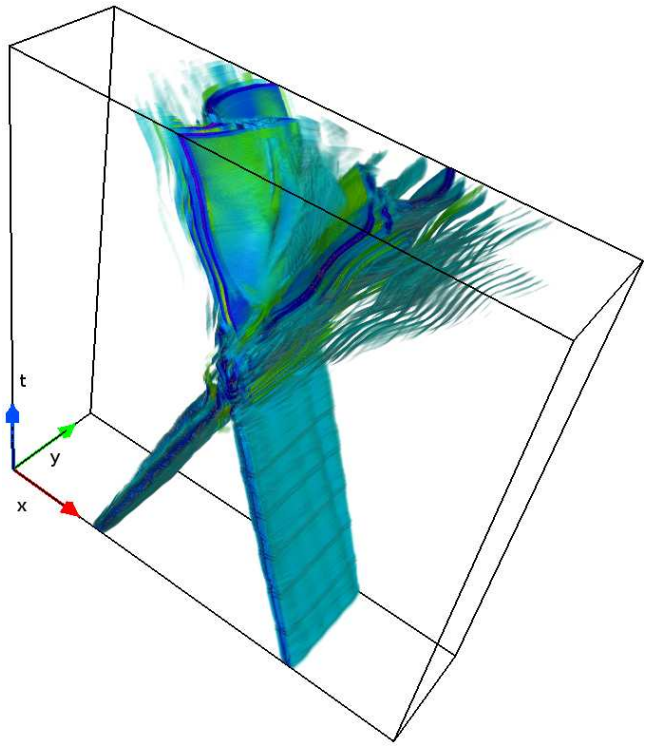

Figure 2.5: (Color online) Iso-surfaces of the current density $j_z(x, y, t)$. Red, green and blue axes correspond to the x, y and temporal directions, respectively.

two magnetic field components, as explained in detail in Ref. [106]. Figure 2.6 (b) reports the hodogram of $\delta B_z(x, y_0, t^*)$ as a function of $\delta B_y(x, y_0, t^*)$, in the region $x = [17.5, 21.6]$ and for $y = y_0 = 1.2$ and $t = t^* = 98.2$. The red square in Fig. 2.6 (b) reports the initial x point $x = 17.5$. The hodogram shows a clock-wise verse of rotation with increasing x. This verse of rotation is compatible only with KAW or fast magnetosonic fluctuations, as computed by means of a linear solver where the evaluated $k_{\|} \simeq 1.73 = 0.17 k_{d_p}$ and $k_{\perp} \simeq 16.2 = 1.59 k_{d_p}$ have been utilized. Finally, by computing the propagation speed of these fluctuations, we found that this velocity is compatible with the KAWs propagation speed. Therefore, based on these three methods (correlations, polarization and propagation speed) we conclude that the small amplitude fluctuations are compatible with KAW-like fluctuations. The presence of these fluctuations can be explained as follows: the interaction of the two wave packets transfers energy towards smaller scales and,

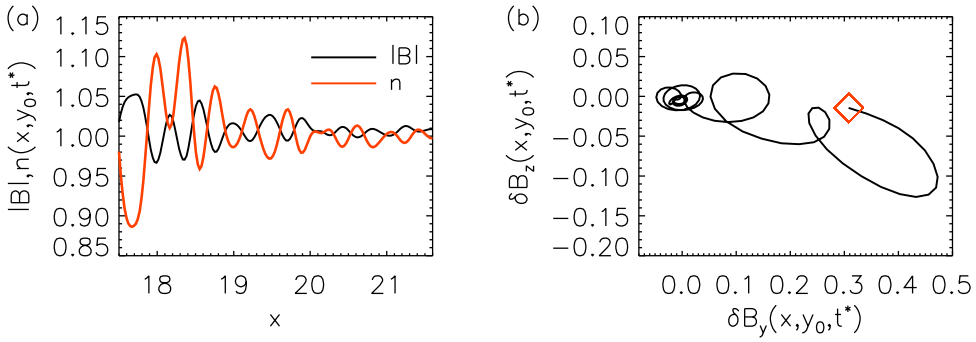

Figure 2.6: (Color online) (a) Shape of $|\mathbf{B}|$ (black) and n (red) as a function of x in the region $x = [17.5, 21.6]$ and for $y = y_0 = 1.2$ and $t = t^* = 98.2$. (b) Hodogram of $\delta B_z(x, y_0, t^*)$ as a function of $\delta B_y(x, y_0, t^*)$ for $x = [17.5, 21.6]$ and for $y = y_0 = 1.2$ and $t = t^* = 98.2$. The red square indicates the initial x point $x = 17.5$.

since the initial disturbances are mainly Alfvénic, the energy is transferred along the Alfvén waves branch, therefore producing KAW fluctuations.

The explanation of the system dynamics just in terms of wave-like activity is restrictive and the KAW small amplitude fluctuations we described above are just one piece of a much more complex scenario. In fact, since $\tau_{nl}/\tau_{coll} < 1$, a strong turbulence regime may be reached. In order to point out that the picture can be actually more complex, we performed the following analysis. First, we selected two temporal windows of duration $T \simeq 29.5$, before (I) and after (II) the wave packets collision. In both windows, the magnetic energy $E_b(\mathbf{x}, t)$ is quite stationary, this allowing us to implement a full spatio-temporal Fourier transform of $E_b(\mathbf{x}, t)$ to get $E_b(\mathbf{k}, \omega)$. Note the ω resolution is quite high: in fact the ω mesh grid is about $2\pi/T \simeq 0.21$, being this value quite smaller than the ω resolution commonly recovered through spacecraft measurements [93, 95, 96, 97]. This last quantity gives information about how the magnetic energy is distributed in the three-dimensional space $\mathbf{k} - \omega$. Figure 2.7 reports the contour plots of $E_{b,y}(k_x, \omega)$ (left) and $E_{b,x}(k_y, \omega)$ (right) in region I (top) and II (bottom).

Before the interaction, the energy $E_{b,y}(k_x, \omega)$ is recovered mostly at relatively larger scales and is distributed in two branches of waves: the Alfvénic waves branch (smaller phase speed) and the fast magnetosonic waves branch

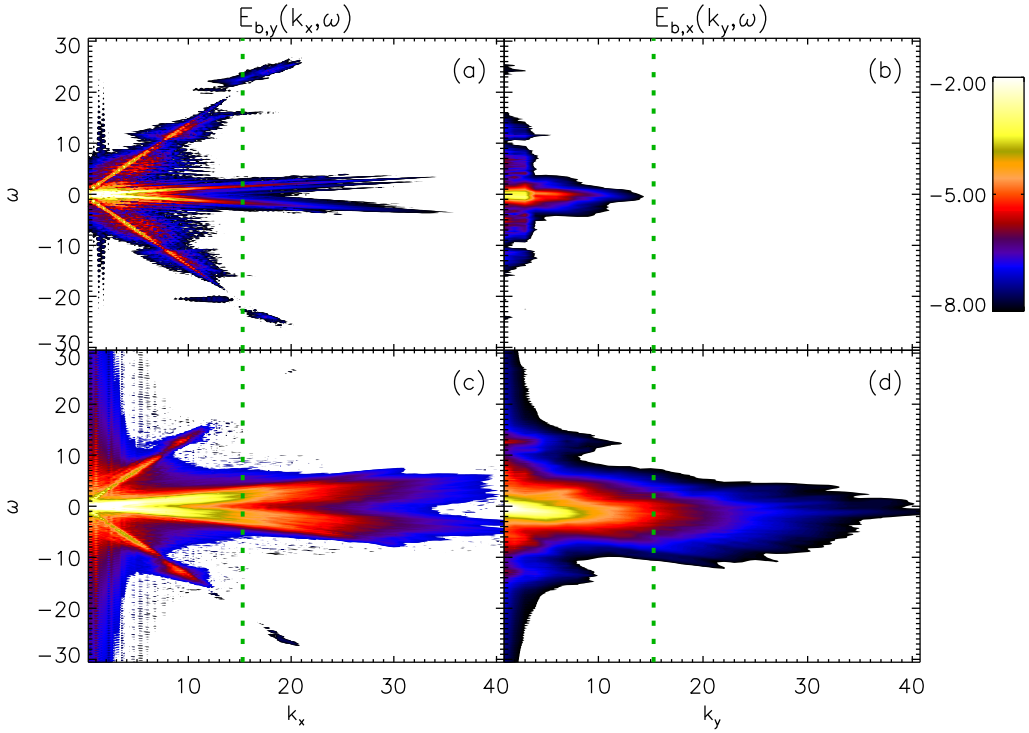

Figure 2.7: (Color online) Contour plots of the Logarithm of the magnetic energy spectra in the spectral space. Left column displays $E_{b,y}(k_x,\omega) = \langle E_b(\mathbf{k},\omega)\rangle_{k_y}$ in the plane $k_x - \omega$ in the temporal region I (a) and II (c) while the right column reports $E_{b,x}(k_y,\omega) = \langle E_b(\mathbf{k},\omega)\rangle_{k_x}$ in the plane $k_y - \omega$ in the temporal region I (b) and II (d).

(larger phase speed). It is worth noting that, since the background magnetic field is quasi-perpendicular to the propagation plane, the Alfvén speed is much smaller compared to the Fast magnetosonic phase speed, while the coexistence of different waves branches before the main interaction of the two wave packets confirms that our initial perturbations are not purely Alfvénic eigenmode but also contain some magnetosonic fluctuations. Moreover, some Bernstein fluctuations are also present along the fast waves branch at high frequencies. On the other hand, the energy $E_{b,x}(k_y,\omega)$ is quite localized around $\omega = 0$.

During the wave packets collision, the nonlinear couplings transfer energy towards small scales. The energy transfer can be easily appreciated in the

bottom panels of Fig. 2.7. Indeed, both $E_{b,y}(k_x, \omega)$ (c) and $E_{b,x}(k_y, \omega)$ (d) exhibit a distribution of energy much more populated at high wavenumbers with respect to the energy distribution in the region I. The distribution of energy is significantly spread in the spectral space and does not rigidly follow dispersion relations: a cone-like region is populated along the k_x direction, while a wide blob is covered in the k_y direction. This suggests that the wave packets interaction cannot be simply described in terms of weakly nonlinear couplings occurring along the dispersion relation, but off-dispersion couplings and strong turbulence activity are also important. Note that the presence of standard dispersion relations is weakened even after a single collision: the scenario would be much more complex if wave packets could interact several times or for a longer time period.

To better point out the fact that, during the wave packets interaction, off-dispersion channels are populated as a result of strong turbulence, Fig. 2.8 reports the profile of $E_{b,y}(k_x = k^*, \omega)$ as a function of ω and at a given $k_x = k^* = 15.3 = 1.5 k_{d_p}$, while the inset of Fig. 2.8 reports $E_{b,x}(k_y = k^*, \omega)$ as a function of ω and at a given $k_y = k^* = 15.3 = 1.5 k_{d_p}$. Fig. 2.8 essentially represents a cut of Figs. 2.7 at a given wavenumber, indicated with a green dashed line in Fig. 2.7. Red and black lines in Fig. 2.8 refer to the temporal windows before (I) and after (II) the wave packets collision, respectively. As it can be easily appreciated from Figs. 2.7(a–c), the range of ω has been opportunely chosen to focus on Alfvénic fluctuations.

Before the collision (red line), the energy is constrained in a relatively narrow band whose width is about few $\omega_0 \simeq 2\pi/T$. Then, after the wave packets interaction (black line), the energy is instead significantly spread (the populated frequency band width increases about a factor 5). This confirms that the energy flows towards smaller scales far from the weakly nonlinear coupling prediction. Furthermore, the amplitude of $E_{b,y}(k_x = k^*, \omega)$ increases for all the frequencies range showed in Fig. 2.8, thus representing, again, the production of small scales fluctuations obtained during the wave packets interaction.

Finally, the energy associated with structures at $\omega = 0$ significantly increases after the collision; this suggests that turbulent stationary structures

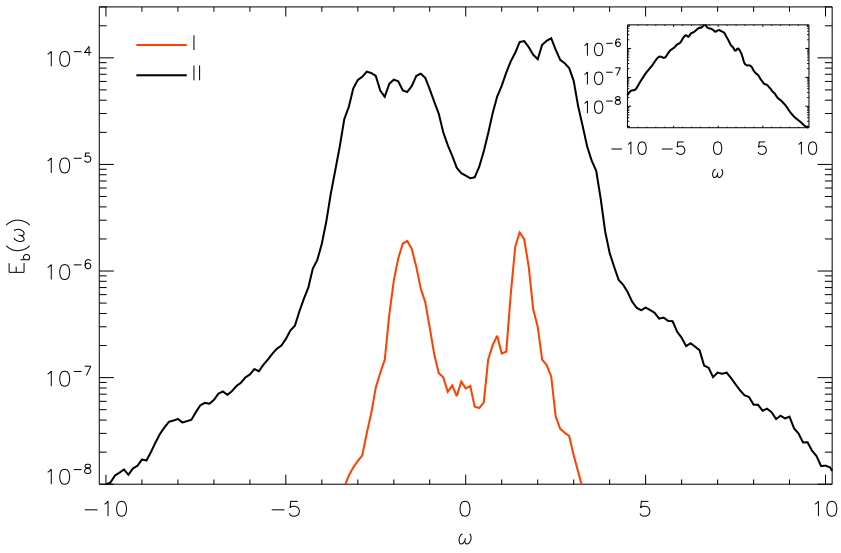

Figure 2.8: (Color online) Plot of $E_{b,y}(k_x = k^*, \omega)$, being $k^* = 15.3$, as a function of ω in the region I (black) and II (red). The small inset plots $E_{b,x}(k_y = k^*, \omega)$ as a function of ω in the region II.

have been generated during the wave packets interaction. A second signature concerning the production of stationary fluctuations can be also observed in Fig. 2.7(c) and in the inset of Fig. 2.8, where the energy is peaked at $\omega \simeq 0$, similarly to some recent solar wind observations [97].

2.3 Summary

To summarize, we focused on the HVM simulation and we described the presence of kinetic effects and the characteristics of the turbulence generated in the Alfvénic wave packet collisions. A certain degree of non-Maxwellianity is also recovered before the interaction as a byproduct of the initial condition which is not an exact HVM solution. However, several kinetic effects indicators suggest that kinetic signatures are more intense during the collision, due to the nonlinear coupling mechanisms which populate smaller scales. We also investigated the wave packets interaction in terms of waves activity and strong turbulence. We found that the wave approach can be successfully

applied to small amplitude fluctuations identified as KAWs, while a deeper comprehension must also consider the presence of strong turbulence features such as the weakening and the broadening of the dispersion relations and the production of quasi-stationary $\omega = 0$ fluctuations.

Discussion

Here we summarize the aim which led us to consider the problem of two counter-propagating Aflvénic wave packets and the main results obtained. We carried out a comparative study using different plasma simulation methods to examine the dynamical evolution that accompanies the interaction or "collision" of two oppositely propagating wave packets. In particular, we described the wave packets interaction by means of MHD, Hall MHD and hybrid kinetic simulations of the same physical configuration. Kinetic simulations have been performed with two different codes: an Eulerian Vlasov-Maxwell code [40] and hybrid Particle-in-cell code [27]. This preliminary examination of the fate of the Moffatt and Parker conjecture in the context of compressible as well as dispersive and kinetic models has produced a satisfactory, if not complete, picture. The basic physics of large amplitude Alfvén waves collisions as envisioned by Moffatt and Parker [5, 6] is recovered, however several intriguing characteristics emerge as one move beyond the ideal MHD treatment and the dynamics becomes more complex.

In each simulation, the interactions and the structures produced in the collision are sufficiently complex that it is difficult to determine whether the wave packets actually attain a full separation after the collision. Indeed, we note that very complex current and vorticity structures are produced at small scales and these fluctuations are indicative of a spread of energy in the wave vectors plane, which is almost perpendicular to $\mathbf{B_0}$. The energy spectra evolve toward isotropy in this plane, although one would expect a degree of spectral anisotropy to persist due to the presence of the weak in-plane magnetic field. Furthermore, to the extent that the interaction of the packets has a finite lifetime, any such relaxation would be expected to be

incomplete in a single interaction time.

In addition, we recall that in the incompressible ideal MHD case, the cross helicity is conserved, so that after the collision in that case, the separated wave packets will each contain the same energy that was present in the initial state. However, cross-helicity is not preserved in the Hall and kinetic cases since dispersive and kinetic effects are at work in the simulations and a significant variation is observed during the interaction.

Note that we also analyzed the same physical problem employing several theoretical models and numerical models and such results are of interest in the context of the Turbulent Dissipation Challenge [98]. The HPIC and HVM methods should describe, approximately, the same physics (the hybrid Vlasov treatment of collisionless plasma dynamics) and the comparison between the two codes is interesting from a methodological perspective. The two kinetic performed simulations are able to take into account the dynamics which occurs at large spatial scales and their comparison is quite discrete in this range of scales. However, the HPIC runs lacks accuracy at smaller spatial scales, thus indicating that the Eulerian approach better describes the dynamics of the system at these scales. The comparison is expected to become better if the number of particle per cell in the PIC simulation gets bigger [28, 34].

Based on the last consideration, we analyzed the production of kinetic signatures by focusing only on the HVM simulation. Several kinetic indicators show that wave packets tend to produce kinetic effects such as temperature anisotropies and nongyrotropies also before the main wave packets interaction. This is related to the fact that the initial condition, consisting of quasi-Alfvénic wave packets, is not a Vlasov equilibrium and it dynamically leads to the production of kinetic features. However, the analysis of kinetic effects before and after the main wave packets collision indicates that some kinetic features are enhanced by the collision itself and each wave packet is significantly characterized by a strong degree of non-thermal signatures. The presence of nongyrotropies suggests that descriptions based on reduced velocity space assumptions may partially fail the description of such features. During the wave packet collision, a beam in the velocity distribution function

is observed to form along the direction of the local magnetic field. This characteristic may connect our results with the general scenario of wave packets observed in natural plasmas such as the solar wind [76].

Finally we characterized the interaction of two colliding Alfvénic wave packets by means of HVM simulation in terms of wave-like activity and strong turbulence signatures. Since the ratio between the nonlinear time to the overlapping time allows a quite strong turbulence scenario, it is significant to figure out which features of a wave-like approach resist to the strong turbulent regime and, on the other hand, which characteristics are lost. We found that a wave-like analysis, based on polarization and correlation, is still useful to characterize the low-energy ripples recovered in the current density contour plot which are associated with KAW like fluctuations. However signatures of strong turbulence are also recovered. In particular the energy in the $\omega - k$ plane is spread after the wave packets collision and the presence of dispersion relations is significantly weakened. The energy contained in the $\omega = 0$ fluctuations also increases, thus suggesting the production of stationary structures associated with current structures.

The kinetic models we implemented to describe the problem of the two colliding Alfvénic wave packets neglects inter-particle collisions. Within these approaches, the particle velocity distribution function is free to explore the full velocity space and exhibits strongly distorted shapes [30, 33, 35]. Here we also gave explicit evidence that evident non-Maxwellian signatures are recovered in the VDF as a result of the wave packets interaction. However, the presence of out-of-equilibrium VDF profiles opens a fundamental question: since collisionality explicitly depends on gradients in velocity space, can such gradients (i.e. fine structures) locally enhance the effect of collisions? In other words, where strong gradients in velocity space are recovered, can collisions be neglected? The next part of the thesis will focus on addressing the answers, which - as we will see - are extremely difficult, to these questions; showing, in particular, that collisionality is effectively enhanced when one takes into account the presence of fine velocity structures.

Part II

Beyond the Vlasov approach: how to introduce collisions in a collisionless plasma

In the previous part of this thesis we extended the problem of two colliding Alfvénic wave packets, previously investigated within a fluid approach, to the collisionless, kinetic plasma physics framework, where the distribution function is let free to explore the full velocity space. We showed that, when the typical scales of kinetic processes are reached, the distribution function becomes strongly distorted as a consequence of such mechanisms. We propose here to make a step forward into the comprehension of the plasma dynamics by taking into account inter-particle collisions.

The description of collisional effects in plasmas represents historically a huge scientific topic in which significant numerical and theoretical efforts have been made even in recent years. In a weakly collisional plasma, such as the solar wind, collisions are usually considered far too weak to produce any significant effect on the plasma dynamics [12]. However, several observations indicate that the solar wind is incessantly heated during its travel through the heliosphere. Indeed, the temperature decay along the radial distance is much slower than the predictions of adiabatic models of the solar wind expansion [117, 118, 119, 120]. Hence, some local heating mechanisms play a significant role to supply the energy needed to heat the plasma.

Numerous scenarios have been proposed to understand the plasma heating (See [12] and references therein). Among these processes, turbulence efficiently contributes to the local heating of solar wind [119, 121, 122], since the energy transfer towards small scales - where dissipative processes are at work [123] - is more efficient as the flow becomes more turbulent. On the other hand, a long-standing debate about which dissipative processes are preferred by the plasma is still waiting for a clear and definitive answer. Many of the proposed models are often based on the collisionless assumption, justified because the Spitzer-Harm collisional time [124] is much bigger than other dynamical times. However, some important caveats should be explicitly introduced.

Firstly, any collisionless mechanism lacks the ultimate part of the description of the heating process, that is the production of heat related to the irreversible approach towards the thermal equilibrium (i.e. to the dissipation of phase space structures). Several processes (e.g. nonlinear waves) are in

fact able to increase the particle temperature, evaluated as the second order moment of the particle distribution function. However, the free energy contained in the VDFs is not in general converted into heat but it can be also transformed in other forms of ordered energy (e.g. through microinstabilities) [125]. On the other hand, collisions are the unique mechanism able to degrade the information contained in the VDFs free energy into heat by approaching the thermal equilibrium, thus producing heating in the standard thermodynamical sense. Secondly, the evaluation of the Spitzer-Harm collisional time strictly assumes that the VDF shape is close to the Maxwellian. Since this assumption does not often hold in the solar wind [21, 35], the hypothesis on which is based the collisionless assumption may locally fail. Based on these last considerations, numerous studies have been recently conducted in order to take into account collisional effects in a weakly collisional plasma such as the solar wind [49, 62, 63, 126, 127, 128, 129, 130, 131].

In these conditions, kinetic physics and collisions are in competition between each other: the former works to produce deformations of the particle distribution function, while the latter - introduced through a collisional operator at the right hand-sides of the Vlasov equation - tends to restore the equilibrium Maxwellian. The evolution of the plasma is, therefore, the result of the complex combination of these two effects. The choice of the particular collisional operator remains an open problem. Numerous derivations from first principles (e.g. Liouville equation) indicates that the most general collisional operators for plasmas are the Lenard-Balescu operator [54, 55] or the Landau operator [52, 56]. Both operators are nonlinear "Fokker-Planck"-like operators which involve velocity space derivatives and three-dimensional integrals. The Landau operator introduces an upper cut-off of the integrals at the Debye length to avoid the divergence for large impact parameters, while the Balescu-Lenard operator solves this divergence in a more consistent way through the dispersion function. Therefore the Balescu-Lenard operator is more general compared to the Landau operator from this point of view. However, we would remark that both operators are derived by assuming that the plasma is not too far from the thermal equilibrium, hence both operators could lack the description of inter-particle collisions in a strongly turbulent

plasma. Moreover, the numerical approach of the Lenard-Balescu operator is much more difficult than the one of the Landau operator. We also point out that, as far as we know, an explicit derivation of the Boltzmann operator for plasmas starting by the Liouville equation does not still exist [132]. However, although the adoption of the Boltzmann operator for describing collisional effects in plasmas is questionable from a theoretical perspective, it still remains a quite valid options since Boltzmann and Fokker-Planck operators are intrinsically similar [52, 127].

In this perspective, by modeling collisions with the fully nonlinear Landau operator [52], we recently showed that fine velocity space structures are dissipated much faster than global non-thermal features such as temperature anisotropy [49]. In other words, the collisionality can be effectively enhanced by the presence of strong gradients in velocity space and the presence of velocity space fine structures may break the quasi-Maxwellian assumption on which the collisionless approach is based. The entropy production due to the relaxation of the VDF towards the equilibrium occurs on several characteristic times - much smaller than the Spitzer-Harm characteristic time [124]. These characteristic times are associated with the dissipation of particular velocity space structures and could be comparable with other dynamical times (e.g. microinstabilities growth rates). Therefore, collisions could be an additional efficient ingredient to properly describe the irreversible heating observed in the solar wind. Since the presence of such strong velocity space gradients tends to naturally enhance collisionality, high-resolution measurements of the particle VDF in the solar wind are crucial for a proper description of heating mechanisms [133]. Moreover, retaining nonlinearities in the collisional operators is also crucial. In fact, we compared the collisional relaxation of an out-of-equilibrium VDF under the effect of the fully nonlinear Landau operator and of its linearized version. Results indicate that, if one neglects nonlinearities, characteristic dissipation times are significantly larger than in the case of the fully nonlinear operator. The dissipation of such structures gets, therefore, slower by linearizing the collisional operator. It is worth to remark that these results have been obtained in the case of a force-free homogeneous plasma, because the simulations the Landau opera-

tor are highly demanding; hence, they clearly need to be confirmed in the self-consistent case. However, our results, which are highlighted in Chapter 1, are still significant to provide a step forward in the comprehension of a tough problem as heating of the solar wind.

Since the numerical implementation of both Landau and Balescu-Lenard operators is difficult from the computational point of view (e.g. the computational cost of the Landau operator in full phase space is proportional to N^9, being N the gridpoints number along each direction), several simplified operators have been previously employed. We may distinguish these simpler operators in two classes. The first type of operators - as the Bathanar-Gross-Krook [57, 61] and the Dougherty operators [58, 59, 64, 129] - aims to model collisions in the realistic three-dimensional velocity space but by adopting a simpler structure of the operator. On the other hand, the second class of collisional operators works in a reduced, one-dimensional velocity space assuming that the dynamics mainly occur in one direction. Although this approach is "unphysical" (collisions naturally act in three dimensions), these operators can satisfactorily model collisions in laboratory systems, such as the long and thin plasma columns contained in Penning-Malmberg trap devices [62, 63, 134, 135, 136], where the dynamics evolves along only one direction.

In Chapter 2 we focus on the Dougherty operator. First, we compare the Dougherty operator with the Landau operator through a numerical investigation of the relaxation toward equilibrium of a spatially homogeneous plasma in absence of fields, in full three-dimensional geometry in velocity space. Even though the mathematical form of the two collisional operators is evidently different, we found that the collisional evolution of the relevant moments of the particle distribution function (temperature and entropy) are similar in the two cases, once an "ad hoc" time rescaling procedure has been performed. This time rescaling results, in practice, in dividing the collisional frequency in the Dougherty operator by a factor $\alpha \simeq 3.55$, whose value has been determined empirically from the numerical simulations. Then, since the Dougherty operator requires a significantly lighter computational effort with respect to the complete Landau integral, self-consistent plasma simulations

in presence of collisions can be afforded, even in the multi-dimensional phase space geometry. We show results of self-consistent collisional simulations of a plasma composed of kinetic electrons and immobile protons, in a nonlinear regime and in the case of weak collisionality. We focus, in particular, on the concomitant role of collisions and kinetic effects for the cases of i) the linear and nonlinear evolution of the bump-on-tail instability and ii) the excitation of the so-called Kinetic Electrostatic Electron Nonlinear (KEEN) waves [137, 138].

Then, in Chapter 3, we describe the evolution of a weakly-collisional plasma in the reduced $1D$–$1V$ phase space by focusing on two separate problems. First, we study the effect of artificial collisions on the recurrence of the initial states. Collisions are here modeled through the Lenard-Bernstein operator [139]. By decomposing the linear Vlasov-Poisson system in the Fourier-Hermite space, the recurrence problem is investigated in the linear regime of the damping of a Langmuir wave and of the onset of the bump-on-tail instability. The analysis is then confirmed and extended to the nonlinear regime through a Eulerian collisional Vlasov-Poisson code. Despite being routinely used, an artificial collisionality is not a viable way of preventing recurrence in numerical simulations without compromising the kinetic nature of the solution. Moreover, it is shown how numerical effects associated to the generation of fine velocity scales, can modify the physical features of the system evolution even in nonlinear regime. This means that filamentation-like phenomena, usually associated with low amplitude fluctuations contexts, can play a role even in nonlinear regime.

Finally, we analyze the method adopted in laboratory plasmas for triggering fluctuations in both a collisionless and weakly collisional plasma. When exciting Electron Acoustic Waves, we find that a new branch of small amplitude, nonlinear and non dispersive waves is recovered. The generation of these waves is discussed in detail as well as their existence in a weakly collisional plasma. Indeed, also for small collisionality values, these secondary waves are suddenly dissipated, while the main electron-acoustic waves branch undergoes an exponential damping comparable with experimental observations.

Chapter 1

Collisional relaxation of fine velocity structures in plasmas

We discuss here the collisional dissipation of non-Maxwellian features in the particle velocity distribution function in a weakly collisional plasma, by means of Eulerian numerical simulations. Due to the nonlinear nature of the Landau operator, the analytical treatment as well as the self-consistent numerical simulations of the Landau operator in 6D phase space are hard goal to achieve yet. Thus, we decided to address the collisional relaxation of a spatially homogeneous force-free plasma and to model collisions between particles of the same species.

We show here how collisionality effects are increased as the velocity distribution function exhibits strong gradients in velocity space [Section 1.1]. Indeed, fine velocity structures are dissipated much faster compared to global quantities. Furthermore, the explicit comparison of the effects of the nonlinear Landau operator and its linearized version indicates that velocity structures are smoothed out slowly if nonlinearities are neglected. This suggests that taking explicitly into account nonlinearities in the collisional operator is crucial to give the proper importance to collisional effects [Section 1.2].

Results shown here have been awarded with the 2016 "V.C.A. Ferraro" Prize of the Italian Physical Society and have been collected in two scientific papers. The first paper has been recently published in *Physical Review Letter*

[49], while the second one is in press in *Journal of Plasma Physics* [140] as an invited paper for the "V.C.A. Ferraro" Special Issue.

1.1 Collisional relaxation of fine velocity structures in plasmas

The dimensionless Landau equation for the particle distribution function $f(\boldsymbol{v})$ reads as follows:

$$\frac{\partial f(\boldsymbol{v})}{\partial t} = \pi \left(\frac{3}{2}\right)^{\frac{3}{2}} \frac{\partial}{\partial v_i} \int d^3v' \; U_{ij}(\mathbf{u}) \left[f(\boldsymbol{v}') \frac{\partial f(\boldsymbol{v})}{\partial v_j} - f(\boldsymbol{v}) \frac{\partial f(\boldsymbol{v}')}{\partial v'_j} \right] \; , \quad (1.1)$$

being f normalized such that $\int d^3v f(\boldsymbol{v}) = n = 1$ and $U_{ij}(\mathbf{u})$

$$U_{ij}(\mathbf{u}) = \frac{\delta_{ij} u^2 - u_i u_j}{u^3} \; , \quad (1.2)$$

where $\mathbf{u} = \boldsymbol{v} - \boldsymbol{v}'$, $u = |\mathbf{u}|$ and the Einstein notation is introduced. In Eq. (1.1), and from now on, time is scaled to the inverse Spitzer-Harm frequency ν_{SH}^{-1} [124], being $\nu_{SH} \simeq 8 \times (0.714\pi n e^4 \ln\Lambda)/(m^{0.5}(3k_BT)^{3/2})$, and velocity to the particle thermal speed $v_{th} = \sqrt{k_BT/m}$. Note that m, e, n and T are the particle mass, charge, density and temperature, while k_B is the Boltzmann constant and $\ln\Lambda$ is the Coulombian logarithm. Details about the numerical solution of Eq. (1.1) can be found in Ref. [64].

We initially consider the mutual effect of a local deformation of the particle VDF (a plateau) and the global temperature anisotropy, by comparing the evolution of two initial VDFs:

$$f_1(\mathbf{v}) = C_1 f_{M,T_\perp}(v_x) f_{M,T_\perp}(v_y) f_{p,T_\parallel}(v_z) \; , \quad (1.3)$$

$$f_2(\mathbf{v}) = C_1 f_{M,T_\perp}(v_x) f_{M,T_\perp}(v_y) f_{M,T_\parallel}(v_z) \; , \quad (1.4)$$

where C_1 and C_2 are normalization constant. The total temperature T, where $T = v_{th}^2$ in dimensionless units, is given by $T = (T_\parallel + 2T_\perp)/3$ and $A = T_\perp/T_\parallel = 2$. Finally f_{M,T_i} is a generic Maxwellian with temperature T_i

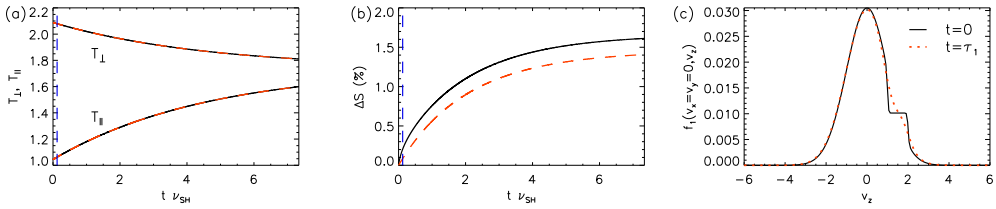

Figure 1.1: (a) Time evolution of $T_\perp$ and $T_\parallel$ for the case of $f_1(\mathbf{v})$ (black-solid line) and $f_2(\mathbf{v})$ (red-dashed line). (b) Time evolution of ΔS for the case of $f_1(\mathbf{v})$ (black-solid line) and $f_2(\mathbf{v})$ (red-dashed line). The vertical blue-dashed line in panels (a)–(b) indicates the time instant $t = \tau_1$. (c) Distribution function $f_1(v_x = v_y = 0, v_z)$ as a function of v_z at $t = 0$ (black-solid line) and at $t = \tau_1$ (red-dashed line).

and [63, 129]:

$$f_{p,T_\parallel}(v_z) = f_{M,T_0}(v_z) - \frac{f_{M,T_0}(v_z) - f_{M,T_0}(V_0)}{1 + [(v_z - V_0)/\Delta V_p]^{n_p}} \tag{1.5}$$

where $T_0 = 1$, $V_0 = 1.44$, $\Delta V_p = 0.5$ and $n_p = 8$. The function $f_{p,T_\parallel}(v_z)$ is constructed in such a way to have a plateau of width ΔV_p around $v = V_0$, that is $f'_{p,T\parallel}(v_z)$ is about null in the interval $V_0 - \Delta V_p/2 <\simeq v_z <\simeq 2V_0 + \Delta V_p/2$, being exactly zero at $v_z = V_0$. Note that the plateau represents one of the most common non-Maxwellian features generated by nonlinear wave-particle interactions.

It is worth to note that $f_1(\mathbf{v})$ is a bi-Maxwellian function, while $f_2(\mathbf{v})$ is Maxwellian in the perpendicular directions with a plateau centered in $v_z = V_0$ in the parallel direction. We also point out that $f_1(\mathbf{v})$ and $f_2(\mathbf{v})$ have the same temperature (second order moment) in each direction. Moreover, for the function $f_1(\mathbf{v})$, we reset the small mean velocity ($\simeq 10^{-2}$) produced by the presence of the plateau. The three-dimensional velocity domain is discretized with $N_{v_x} = N_{v_y} = 51$ and $N_{v_z} = 1601$ grid points. We point out that the resolution along v_z has been increased significantly in order to resolve the short velocity scales associated with the plateau presence. Finally, the distribution function is set equal to zero for $|v_j| > v_{max} = 6v_{th}$, being $j = x, y, z$.

As shown in Fig. 1.1 (a), the time evolution of parallel and perpendicular

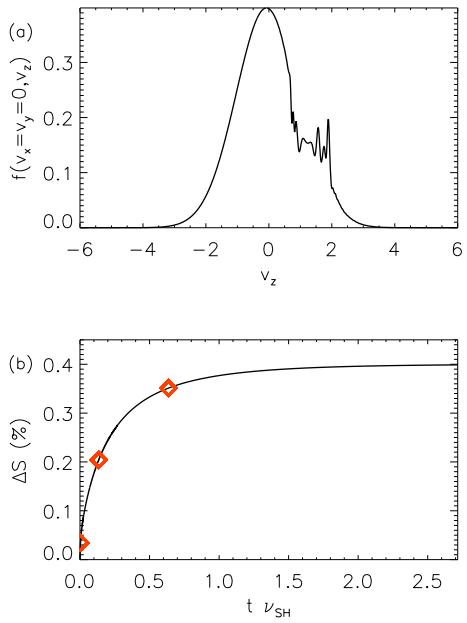

Figure 1.2: (a) Dependence of f_e on v_z. (b) Time history of ΔS. Red dots in panel (b) indicate the time instants $t = \tau_1$, $t = \tau_1 + \tau_2$, $t = \tau_1 + \tau_2 + \tau_3$.

temperatures of $f_1(\mathbf{v})$ (black-solid line) and $f_2(\mathbf{v})$ (red-dashed line) is clearly the same. On the other hand, the evolution of the entropy variation $\Delta S = S(t) - S(0)$ ($S = -\int f \ln f dx dv$), reported in Fig. 1.1(b), displays significant differences. In particular, for $f_1(\mathbf{v})$ (black-solid curve), the case in which a plateau is present, ΔS saturates at a larger level than that recovered for $f_2(\mathbf{v})$ (red-dashed curve). In order to investigate the reasons of such different behavior of the entropy for $f_1(\mathbf{v})$ and $f_2(\mathbf{v})$, we performed a multi-exponential fit [141] of ΔS for the two cases, with the following curve:

$$\Delta S(t) = \sum_{i=1}^{K} \Delta S_i \left(1 - e^{-t/\tau_i}\right) \ , \tag{1.6}$$

τ_i being the i–th characteristic time and K is evaluated through a recursive procedure.

From this analysis, we found that, while for the case of $f_2(\mathbf{v})$ [red-dashed curve of Fig. 1.1(b)] ΔS shows an exponential growth with a single char-

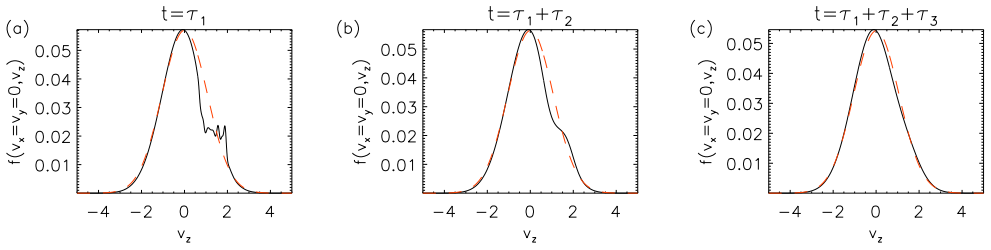

Figure 1.3: Distribution function $f(v_x = 0, v_y = 0, v_z)$ as a function of v_z at $t = \tau_1$ (a), $t = \tau_1 + \tau_2$ (b) and $t = \tau_1 + \tau_2 + \tau_3$ (c). Red dashed lines in panels (a)–(c) indicate the equilibrium Maxwellian finally reached in the simulation.

acteristic time ($\tau \simeq 2\nu_{SH}^{-1}$), for $f_1(\mathbf{v})$ [black-solid curve of Fig. 1.1 (b)], i. e. in the presence of a plateau, two different characteristic times are recovered: a fast characteristic time $\tau_1 = 0.14\nu_{SH}^{-1}$ [indicated in Fig. 1.1(a)–(b) by a vertical blue-dashed line] in which 25% of the total entropy growth is achieved, and a slow characteristic time $\tau_2 = 2.03\nu_{SH}^{-1}$ during which the remaining 75% of the total entropy growth is observed. We argue that the existence of the characteristic time τ_1 is due to the presence of the plateau, and in particular it is associated with the sharp velocity gradients in $f_1(\mathbf{v})$, while τ_2 is related to the initial temperature anisotropy. In fact, as it can be seen in Fig. 1.1(c) where $f_1(v_x = v_y = 0, v_z)$ is plotted as a function of v_z at $t = 0$ (black-solid line) and at $t = \tau_1$ (red-dashed line), the initial plateau is completely smoothed out by collisional effects in a time close to τ_1, while from Fig. 1.1(a) one realizes that at $t \simeq \tau_1$ the temperature anisotropy is still present.

To further support the idea that the presence of sharp velocity gradients in the particle VDF causes the entropy to grow over different time scales, we made an additional numerical experiment of collisional relaxation, considering a different initial condition for Eq. (1.1). This new initial condition has been designed as follows. Firstly, we performed a $1D$–$1V$ Vlasov-Poisson simulation (kinetic electrons and motionless protons) with high numerical resolution in the $z - v_z$ phase space domain ($N_z = 256$, $N_{v_z} = 1601$). In this simulation, we externally forced the system, initially at equilibrium, through a sinusoidal driver electric field, in order to excite a large amplitude elec-

tron acoustic wave (EAW) [142], as it has been done numerically in Refs. [137, 143, 144] and in laboratory experiments with nonneutral plasmas in Refs. [50, 145]. As discussed in these papers, the propagation of large amplitude EAWs is characterized by the generation of phase space structures of the Bernstein-Green-Kruskal (BGK) type [146] in the electron distribution function $f_e(z, v_z)$, associated with trapped particle populations. Then, we selected the spatial point z_0 in the numerical domain, where this BGK-like phase space structure displays its maximum velocity width, and considered the velocity profile $\hat{f}_e(v_z) = f_e(z_0, v_z)$. In Fig. 1.2(a), we report the dependence of $\hat{f}_e$ on v_z; here, it can be appreciated that $\hat{f}_e$ is highly distorted due to nonlinear wave-particle interaction processes and displays the presence of sharp velocity gradients (bumps, holes, spikes etc.). At this point, we evaluated the second order velocity moment of $\hat{f}_e$, that is the temperature T_e, and built up the three-dimensional VDF $f(v_x, v_y, v_z) = f_{M,T_e}(v_x) f_{M,T_e}(v_y) \hat{f}_e(v_z)$. We emphasize that this VDF has the same temperature in each velocity direction, but presents strong non-Maxwellian deformations along v_z, as shown in Fig. 1.2(a), which make the system to be far from equilibrium. The time history of ΔS, obtained when using f_e as initial condition for Eq. (1.1), is presented in Fig. 1.2(b). As in the previous simulations, the three-dimensional velocity domain in this case is discretized by $N_{v_x} = N_{v_y} = 51$ and $N_{v_z} = 1601$ gridpoints.

By analyzing the entropy growth through the same method of multi-exponential fit discussed previously, three characteristic times are recovered in this case, whose values are reported below, together with the corresponding percentage of entropy variation:

- $\tau_1 = 3.5 \cdot 10^{-3} \nu_{SH}^{-1} \rightarrow \Delta S_1 / \Delta S_{tot} = 13\%$
- $\tau_2 = 1.3 \cdot 10^{-1} \nu_{SH}^{-1} \rightarrow \Delta S_2 / \Delta S_{tot} = 42\%$
- $\tau_3 = 4.9 \cdot 10^{-1} \nu_{SH}^{-1} \rightarrow \Delta S_3 / \Delta S_{tot} = 40\%$

Characteristic times τ_1, τ_2 and τ_3 are indicated as red diamonds in Fig. 1.2(b). In Fig. 1.3, we plot f as a function of v_z for $v_x = v_y = 0$, at three different times $t = \tau_1$ (a), $t = \tau_1 + \tau_2$ (b) and $t = \tau_1 + \tau_2 + \tau_3$ (c): during the time

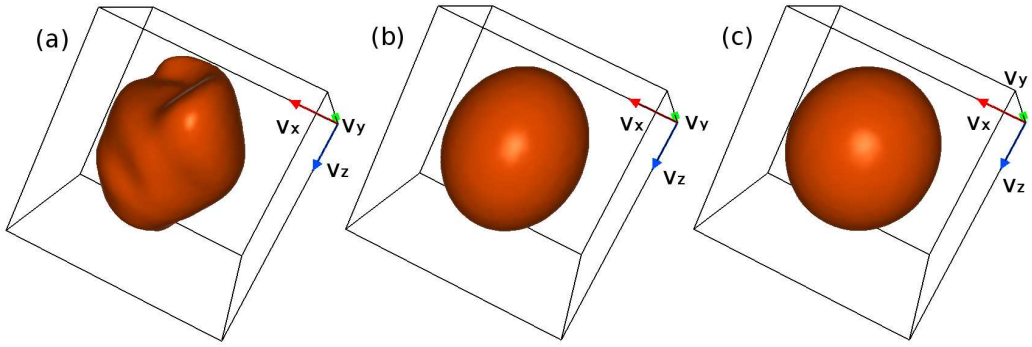

Figure 1.4: Iso-surface plot of the initial VDFs $f_{sw}(\mathbf{v})$ [(a)], $\tilde{f}_{sw}(\mathbf{v})$ [(b)] and $\hat{f}_{sw}(\mathbf{v})$ [(c)], respectively.

τ_1, steep spikes visible in Fig. 1.2(a) are almost completely smoothed out; at time $\tau_1 + \tau_2$ the remaining plateau region is significantly rounded off, only a gentle shoulder being left; finally, after a time $\tau_1 + \tau_2 + \tau_3$, the collisional return to equilibrium is completed for the most part (a small percentage $\simeq 5\%$ of the total entropy growth is finally recovered for larger times and corresponds to the final approach to the equilibrium Maxwellian, indicated by red-dashed lines in the three panels of Fig. 1.3).

Compared to the case shown in Fig. 1.1, here we recovered an additional extremely fast characteristic time ($\simeq 10^{-3}\nu_{SH}^{-1}$), associated with the sharp velocity gradients of f along v_z, while we did not detect the large characteristic time ($\simeq 2\nu_{SH}^{-1}$) associated with the temperature anisotropy in the previous case.

Numerical experiments discussed so far give a clear message: collisional dissipation of small velocity scales in the particle VDF occurs over different time scales, inversely proportional to the sharpness of the velocity gradients associated with those scales. As we discussed above, these characteristic times can be significantly smaller than the Spitzer-Harm collisional time [124], this meaning that the presence of velocity gradients in fact speeds up the growth of the entropy of the system. These evidences suggest that when the particle VDFs exhibit small velocity scale deformations, the quasi-Maxwellian approximation, on which the Spitzer-Harm collisional evolution is based, is no longer appropriate.

In order to explore the implications of our results to the general case of the solar wind plasma, we performed our analysis on a three-dimensional proton VDF $f_{sw}(\mathbf{v})$, obtained from the hybrid Vlasov-Maxwell [40] numerical simulations of solar wind decaying turbulence described in detail in Refs. [30, 31, 33, 35, 41]. As shown in Fig. 1.4(a), where the three-dimensional iso-surface plot of f_{sw} is reported, kinetic effects along the cascade make the VDF depart from the spherical shape of Maxwellian equilibrium and resemble a deformed potato. Then, having in mind to mimic low resolution VDF measurements by a real spacecraft, we fitted $f_{sw}(\mathbf{v})$ with a tri-Maxwellian function $\tilde{f}_{sw}(\mathbf{v})$ [Fig. 1.4(b)] and with a bi-Maxwellian function $\hat{f}_{sw}(\mathbf{v})$ [Fig. 1.4(c)]. In order to point out the loss of physical information caused by not adequately resolving the sharp velocity gradients in the particle VDFs, the functions f_{sw}, $\tilde{f}_{sw}$ and $\hat{f}_{sw}$ are used as initial conditions in three new simulations of Eq. (1.1), in which the velocity domain is now discretized by $N_{v_x} = N_{v_y} = N_{v_z} = 51$ gridpoints, as in the simulations in Refs. [30, 31, 33, 35, 41]. The results for the entropy growth of these new numerical experiments are reported in Fig. 1.5, where we show the time evolution of ΔS for the VDFs $f_{sw}(\mathbf{v})$ (black-solid line), $\tilde{f}_{sw}(\mathbf{v})$ (red-dashed line) and $\hat{f}_{sw}(\mathbf{v})$ (blue-dashed line), respectively.

As for the previous cases discussed above, also here the time history of ΔS is evidently affected by the presence of fine velocity scales and steep

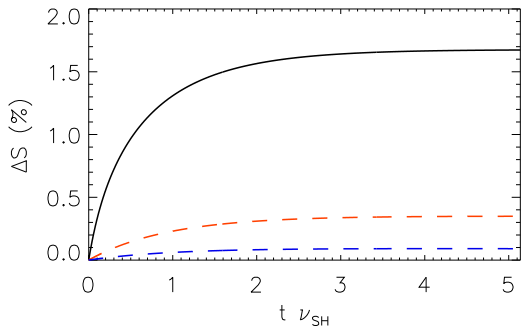

Figure 1.5: Entropy growth for the initial VDFs $f_{sw}(\mathbf{v})$ (black line), $\tilde{f}_{sw}(\mathbf{v})$ (red line) and $\hat{f}_{sw}(\mathbf{v})$ (blue line), respectively.

gradients in the particle VDF. Any fitting procedure, which smooths out the fine velocity structures, reduces the entropy growth: in fact, the simulation with the function $\hat{f}_{sw}(\mathbf{v})$ as initial condition displays a collisional entropy growth about 20 times smaller than that recovered for case of the function $f_{sw}(\mathbf{v})$. Moreover, through the multi-exponential fit analysis performed on ΔS for the simulation initialized with f_{sw}, we found two characteristic times: a fast one $\tau_1 = 0.20\nu_{SH}^{-1}$, in which 26% of the total entropy growth is achieved, and a slow one $\tau_2 = 0.82\nu_{SH}^{-1}$, during which the remaining 74% of the total entropy growth is observed. By analyzing VDF iso-surface plots (not shown here) at different times in the simulation, we realized that after a time $t = \tau_1$ collisions have dissipated most of the sharp velocity gradients which were initially present in the VDF. We point out that, since the numerical resolution for this simulation is about fifty times smaller than in the previous case, sharp velocity gradients [as those shown in Fig. 1.2 (a)] are not visible in the particle VDF, even though it displays significant non-Maxwellian features [see Fig. 1.4 (a)]. Hence, the lack of velocity resolution presumably does not allow to recover the extremely fast characteristic time ($\simeq 10^{-3}\nu_{SH}^{-1}$) in the evolution of ΔS, observed for the simulation initialized with the velocity profile in Fig. 1.2 (a).

1.2 Nonlinear and linearized collisional operators

The second aspect analyzed here concerns the nonlinearities of collisional operators. As introduced above, the Landau operator involves strong nonlinearities and, despite collisional operators are quite often simplified to their linearized versions, it is significant to consider nonlinearities. Indeed, a linearized operator may hide or reduce the importance of velocity space gradients. Therefore, we present a case study where we focus on one of the initial conditions described in the previous section and we compare its evolution, obtained through the fully nonlinear Landau operator and its linearized version, in a force-free homogeneous plasma.

Under these assumptions, we numerically integrate the following dimensionless collisional evolution equations for the particle distribution function $f(\boldsymbol{v},t)$:

$$\frac{\partial f(\boldsymbol{v},t)}{\partial t} = \pi\left(\frac{3}{2}\right)^{\frac{3}{2}}\frac{\partial}{\partial v_i}\int d^3v'\; U_{ij}(\mathbf{u})\left[f(\boldsymbol{v}',t)\frac{\partial f(\boldsymbol{v},t)}{\partial v_j} - f(\boldsymbol{v},t)\frac{\partial f(\boldsymbol{v}',t)}{\partial v'_j}\right] \quad (1.7)$$

$$\frac{\partial f(\boldsymbol{v},t)}{\partial t} = \pi\left(\frac{3}{2}\right)^{\frac{3}{2}}\frac{\partial}{\partial v_i}\int d^3v'\; U_{ij}(\mathbf{u})\left[f_0(\boldsymbol{v}')\frac{\partial f(\boldsymbol{v},t)}{\partial v_j} - f(\boldsymbol{v},t)\frac{\partial f_0(\boldsymbol{v}')}{\partial v'_j}\right] \quad (1.8)$$

being f normalized such that $\int d^3v f(\boldsymbol{v}) = n = 1$ and $U_{ij}(\mathbf{u})$ the projector defined in Eq. (1.2). In Eqs. (1.7–1.8), and from now on, time is scaled to the inverse Spitzer-Harm frequency ν_{SH}^{-1} [124] and velocity to the particle thermal speed v_{th}. Details about the numerical solution of Eqs. (1.7–1.8) can be found in Refs. [49, 64]. Moreover, in Eq. (1.8), f_0 is the three-dimensional Maxwellian distribution function associated with the initial condition of our simulations $f(\boldsymbol{v}, t = 0)$ and built in such a way that density, bulk velocity and temperature of the two distributions $f(\boldsymbol{v}, t = 0)$ and $f_0(\boldsymbol{v})$ are the same. Clearly the two equations differ because Eq. (1.7) refers to the nonlinear Landau operator, already adopted in Sect. 1.1, while Eq. (1.8) evolves the linearized Landau operator, obtained by linearizing the Fokker-Planck coefficients of Eq. (1.7). Velocity domain discretization and boundary conditions are the same as in the previous section.

For the current simulations, we chose as initial condition one of the initial conditions adopted in the previous section. In particular, we selected the one obtained as a cut of a $1D$–$1V$ Vlasov-Poisson simulation where KEEN waves are triggered. The shape of the $1V$ cut of the particle distribution function can be appreciated in Fig. 1.2(a). We remark that this VDF does not initially exhibit any temperature anisotropy but it still shows strong non-Maxwellian deformations along v_z, due to the presence of trapped particles.

Figure 1.6 reports the temporal evolution of the entropy variation $\Delta S = S(t) - S(0)$ ($S = -\int f \ln f d^3v$), which gives information about the approach towards equilibrium. Black and red lines respectively refer to the case of the fully nonlinear Landau operator and the linearized operator. Since the initial condition is the same for both operators, the total growth of entropy ΔS is

the same in terms of absolute values. In the case where nonlinearities are taken into account the entropy grows much faster compared to the linearized operator case. Indeed, in the case of the full Landau operator, the total entropy growth is reached in about $1 \div 2\nu_{SH}^{-1}$; while, for the linearized Landau operator, the entropy grows on $4 \div 5\nu_{SH}^{-1}$.

To better point out how the dissipation of fine velocity space structures is affected by the presence of the nonlinearities, we performed the multi-exponential fit of ΔS presented in the previous section [49, 141]. When collisions are modeled by means of the fully nonlinear Landau operator, we already found that three characteristic times are recovered:

- $\tau_1^{nl} = 3.5 \cdot 10^{-3}\, \nu_{SH}^{-1} \rightarrow \Delta S_1^{nl}/\Delta S_{tot} = 13\%$
- $\tau_2^{nl} = 1.3 \cdot 10^{-1}\, \nu_{SH}^{-1} \rightarrow \Delta S_2^{nl}/\Delta S_{tot} = 42\%$
- $\tau_3^{nl} = 4.9 \cdot 10^{-1}\, \nu_{SH}^{-1} \rightarrow \Delta S_3^{nl}/\Delta S_{tot} = 40\%$

As discussed in the previous Section, the presence of several characteristic times is associated with the dissipation of different velocity space structures. Fig. 1.7 reports $f(v_x = v_y = 0, v_z)$ as a function of v_z at the time instants

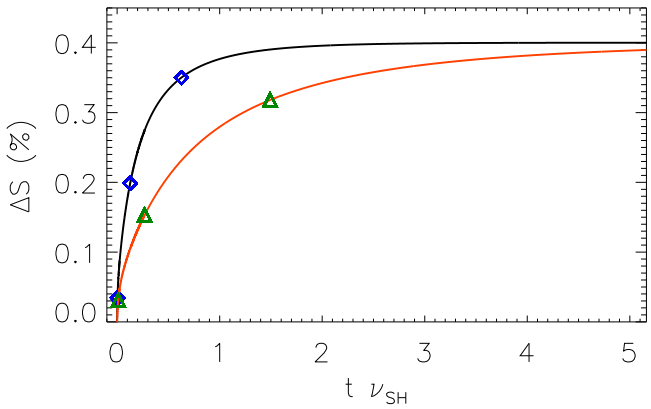

Figure 1.6: (Color online) Time history of ΔS in the case of the fully nonlinear Landau operator (black) and the linearized Landau operator (red). Blue diamonds indicate the time instants $t = \tau_1^{nl}$, $t = \tau_1^{nl} + \tau_2^{nl}$ and $t = \tau_1^{nl} + \tau_2^{nl} + \tau_3^{nl}$; the green triangles refer to $t = \tau_1^{lin}$, $t = \tau_1^{lin} + \tau_2^{lin}$ and $t = \tau_1^{lin} + \tau_2^{lin} + \tau_3^{lin}$.

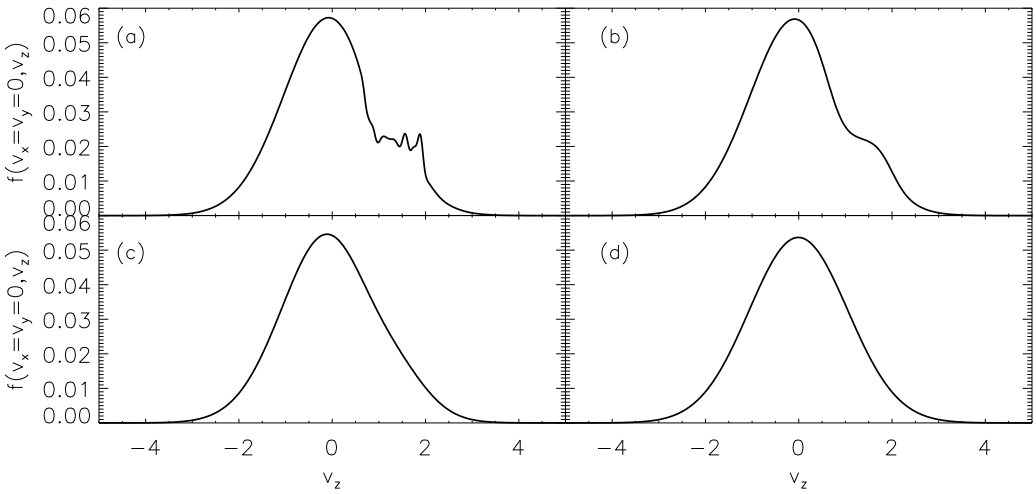

Figure 1.7: Distribution function $f(v_x = 0, v_y = 0, v_z)$ as a function of v_z, obtained in the case of the fully nonlinear Landau operator. Panels from (a) to (d) respectively display the time instants $t = \tau_1^{nl}$ (a), $t = \tau_1^{nl} + \tau_2^{nl}$ (b), $t = \tau_1^{nl} + \tau_2^{nl} + \tau_3^{nl}$ (c) and $t = t_{fin}$ (d).

$t = \tau_1^{nl}$ (a), $t = \tau_1^{nl} + \tau_2^{nl}$ (b), $t = \tau_1^{nl} + \tau_2^{nl} + \tau_3^{nl}$ (c) and $t = t_{fin}$ (d). These time instants are displayed in Fig. 1.6 with blue diamonds.

The same analysis performed in the case of the linearized Landau operator (red line of Fig. 1.6) indicates that, as in the nonlinear operator case, three characteristic times are obtained. The values of these characteristic times are, however, much different compared to the ones previously recovered:

- $\tau_1^{lin} = 1.1 \cdot 10^{-2}\, \nu_{SH}^{-1} \rightarrow \Delta S_1^{lin}/\Delta S_{tot} = 11\%$
- $\tau_2^{lin} = 2.7 \cdot 10^{-1}\, \nu_{SH}^{-1} \rightarrow \Delta S_2^{lin}/\Delta S_{tot} = 23\%$
- $\tau_3^{lin} = 1.5 \qquad \nu_{SH}^{-1} \rightarrow \Delta S_3^{lin}/\Delta S_{tot} = 63\%$

Moreover, when looking at the evolution of the distribution function, one can easily figure out that this is qualitatively similar to the case of the fully nonlinear operator. Fig. 1.8(a–d) reports $f(v_x = v_y = 0, v_z)$ as a function of v_z at the time instants $t = \tau_1^{lin}$ (a), $t = \tau_1^{lin} + \tau_2^{lin}$ (b), $t = \tau_1^{lin} + \tau_2^{lin} + \tau_3^{lin}$ (c) and $t = t_{fin}$ (d). These time instants are displayed in Fig. 1.6 with green triangles. As recovered in the fully nonlinear operator case, the initial

spikes in the initial condition are flattened after the time $t = \tau_1^{lin}$ (a). Then, at $t = \tau_1^{lin} + \tau_2^{lin}$ (b), the plateau is rounded off. Finally, after a time $t = \tau_1^{nl} + \tau_2^{nl} + \tau_3^{nl}$ (c), the collisional relaxation to equilibrium is almost completed and a very small percentage $\simeq 3\%$ of the total entropy growth is finally recovered for larger times and corresponds to the final approach to the equilibrium Maxwellian (d).

Since several characteristic times are recovered in both cases, we can argue that fully nonlinear and linearized operators are both able to recover the characteristic that fine velocity space structures are dissipated faster as their scale gets finer (e.g. as the velocity space gradients become stronger). However, the speed at which such structures are smoothed out is significantly weakened if one neglects nonlinearities: each characteristic times recovered in the case of a linearized operator is significantly bigger (about $2 \div 5$ times) than the correspondent characteristic times recovered with the fully nonlinear operator. It is also worth mentioning that the amount of entropy production due to different velocity structures also changes by ignoring nonlinearities: in the case of the fully nonlinear Landau operator about 55% of the total

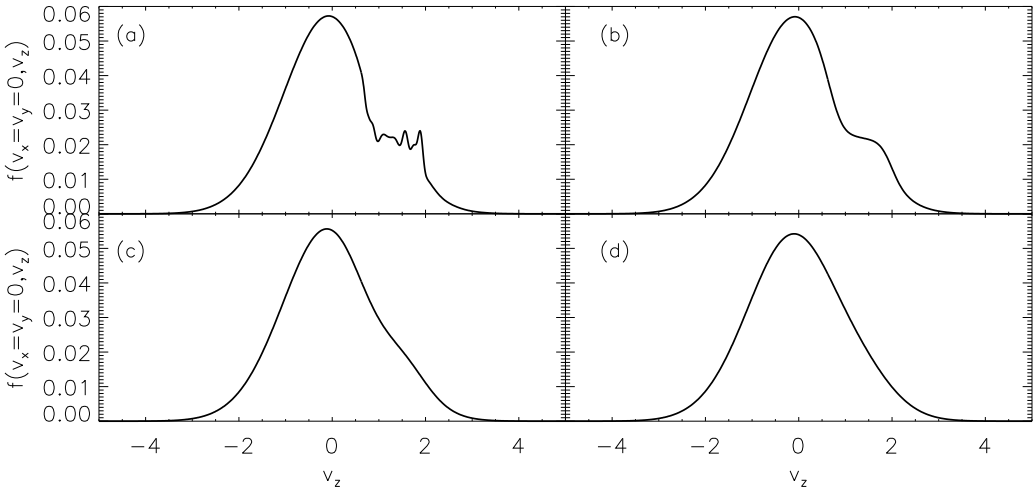

Figure 1.8: Distribution function $f(v_x = 0, v_y = 0, v_z)$ as a function of v_z, obtained in the case of the linearized Landau operator. Panels from (a) to (d) respectively display the time instants $t = \tau_1^{lin}$ (a), $t = \tau_1^{lin} + \tau_2^{lin}$ (b), $t = \tau_1^{lin} + \tau_2^{lin} + \tau_3^{lin}$ (c) and $t = t_{fin}$ (d).

entropy is due to the dissipation of the initial spikes and to the rounding of the successive plateau, while - in the linearized operator case - only about the 30% of the total entropy is due to these two processes. Hence a significant difference between the two operators is recovered and, bearing in mind to compare the collisional characteristic times with other dynamical times, it is fundamental to properly attribute the importance of collisions by taking into account the nonlinearities present in the collisional integral.

1.3 Summary

To summarize, we here discussed the role of the VDF fine velocity structures in enhancing the plasma collisionality. In particular, by means of Eulerian simulations of collisional relaxation of a spatially homogeneous force-free plasma, we have shown that the system entropy growth occurs over several time scales, which gets smaller as VDF gradients become steeper. We reported clear evidences that these gradients are dissipated by collisions in a time much shorter than that associated with global non-Maxwellian features, e.g. temperature anisotropies. This characteristic time may be comparable or even smaller than the instability growth rates invoked to explain the SW anisotropic VDFs [147, 148] or than the nonlinear dynamics times, as recently discussed through a classical treatment of collisions [131]. We finally pointed out how the lacks of resolution in the VDFs measurements mask a relevant part of physical information hidden in the sharp velocity gradients of the non-Maxwellian VDFs, observed ubiquitous, for example, in the SW [21, 25]. Future space missions, planned to increase both energy and angular resolutions of the VDFs measurements, will provide crucial insights for the longstanding problems of plasma heating and particle energization in the interplanetary medium.

Moreover, focusing on the comparison of the full Landau operator and its linearized version, we showed that both nonlinear and linearized collisional operators are able to detect the presence of several time scales associated with the collisional dissipation of small velocity scales. This can be explained by the fact that the linearized operators also involve derivatives while do

not take into account the "second-order" gradients related to the Fokker-Planck coefficients of the Landau operator, which may influence the absolute value of such times. For both evolutions, the recovered characteristic times are significantly smaller than the Spitzer-Harm collisional time [124], this meaning that the presence of sharp velocity space gradients speeds up the entropy growth of the system. However, the importance of such characteristic times is significantly affected and, in general, weakened if nonlinearities are ignored in the collisional operator. In the case of a linearized collisional operator, one obtains much slower characteristic times with respect to the case where operator nonlinearities are taken into account. Therefore, we conclude that the presence of nonlinearities in the collisional operator should be taken into account, since it may affect the relevance of fast characteristic times - associated with the collisional relaxation of fine velocity structures - with respect to other dynamical times [131, 147, 148].

Chapter 2

Collisional effects described through simplified collisional operators: the Dougherty operator

As described in the Introduction of the current part of this thesis, self-consistent collisional simulations where collisions are modeled by the fully nonlinear Landau operator cannot be easily performed due to the computational cost of the Landau integral. Therefore, simplified collisional operators are usually considered to model collisionality. Here we focus on the Dougherty operator, which has been proposed by Dougherty in 1964 to describe collisions among particles of the same species in $3D$–$3V$ physical systems [58, 59].

Even though the Dougherty operator has been set up in a phenomenological way, it satisfies the main properties of a good collisional operator [134, 135]:

- it vanishes for any thermal equilibrium distribution function and it displays the Maxwellian distribution function as a long-time limit solution;
- it conserves particle number, momentum and energy;

- it describes the dominance of small-angle scattering through a velocity-space diffusion term.

However, since the Dougherty operator is explicitly phenomenological and it has not been formally derived from the Landau collisional operator, firstly it could give rise to evolution times which can be different from those predicted by the Landau operator by some numerical factor and secondly it does not describe the velocity dependence of the diffusion coefficients in velocity space. Note that the Dougherty operator is significantly less time demanding than the full Landau collisional integral. In fact, the computational time t_c for $1D$–$3V$ ($1D$ in physical space and $3D$ in velocity space) Eulerian simulations which include the full Landau operator scales as $t_c \sim N^7$ (where N is the number of gridpoints, assumed, for simplicity, to be the same for each phase-space coordinate); for the Dougherty operator, the scaling is $t_c \sim N^4$; this significant reduction of t_c allows to run numerical experiments of the self-consistent electrostatic dynamics of a collisional plasma in $1D$–$3V$ geometry.

For this reason, in Sections 2.1 and 2.2, we try to face the first problem by analyzing the behavior of the Dougherty operator [58], as compared to that of the complete Landau integral, through a numerical investigation of the relaxation toward equilibrium of a spatially homogeneous plasma in absence of fields, in full three-dimensional geometry in velocity space. To perform this analysis, we describe numerically the return to equilibrium of several non-Maxwellian velocity distributions, and compare quantitatively the time evolution of the velocity distribution itself and of temperature and entropy. Interestingly enough, for the cases discussed in this thesis, the system evolution obtained when collisions are modeled through the Dougherty operator results very similar to the case where the full Landau integral is employed, provided an "ad hoc" time rescaling is performed. This time rescaling results, in practice, in dividing the plasma parameter g in the Dougherty operator by a factor $\alpha \simeq 3.55$, whose value has been determined empirically from the numerical simulations. We point out that, due to the computational cost of the numerical approximation of the Landau integral, this analysis could not be performed in situations of self-consistent plasma evolution, not even in electrostatic approximation.

In Section 2.3, once the relationship between the Landau and Dougherty operators has been established, we employ the Dougherty operator to model particle collisions, rescaling the plasma parameter as discussed above and making the assumption that this procedure works to mimic the Landau integral also in self-consistent electrostatic situations. We analyze two cases of the electrostatic dynamics of a plasma composed of kinetic electrons and immobile protons, in a nonlinear regime and in the case of weak collisionality. We focus, in particular, on the concomitant role of collisions and kinetic effects in shaping the particle distribution function, which, in turn, determines the plasma evolution. We performed our analysis in two specific cases: the linear and nonlinear evolution of the bump-on-tail instability and the excitation of KEEN waves [137, 138]. We emphasize that our numerical results can be relevant for laboratory plasma experiments, in which collisional effects are weak but often not negligible. We point out also that our numerical simulations retain only electron-electron collisions, neglecting electron-proton interactions and electron collisions with heavy particles [56].

Results shown here have been collected in two scientific papers recently published in *Journal of Plasma Physics* [64] and *Physics of Plasmas* [129].

2.1 Landau and Dougherty collisional operators

We consider here the collisional relaxation of a plasma in presence of collisions among particles of the same species (electron-electron or ion-ion). We assume that the plasma is spatially homogeneous and no field (self-consistent or external) is present.

The explicit form of the Landau operator, in dimensionless units, is the following:

$$\left.\frac{\partial f}{\partial t}\right|_{coll} = \frac{g \ln \Lambda}{8\pi} \frac{\partial}{\partial v_i} \int d^3v' \; U_{ij}(\mathbf{u}) \left[f(\boldsymbol{v}') \frac{\partial f(\boldsymbol{v})}{\partial v_j} - f(\boldsymbol{v}) \frac{\partial f(\boldsymbol{v}')}{\partial v'_j} \right] , \qquad (2.1)$$

$f(\boldsymbol{v})$ being the particle distribution function, normalized such as $\int d^3v \, f(\boldsymbol{v}) =$

$n = 1$, $g = 1/n\lambda_D^3$ the plasma parameter, $\ln\Lambda \simeq -\ln g/3$ the Coulombian logarithm and $U_{ij}(\mathbf{u})$ the projector

$$U_{ij}(\mathbf{u}) = \frac{\delta_{ij}u^2 - u_i u_j}{u^3} \ , \tag{2.2}$$

where $\boldsymbol{u} = \boldsymbol{v} - \boldsymbol{v}'$ and $u = |\boldsymbol{u}|$. For brevity and clarity, we avoided to explicitly indicate the time dependence of the distribution function f. Moreover, the Einstein summation notation has been introduced.

The dimensionless Dougherty operator is the following:

$$\left.\frac{\partial f}{\partial t}\right|_{coll} = \frac{g\ln\Lambda}{8\pi}\frac{n}{T^{3/2}}\frac{\partial}{\partial v_j}\left[T\frac{\partial f(\boldsymbol{v})}{\partial v_j} + (v-V)_j\, f(\boldsymbol{v})\right] \ . \tag{2.3}$$

where $n = \int d^3v f(\boldsymbol{v}) = 1$, $\mathbf{V} = 1/n\int d^3v\ \mathbf{v}f(\boldsymbol{v})$, $T = 1/3n\int d^3v(v - V)^2 f(\boldsymbol{v})$ respectively the density, the mean velocity and the temperature of the plasma.

In the previous equations, time is scaled to the inverse plasma frequency ω_p, lengths to the Debye length λ_D and velocities to the thermal speed v_{th}. From now on, all physical quantities will be scaled with these characteristic parameters.

It is worth to remark that both operators exhibit a similar Fokker-Planck structure, weighted with different coefficients, satisfy conservation of mass, energy and momentum and obeys an H-theorem [58, 59, 149].

By looking at Eqs. (2.1)-(2.3), one can realize that the projector $U_{ij}(\mathbf{u})$ that couples the velocity $\boldsymbol{v}$, at which the Landau collisional operator is evaluated, and the integration variable $\boldsymbol{v}'$ is absent in the Dougherty operator. This significantly simplifies the numerical solution, since the velocity integrals in the Dougherty operator (n, U and T) can be evaluated once for each time step in the simulation. In the case of spatially homogeneity, this reduces the computational cost from N^6 (Landau operator) to N^3 (Dougherty operator); for the general non-homogeneous case with three dimensions in physical space, the computational cost decreases from N^9 (Landau operator) to N^6 (Dougherty operator).

2.2 Relaxation toward equilibrium: a numerical comparison

To begin this section, we shortly discuss the numerical strategy adopted to solve the collisional time evolution equation for the particle distribution function:

$$\frac{\partial f}{\partial t} = \left.\frac{\partial f}{\partial t}\right|_{coll} , \tag{2.4}$$

where $\partial f/\partial t|_{coll}$ is given by Eq. (2.1) for the case of the Landau operator and by Eq. (2.3) for the Dougherty operator. We will refer to Eq. (2.4) as the Landau or the Dougherty equation, depending on which collisional operator is used in the right-hand side.

The velocity derivatives in both Landau and Dougherty operator are evaluated numerically through a sixth-order centered finite difference scheme [62, 63], while for the time derivative a first-order Eulerian scheme has been employed. The explicit expressions of the schemes for the velocity derivatives are the following:

$$\left.\frac{\partial f}{\partial v_j}\right|_i = \frac{-f_{i-3} + 9f_{i-2} - 45f_{i-1} + 45f_{i+1} - 9f_{i+2} + f_{i+3}}{60\Delta v_j} \tag{2.5}$$

$$\left.\frac{\partial^2 f}{\partial v_j^2}\right|_i = \frac{2f_{i-3} - 27f_{i-2} + 270f_{i-1} - 490f_i + 270f_{i+1} - 27f_{i+2} + 2f_{i+3}}{180\Delta v_j^2} \tag{2.6}$$

i being a generic grid point along the velocity direction j and Δv_j the mesh size along the j-th velocity direction.

In the numerical velocity domain, f is set equal to zero for $|\boldsymbol{v}| > v_{max}$, where $v_{max} = 6v_{th,m}$ along each direction, where $v_{th,m} = \max\{v_{th,\parallel}, v_{th,\perp}\}$. The number of grid points used to discretize the velocity numerical domain has been chosen such that the ratio $\Delta v_j/v_{th,j}$ is almost constant for $j = x, y, z$. We typically use 101 grid points in v_z and 51 grid points in v_x and v_y.

The time step Δt is chosen in such a way to satisfy the Courant-Friedrichs-Levy condition for the numerical stability of time explicit finite difference schemes [150].

In the following Subsections, we will describe the comparison between

Landau and Dougherty operators in different cases, i. e., initializing the computation with different initial particle velocity distributions. In Sec. 2.2.1 the evolution of a bi-Maxwellian velocity distribution is discussed. Then, in Sec. 2.2.2 we analyze the relaxation of velocity distributions with a plateau and a beam along one velocity direction. Finally, in Sec. 2.2.3, the evolution of a more "distorted" velocity distribution, which comes out from a self-consistent $1D$–$1V$ Vlasov-Poisson simulation of nonlinear wave-particle interaction, is discussed.

2.2.1 Bi-Maxwellian velocity distribution

We consider the following bi-Maxwellian non-drifting velocity distribution:

$$f(v_x, v_y, v_z) = \frac{1}{(2\pi)^{3/2} T_\perp \sqrt{T_\parallel}} \exp\left[-\left(\frac{v_x^2}{2T_\perp} + \frac{v_y^2}{2T_\perp} + \frac{v_z^2}{2T_\parallel}\right)\right] . \tag{2.7}$$

Here, the subscript $\parallel$ indicates the z direction, while x and y are the perpendicular ($\perp$) directions. We define the temperature anisotropy as $A = T_\perp / T_\parallel$.

From the analytical point of view, by assuming that the distribution function remains a bi-Maxwellian during the process of collisional relaxation, one can integrate Eq. (2.4) in the case of both Landau and Dougherty operators to obtain the evolution equation for parallel and perpendicular temperatures.

In the case of the Landau operator [151], one gets:

$$\frac{dT_\perp}{dt} = -\nu_{_L} \left(T_\perp - T_\parallel\right) , \tag{2.8}$$

$$\frac{dT_\parallel}{dt} = 2\nu_{_L} \left(T_\perp - T_\parallel\right) ; \tag{2.9}$$

ν_T being a thermalization frequency given by:

$$\nu_{_L} = \frac{g \ln \Lambda}{8\pi^{3/2} T_\parallel^{3/2}} \frac{-3 + \left(\tilde{A} + 3\right) \varphi(\tilde{A})}{\tilde{A}^2} , \tag{2.10}$$

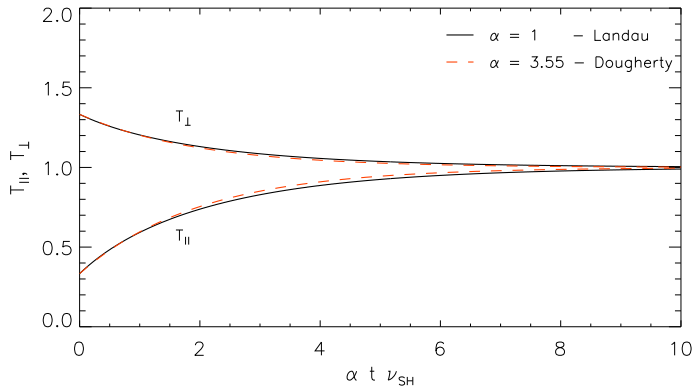

Figure 2.1: (Color online) Time evolution of parallel and perpendicular temperatures obtained from Eqs. (2.8)−(2.9) (black solid lines) and Eqs. (2.12)−(2.13) (red dashed lines). The initial anisotropy is $A = 4$ and the plasma parameter $g = 10^{-2}$.

where $\tilde{A} = A - 1$ and

$$\varphi(x) = \begin{cases} \tan^{-1}(\sqrt{x})/\sqrt{x} & x > 0 \\ 1 & x = 0 \\ \tanh^{-1}(\sqrt{-x})/\sqrt{-x} & x < 0 \end{cases} \tag{2.11}$$

It is worth noting that, in Eqs. (2.8)−(2.9), the total temperature $T = (2T_\perp + T_\parallel)/3$ remains constant in time.

In the same way, for the case of the Dougherty operator, one can easily get:

$$\frac{dT_\perp}{dt} = -\frac{2\nu_{_D}}{3}\left(T_\perp - T_\parallel\right) \quad , \tag{2.12}$$

$$\frac{dT_\parallel}{dt} = 2\frac{2\nu_{_D}}{3}\left(T_\perp - T_\parallel\right) \quad ; \tag{2.13}$$

$\nu_{_D}$ being a thermalization frequency written as:

$$\nu_{_D} = \frac{g\ln\Lambda}{8\pi}\frac{n}{T^{3/2}} \ . \tag{2.14}$$

For the case of the Dougherty operator an evolution equation for the entropy

$S = -\int d^3v f \ln f$ can be easily deduced, and reads:

$$\frac{dS}{dt} = n\nu_{_D} \left[T \frac{T_\perp + 2T_\parallel}{T_\perp T_\parallel} - 3 \right] . \tag{2.15}$$

Figure 2.1 shows the time evolution of parallel and perpendicular temperatures obtained from Eqs. (2.8)−(2.9) (black solid lines) and from Eqs. (2.12)−(2.13) (red dashed lines). In this specific case the initial anisotropy is $A = 4$, while the value of the plasma parameter is $g = 10^{-2}$. In this plot, time is normalized to the inverse Spitzer-Harm frequency [124] ν_{SH}, that is the characteristic collisional frequency for relaxation processes in plasmas, and rescaled by a factor α. The value of α is set equal to 1 in the case of the Landau operator, while in the case of the Dougherty operator it is determined numerically in such a way to minimize the following function:

$$\sigma(\alpha) = \sqrt{\frac{1}{t_{max}} \int_0^{t_{max}} \left\{ \left[T_\parallel^{(L)}(t) - T_\parallel^{(D)}(\alpha t) \right]^2 + \left[T_\perp^{(L)}(t) - T_\perp^{(D)}(\alpha t) \right]^2 \right\} dt} \tag{2.16}$$

where t_{max} is the time at which the thermal equilibrium is established. This procedure gives $\alpha = 3.55$ for the Dougherty operator.

It is worth noting that rescaling the time by $\alpha = 3.55$ in the case of the Dougherty operator corresponds to rescaling the thermalization frequency $\nu_{_D}$ by $1/\alpha$; in other words, the collisional effect of the Dougherty operator is made "slower" than it would be originally.

As it is clear from Fig. 2.1, when rescaling the time as explained above, the evolution of perpendicular and parallel temperatures obtained through the Landau equations (2.8)−(2.9) and the Dougherty equations (2.12)−(2.13) looks closely similar for many Spitzer-Harm times. We have checked that the value of the rescaling factor α does not depend on the value of g.

The analytical predictions for the time evolution of $T_\perp$ and $T_\parallel$ provide excellent benchmarks to check the direct numerical solution of Eq. (2.4). Therefore we solved numerically Eq. (2.4) in the case of the Landau operator and of the Dougherty operator, through the Eulerian algorithm shortly

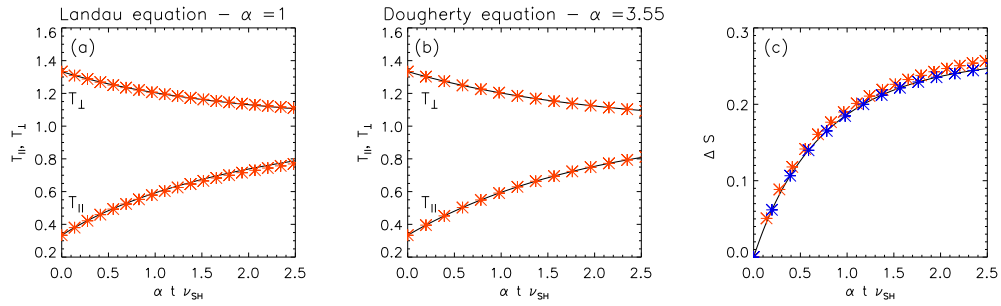

Figure 2.2: (Color online) (a) Time evolution of the parallel and perpendicular temperatures for the Landau operator case. The black solid line represents the time evolution of the moments equations [Eqs. (2.8)−(2.9)], while the red dots correspond to the time evolution of the temperatures obtained from the numerical evolution of Eq. (2.4). (b) Time evolution of the parallel and perpendicular temperatures for the Dougherty operator case. The black solid line represents the time evolution of the moments equation [Eqs. (2.12)−(2.13)], while the red dots correspond to the time evolution of the temperatures obtained from the numerical evolution of Eq. (2.4). (c) Time evolution of the entropy growth obtained from Eq. (2.15) and from the numerical evolution of the Eq. (2.4) for the case of the Landau operator (red dots) and the Dougherty operator (blue dots), respectively.

presented previously. Then, we compared the results of these simulations for the evolution of $T_\perp$ and $T_\parallel$ with the theoretical solutions. In these direct simulations the initial condition for the velocity distribution is given by Eq. (2.7) with $A = 4$ and the plasma parameter is $g = 10^{-2}$.

In Fig. 2.2 (a) the evolution of $T_\perp$ and $T_\parallel$ is reported for the case in which the Landau operator is used in the right-hand side of Eq. (2.4). The analytical curves from Eqs. (2.8)−(2.9) are indicated as black solid lines, while the results of the direct simulation as red stars. In the same way, Fig. 2.2 (b) shows the comparison between theory and numerical results for the case of the Dougherty operator. In both cases we get a very good agreement between analytical and numerical results. Again, the time scaling factor is $\alpha = 1, 3.55$ for the case of the Landau operator and of the Dougherty operator respectively.

Finally, in Fig. 2.2 (c) we report the entropy growth obtained through the direct simulation of Eq.(2.4), in the case of the Landau operator (red stars), of the Dougherty operator (blue stars). The black solid line indicates the

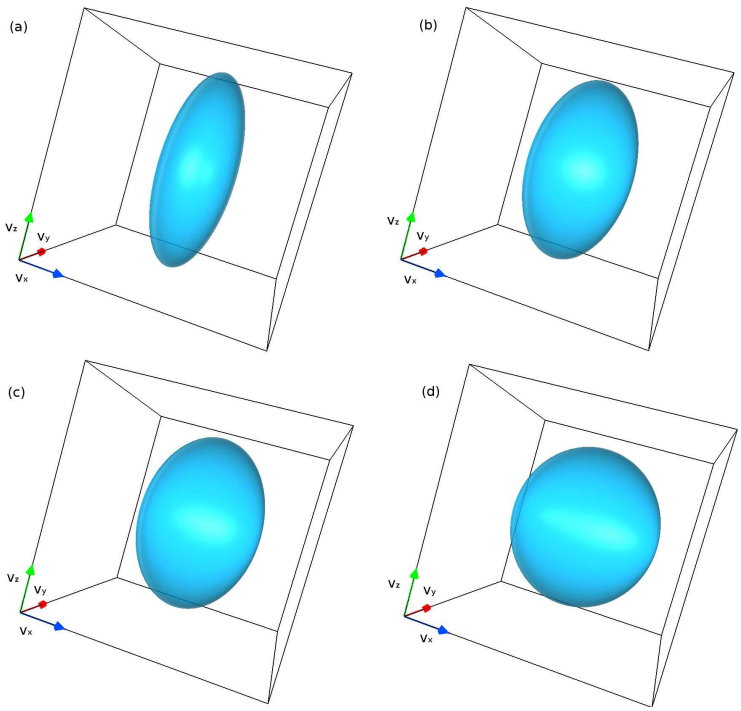

Figure 2.3: (Color online) Snapshot (iso-contour levels) of the distribution function in the whole 3V space at four different times: $\alpha\ t_1\ \nu_{SH} = 0.00$ (a), $\alpha\ t_2\ \nu_{SH} = 0.70$ (b), $\alpha\ t_3\ \nu_{SH} = 1.38$ (c) and $\alpha\ t_4\ \nu_{SH} = 4.13$ (d).

analytical solution from the time evolution of S from Eq. (2.15). Here, we point out that at time $t \simeq 1.5\nu_{SH}^{-1}$ the Landau solution slightly departs from the Dougherty solution even when time is rescaled by the factor $\alpha = 3.55$. A better agreement has been recovered for $\alpha = 3.35$. It is worth noting that, in both cases, the final temperature and the total entropy growth are in agreement with the thermodynamical prediction on the final temperature and on the entropy variation between the initial condition (three Maxwellian distribution functions with different temperatures considered as isolated systems) and the equilibrium distribution functions at saturation (three Maxwellian distribution functions with the same temperature). This shows that the numerically produced entropy variation is negligible with respect to the entropy variation produced by the collisional terms.

Eulerian algorithms allow for a clean description (almost noise-free) of the velocity distribution. Figures 2.3 (a)-(d) show four snapshots of the velocity

distribution at four different times for a Dougherty simulation of Eq. (2.4) with initial anisotropy $A = 8$ and $g = 10^{-2}$. The sequence of plots illustrates how collisions work to restore the spherical shape of the velocity distribution, which corresponds to the isotropic Maxwellian configuration.

2.2.2 Plateau and Beam velocity distributions

In order to investigate whether the time rescaling procedure allows in general to reproduce the collisional Landau relaxation through the simplified Dougherty operator, in this Section we follow numerically the collisional evolution of velocity distributions with sharp gradients in one velocity direction. In particular, we considered a velocity distribution with a plateau along v_z (f_p) at $t = 0$ and a velocity distribution with a beam along v_z (f_b) at $t = 0$. This kind of velocity distributions are usually generated by resonant wave-particle interaction processes and are very common features recovered, for example, in solar-wind spacecraft observations [21] and in laboratory plasma experiments [143, 152].

For these new set of simulations the plasma parameter is $g = 10^{-2}$. The explicit expressions of the initial velocity distributions are:

$$f_p(v_z) = f_0(v_z) - \left[f_0(v_z) - f_0(v_p)\right] \cdot \left[1 + \left(\frac{v_z - v_p}{dv_p}\right)^{m_p}\right]^{-1} \quad (2.17)$$

$$f_b(v_z) = f_0(v_z) + \frac{n_b}{\sqrt{2\pi T_b}} \exp\left[-\frac{(v_z - V_b)^2}{2T_b}\right] \quad (2.18)$$

being $f_0(v_z) = 1/\sqrt{2\pi}\ \exp[-v_z^2/2]$, $v_p = 1.44$, $m_p = 8$, $dv_p = 0.5$ and $n_b = 0.17$, $V_b = 2.2$ and $T_b = 0.1$.

Figure 2.4 (a)-(b) show the initial velocity distributions f_p and f_b, respectively. Panels (c)-(d) in the same figure display the time evolution of S obtained through the Landau operator (black solid line) and through the Dougherty operator (red stars), for the initial conditions f_p and f_b respectively. The rescaling factor is given the value $\alpha = 1, 3.55$ for the Landau operator and the Dougherty operator, respectively. We note that, for the plateau initial condition f_p, the Landau solution and the Dougherty solu-

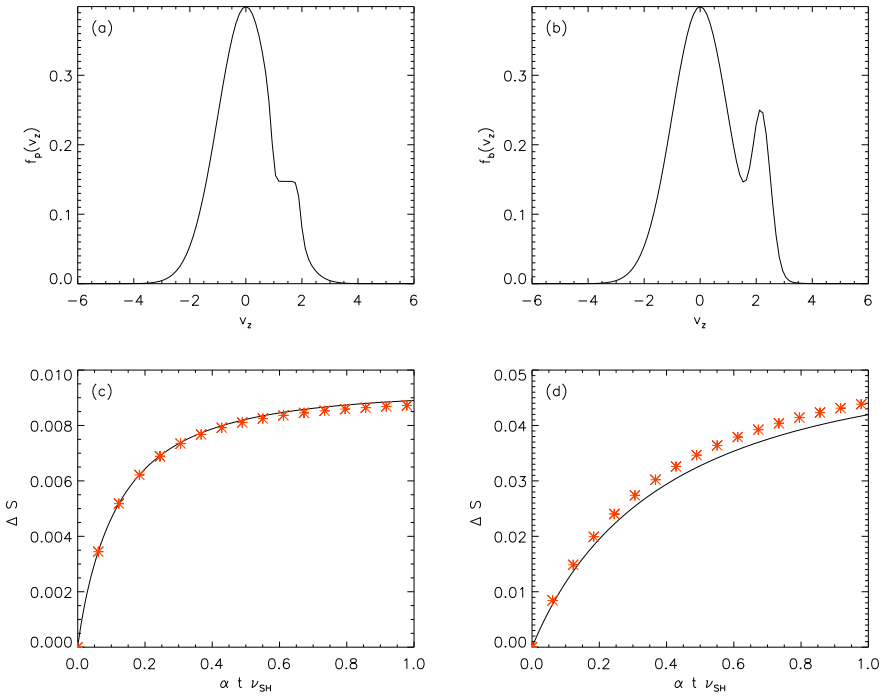

Figure 2.4: (Color online) In the top row, the initial velocity distributions functions along v_z are shown for the plateau case [Eq. (2.17)] (a) and for the beam case [Eq. (2.18)] (b). In the bottom row, the entropy growth is presented for the Landau operator (black solid line) and for the Dougherty operator (red dashed line) for the plateau case (c) and for the beam case (d).

tion almost superpose one on another, once time has been rescaled. A slight discrepancy is recovered for the case of the beam initial condition f_b.

A better agreement between Landau solution and Dougherty solution can be obtained slightly modifying the value of the scaling parameter α (better choices would be $\alpha = 3.35$ for the plateau initial condition and $\alpha = 3.75$ for the beam initial condition), which, however, remains very close to the value $\alpha = 3.55$ predicted from the analytical considerations in the previous section.

2.2.3 Trapped particle distribution function

As a final case, in this section we compare Landau and Dougherty operators in the process of collisional relaxation of a velocity distribution generated by the process of particle trapping. The trapped particle distribution function

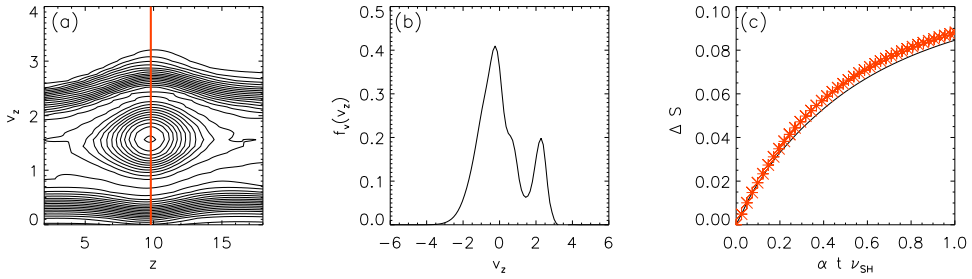

Figure 2.5: (Color online) (a) Phase space portrait of the distribution function obtained through a self-consistent $1D$–$1V$ Vlasov-Poisson simulation at time $t\omega_p = 500$ zoomed in the region $x = [2, 18]$, $v = [0, 4]$. The red vertical line indicates the value of z at which we get the velocity profile $f_v(v_z)$, shown in panel (b). (c) Time evolution of the entropy growth for the Landau operator case (black solid line) and for the Dougherty operator case (red dots).

is obtained by means of a $1D$–$1V$ self-consistent Vlasov-Poisson simulation (with no collisions) with kinetic electrons and fixed protons. In this simulation, the initial plasma is spatially homogeneous, with Maxwellian distribution of velocities. The phase space numerical domain is discretized by 256×101 grid points in physical and velocity space, respectively.

We launch into the plasma an external driver sinusoidal electric field of the form:

$$E_{_D}(z,t) = E_0\ g(t)\sin[k(z - v_\phi t)] \tag{2.19}$$

where $E_0 = 0.2\ \omega_p m v_{th}/e$ (m and e being the electron mass and charge, respectively), $k = 0.26\lambda_D^{-1}$, $v_\phi = 1.42 v_{th}$ and

$$g(t) = \begin{cases} \sin(\pi t/100) & t < 50 \\ 1 & 50 \leq t < 150 \\ \cos[\pi(t-150)/100] & 150 \leq t < 200 \\ 0 & t \geq 200 \end{cases} \tag{2.20}$$

This external field is turned off once a population of trapped particles has been created. Figure 2.5 (a) shows the phase space portrait of the electron distribution function $f_e(z, v_z)$ at a fixed instant of time, after the driver has been turned off. Here, a vortical structure, typical signature of the presence

of trapped particles, is recovered. At this point, we consider the velocity profile $f_v(v_z) = f_e(z_m, v_z)$, where z_m (red vertical line in the plot) is the spatial point corresponding to the maximum velocity width of the trapping region. The velocity profile $f_v(v_z)$ is reported in Fig. 2.5 (b).

Therefore, we build a three-dimensional velocity distribution as follows:

$$f(v_x, v_y, v_z) = C\ f_{_M}(v_x, v_y) f_v(v_z) \tag{2.21}$$

where the constant C is chosen such that $\int f(v_x, v_y, v_z)\ d^3v = n = 1$ and

$$f_{_M}(v_x, v_y) = \exp\left(-\frac{v_x^2 + v_y^2}{2T}\right) \tag{2.22}$$

with

$$U_z = \frac{1}{n}\int v_z f_v(v_z)\ dv_z \tag{2.23}$$

$$T = \frac{1}{n}\int (v_z - U_z)^2 f_v(v_z)\ dv_z \tag{2.24}$$

The three-dimensional velocity distribution $f(v_x, v_y, v_z)$ is used as initial condition for the direct simulations of Eq. (2.4), performed for both the Landau and the Dougherty operator. Figure 2.5 (c) shows the evolution of the entropy for the case of the Landau operator (black line) and of the Dougherty operator (red dots). In this figure, as in previous examples, time has been scaled by $\alpha = 1, 3.55$ for the Landau operator and the Dougherty operator, respectively. Even in this case a slight discrepancy in the evolution of S is recovered, while a better agreement is found when the scaling factor is given the value $\alpha = 3.75$ for the Dougherty simulation.

Finally, in Fig. 2.6 (a)-(d), we directly report the velocity distribution f (evaluated at $v_x = v_y = 0$) versus v_z at four different times in the simulation. The black line in each plot represents the solution obtained when the Landau operator is considered, while the red-dashed line corresponds to the Dougherty solution. Here $\alpha = 1, 3.55$ for the Landau operator and the Dougherty operator, respectively.

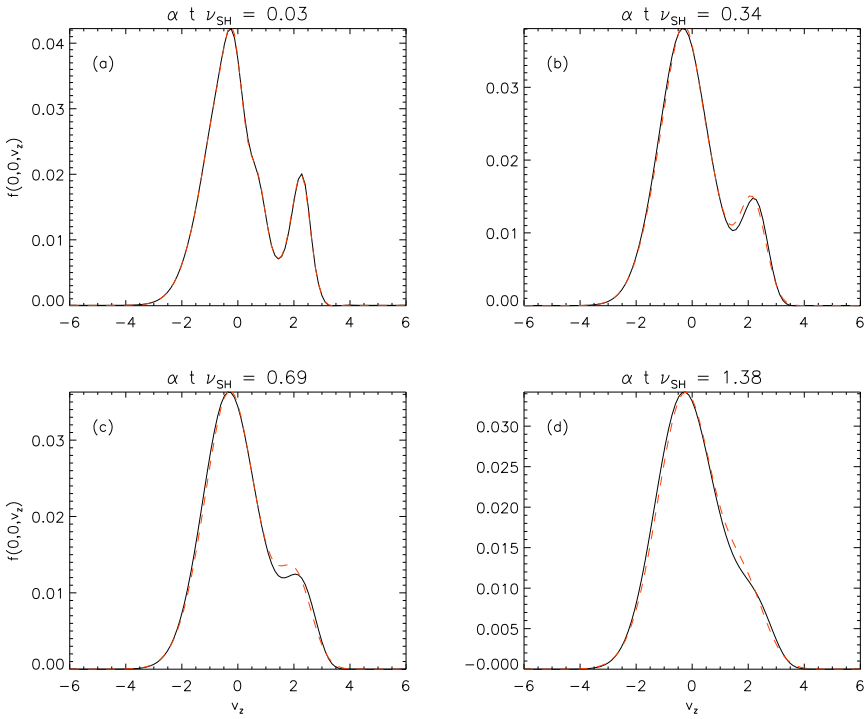

Figure 2.6: (Color online) Velocity distributions obtained from the numerical solution of the Landau equation (black solid line) and of the Dougherty equation (red dashed line) at four different times $\alpha\ t_1\ \nu_{SH} = 0.03$ (a), $\alpha\ t_2\ \nu_{SH} = 0.34$ (b), $\alpha\ t_3\ \nu_{SH} = 0.69$ (c) and $\alpha\ t_4\ \nu_{SH} = 1.38$ (d).

It is worth noting that, during the relaxation process, the form of the velocity distributions display different details. In particular the Dougherty operator seems to be faster than the Landau operator, in smoothing the velocity gradients. This is consistent with the fact that, when slightly increasing more and more the value of the rescaling factor α for the Dougherty simulation, the detailed evolutions of the velocity distributions approach each other more and more. The different behavior of the two operators can be due to the different way they smooth and weight the gradients in velocity space.

To summarize, for all velocity distributions considered in this work, the value of the factor $\alpha = 3.55$ allows to almost superpose the results for the time evolution of $T_\perp$ and $T_\parallel$ obtained in the case of the Landau operator and of the Dougherty operator. For the time evolution of the entropy, the two operators exhibit slight differences, presumably due to the different roles of

the velocity gradients in the Landau and the Dougherty operator. However, we point out that the maximum relative discrepancy for the time evolution of entropy, in a one Spitzer-Harm time, is about 6%. Our results allow to conclude that the lack of physical details that one relentlessly introduces by approximating the Landau operator with the Dougherty operator can be considered negligible compared to the advantage of having a collisional operator, the Dougherty one, that can be easily used and implemented in self-consistent Eulerian simulations and that reproduces satisfactorily the Landau collisional thermalization, once an appropriate time rescaling has been introduced.

2.3 Nonlinear regime of electrostatic waves in presence of electron-electron collisions

In this section, we present the effects of including electron-electron collisions in self-consistent Eulerian simulations of electrostatic wave propagation in nonlinear regime. Based on the considerations of the previous section, electron-electron collisions are modeled through the full three-dimensional Dougherty collisional operator; this allows the elimination of unphysical byproducts due to reduced dimensionality in velocity space. The effects of non-zero collisionality are discussed in the nonlinear regime of the symmetric bump-on-tail instability and in the propagation of KEEN waves. For both cases it is shown how collisions work to destroy the phase-space structures created by particle trapping effects and to damp the wave amplitude, as the system returns to the thermal equilibrium. In particular, for the case of the KEEN waves, once collisions have smoothed out the trapped particle population which sustains the KEEN fluctuations, additional oscillations at the Langmuir frequency are observed on the fundamental electric field spectral component, whose amplitude decays in time at the usual collisionless linear Landau damping rate.

2.3.1 Mathematical and Numerical Approach

We consider a plasma composed by kinetic electrons and motionless protons and analyze the dynamics of this system in electrostatic approximation. As discussed earlier, we model electron-electron collisions through the Dougherty operator [58, 59, 135] and neglect electron-proton and proton-proton collisions, as their characteristic time is significantly longer than that for electron-electron interactions [56, 62, 63].

We consider the following dimensionless Dougherty-Poisson (DP) equations, in $1D$–$3V$ phase space configuration:

$$\frac{\partial f}{\partial t} + v_x \frac{\partial f}{\partial x} + \frac{\partial \phi}{\partial x}\frac{\partial f}{\partial v_x} = \left.\frac{\partial f}{\partial t}\right|_{coll} \tag{2.25}$$

$$- \quad \frac{\partial^2 \phi}{\partial x^2} = 1 - \int f \; d^3v \; ; \tag{2.26}$$

where $f = f(x, \mathbf{v})$ is the electron distribution function, $\phi = \phi(x) = -dE/dx$ is the electrostatic potential (E is the electric field) and $\partial f/\partial t|_{coll}$ is the Dougherty collisional operator. Due to their inertia, the protons are considered as a motionless neutralizing background of constant density $n_0 = 1$. In previous equations, time is scaled to the inverse electron plasma frequency ω_{pe}, velocities to the initial electron thermal speed $v_{th,e}$; consequently, lengths are normalized by the electron Debye length $\lambda_{De} = v_{th,e}/\omega_{pe}$ and the electric field by $\omega_{pe} m v_{th,e}/e$ (m and e being the electron mass and charge, respectively). For the sake of simplicity, from now on, all quantities will be scaled using the characteristic parameters listed above.

The Dougherty collisional operator [58, 59] has the following form:

$$\left.\frac{\partial f}{\partial t}\right|_{coll} = \nu(n,T)\frac{\partial}{\partial v_j}\left[T\frac{\partial f}{\partial v_j} + (v - V)_j \, f\right] \; ; \tag{2.27}$$

here, $\nu(n,T)$ is the collision frequency:

$$\nu(n,T) = \nu_0 \frac{n}{T^{3/2}} \; ; \; \nu_0 = \frac{g \ln \Lambda}{\alpha 8\pi} \; ; \tag{2.28}$$

where $g = 1/n\lambda_{D,e}^3$ is the plasma parameter, $\ln \Lambda \simeq -\ln g/3$ is the Coulom-

bian logarithm, $\alpha = 3.55$ is the scaling factor discussed previously, and the subscript j indicates the j-th vector component. Moreover $n = \int d^3v f$, $V_j = 1/n \int d^3v\ v_j f$, $T = 1/3n \int d^3v\ (\mathbf{v} - \mathbf{V})^2 f$ are respectively plasma density, mean velocity and temperature. These last quantities obviously depend on coordinate x, since $f = f(x, \mathbf{v})$. Einstein notation has been used in Eq. (2.27).

We solve numerically Eqs. (2.25)–(2.26) through a Eulerian code based on a finite difference scheme for the approximation of spatial and velocity derivatives of f over the grid-points [40, 153, 154]. Time evolution of the distribution function is approximated by using the splitting scheme proposed by Filbet et al. [126] (see also Refs. [62, 63] for details about the numerical algorithm). We employ periodic boundary conditions in physical space and f is set equal to zero for $|v_j| > v_{max}$, where $v_{max} = 6v_{th,e}$. Phase space is discretized with $N_x = 128$ grid points in the physical domain $D_x = [0, L]$ and $N_{v_x} \times N_{v_y} \times N_{v_z}$ points in the three-dimensional velocity domain ($N_{v_x} = 101, N_{v_y} = N_{v_z} = 51$). Finally, the time step Δt has been chosen in such a way to satisfy Courant-Friedrichs-Levy condition [150] for the numerical stability of time explicit finite difference schemes.

2.3.2 Numerical Results

We present and discuss the results of kinetic Eulerian simulations in two different physical situations: the linear and nonlinear regime of the bump-on-tail instability and the excitation and propagation of the KEEN waves.

Bump-on-tail instability

In this section, we focus on the process of bump-on-tail instability [155, 156] in a collisional plasma, in order to point out the role of collisions on the onset of the instability and on its nonlinear saturation. The initial electron distribution function considered for the numerical runs has the following form:

$$f(v_x, v_y, v_z, t = 0) = f_0(v_x) f_{_M}(v_y) f_{_M}(v_z) \tag{2.29}$$

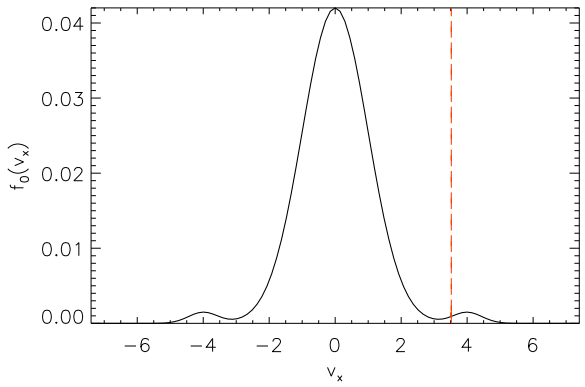

Figure 2.7: (Color online) Velocity dependence of f_0; the vertical red-dashed line indicates the wave phase speed.

where:

$$f_0(v_x) = \frac{n_1}{(2\pi T_1)^{1/2}} \exp\left(-\frac{v_x^2}{2T_1}\right) + \frac{n_2}{(2\pi T_2)^{1/2}} \times \left[\exp\left(-\frac{(v_x - V_0)^2}{2T_2}\right) + \exp\left(-\frac{(v_x + V_0)^2}{2T_2}\right)\right] \tag{2.30}$$

$$f_M(v_j) = \frac{1}{(2\pi T)^{1/2}} \exp\left(-\frac{v_j^2}{2T}\right); \quad j = y, z \tag{2.31}$$

with $n_1 = 0.97$, $n_2 = 0.015$ ($n_0 = n_1 + 2n_2 = 1$), $V_0 = 4.0$, $T_1 = 1.0$ and $T_2 = 0.2$. Moreover, $f_M(v_{j=y,z})$ is a normalized Maxwellian with temperature $T = 1/n \int dv_x (v_x - V_x)^2 f_0(v_x)$. In these conditions, the plasma initially does not present any temperature anisotropy among the three velocity directions. Choosing an initial electron velocity distribution that is symmetric in v_x guarantees an initial state with no net plasma currents or magnetic fields [156].

At t = 0, we perturb the system with a sinusoidal density perturbation of amplitude $A_1 \simeq 5.6 \times 10^{-4}$; we set the length of the spatial domain $L \simeq 22$, in such a way to excite the most unstable wavenumber (the one with the largest growth rate) $k^* = 2\pi/L \simeq 0.28$, whose value has been predicted through a linear Vlasov solver, which computes numerically the roots of the electrostatic dielectric function. This density perturbation produces (through Poisson

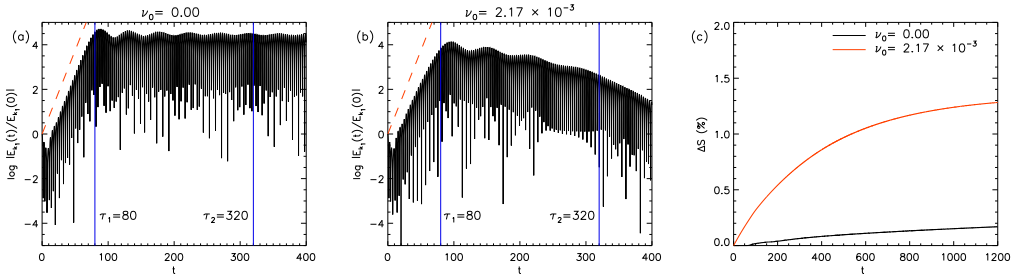

Figure 2.8: (Color online) Time evolution of $\log|E_{k_1}(t)/E_{k_1}(0)|$, for $\nu_0 = 0.0$ (a) and $\nu_0 = 2.17 \times 10^{-3}$ (b); here, the red-dashed curves represent the theoretical prediction for the instability growth rate $\gamma_I^{th} \simeq 7.46 \times 10^{-2}$. In panel (c), the time evolution of the entropy variation ΔS (in %) is reported for $\nu_0 = 0.0$ (black-solid curve) and $\nu_0 = 2.17 \times 10^{-3}$ (red-solid curve).

equation) an initial sinusoidal electric field of amplitude $E_1 \simeq 2 \times 10^{-3}$. Figure 2.7 shows f_0 as a function of v_x; here, the vertical red-dashed line represents the value of the wave phase speed v_ϕ, which clearly falls in the unstable region where $df_0/dv_x|_{v_\phi} > 0$.

Figure 2.8 (a) displays the time evolution of the logarithm of the fundamental electric field spectral component E_{k_1} (where $k_1 = k^*$), normalized to its initial value ($\log|E_{k_1}(t)/E_{k_1}(0)|$), for a collisionless simulation. In the early stage of the system evolution, a linear exponential growth of the wave amplitude is observed with growth rate $\gamma_I^{obs} = 7.29 \times 10^{-2}$; this value is in good agreement with the theoretical expectation obtained through a numerical linear Vlasov solver $\gamma_I^{th} = 7.46 \times 10^{-2}$ (red-dashed line). Later in time, nonlinear effects come into play and arrest the exponential growth; in this regime, the wave amplitude displays nearly periodic oscillations around an almost constant saturation level. These oscillations are driven by particle trapping processes [157, 158] and typical vortical structures are generated in the longitudinal $(x - v_x)$ phase space, in the velocity range around v_ϕ.

When collisions are taken into account, the system evolution can change significantly. In Figure 2.8 (b), we show a collisional simulation with $\nu_0 \simeq 2.17 \times 10^{-3}$. For such value of the collision frequency, the linear growth of the wave amplitude remains close to exponential with a growth rate somewhat less than that for the collisionless case. This suggests that, in this

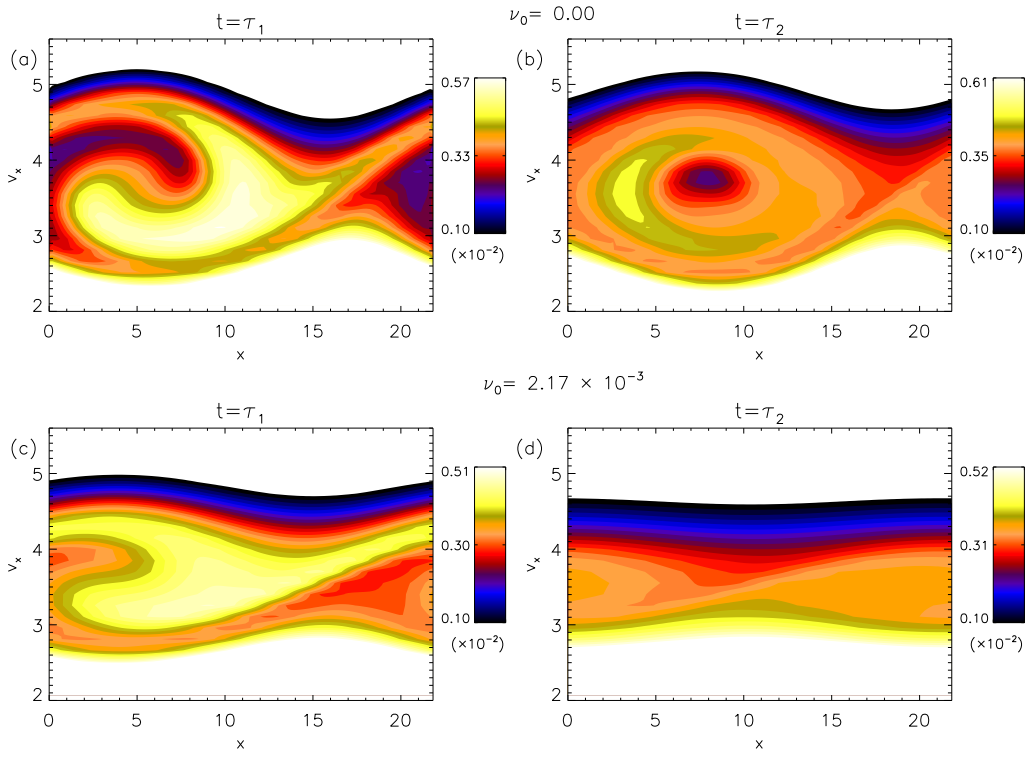

Figure 2.9: $x - v_x$ contour plot of the electron distribution function (zoomed in the velocity range $\simeq v_\phi$), evaluated at $v_y = v_z = 0$, for $\nu_0 = 0.0$ (top row) and $\nu = 2.17 \times 10^{-3}$ (bottom row), at the time instants $t = \tau_1 = 80$ (left column) and $t = \tau_2 = 320$ (right column).

scenario, the damping rate due to collisions is lower than the growth rate of the instability, thus showing that collisions are too weak to prevent the instability onset. However, the nonlinear saturation of the instability is evidently affected by collisions. In fact, from Figure 2.8 (b), one notices that the saturation amplitude is decreased with respect to the collisionless case and that the electric oscillations are significantly damped after the saturation of the instability, as collisions work to smooth out the trapping structure and to drive the particle distribution towards the equilibrium Maxwellian shape. Additional runs with larger values of ν_0 (not presented here) show how also the linear phase of the system evolution is modified in the strong collisional regime and eventually the onset of the instability is completely prevented.

We evaluated also from the simulations the entropy $S = -\int f \ln f \; dx \; dv$.

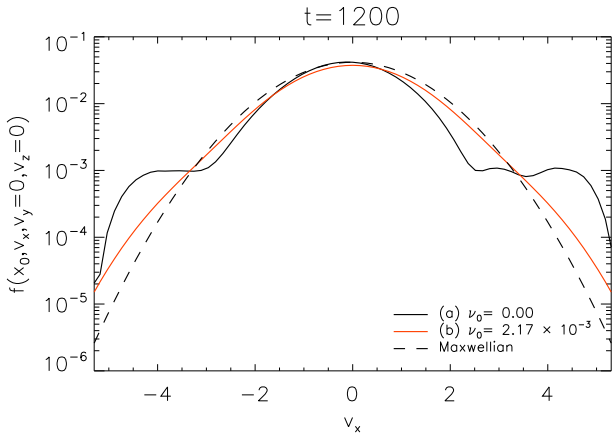

Figure 2.10: (Color online) Semi-logarithmic plot of $f(x_0, v_x, v_y = 0, v_z = 0)$ as a function of v_x at the time instant $t = 1200$, for $\nu_0 = 0.0$ (black-solid line) and $\nu_0 = 2.17\times10^{-3}$ (red-solid line); the black-dashed curve indicates the corresponding Maxwellian.

In Fig. 2.8 (c) we compare the entropy growth,defined as $\Delta S = [S(t) - S(t = 0)]/S(t = 0)$, for the collisionless case (black solid line) and for the weekly collisional case with $\nu_0 = 2.17 \times 10^{-3}$ (red solid line). Since the collisionless Vlasov system is an iso-entropic system, the small entropy growth ($\simeq 0.15\%$) recovered in the collisionless simulation is obviously due to numerical effects (filamentation). On the other hand, in the collisional case, the increase in entropy (about 10 times larger than the unphysical entropy growth for the collisionless simulation) is mainly due to the effect of collisions which drive the system towards thermal equilibrium, according to H theorem.

To conclude this Section, in Fig. 2.9 we show the $x - v_x$ contour plots (zoomed in the velocity range $\simeq v_\phi$) of the distribution function evaluated at $v_y = v_z = 0$; the top/bottom row in this figure corresponds to the collisionless/collisional case. We plot the distribution function at two instants of time in the simulations ($\tau_1 = 80$ and $\tau_2 = 320$), indicated by the vertical solid-blue lines in Figs. 2.8 (a)–(b); τ_1 corresponds to the end of the exponential growth phase of the wave amplitude, while τ_2 is picked in the nonlinear regime of wave propagation. In the top row of Fig. 2.9 (collisionless case), one recognizes (left panel) the vortical phase-space structure at $v_x \simeq v_\phi \simeq 3.5$, typical signature of particle trapping, which is persistent

in time (right panel). A similar phase-space vortex (not shown here) is recovered at $v_x \simeq -3.5$; the two counter-propagating phase space trapping populations are associated with the standing plasma wave launched by the initial density perturbation and amplified by the bump-on-tail instability. In the bottom row of the same figure (collisional case), at $t = \tau_1$ [Fig. 2.9 (c)], the vortex has a smaller velocity width as compared to the collisionless simulation; moreover, collisions prevent the generation of fine velocity scales and, at $t = \tau_2$ [Fig. 2.9 (d)], the trapping structure has been almost completely smoothed out.

Figure 2.10 shows, in a semi-logarithmic plot, the dependence of the distribution function on v_x (evaluated at a fixed spatial position x_0, and at $v_y = v_z = 0$) at the time instant $t = 1200$, for the collisional simulation (red-solid line) and the collisionless one (black-solid line). The point x_0 corresponds to the spatial position where the phase space vortex moving with positive velocity has its maximum velocity width. In the collisional case, thermal equilibrium has been almost restored by collisions, while, in absence of collisions, the distribution function still displays many strong deviations from the Maxwellian profile (represented by the black-dashed curve). We point out that the asymmetry of the velocity profile for the collisionless simulation in Fig. 4 (black-solid line) is due to the fact that at $t = 1200$ the two counter-propagating phase space trapping vortices are not exactly aligned in phase space (i. e. their centers are not in the same spatial location).

Kinetic electrostatic electron nonlinear waves

For the simulations of KEEN wave excitation [138, 137], we refer to a previous work by Cheng et al. [159]. According to these authors, the box length for this simulation is set $L = 24.166$. At $t = 0$ the plasma is spatially homogeneous with density $n_0 = 1$ and isotropic Maxwellian in velocities with temperature $T = 1$. In order to produce the excitation of KEEN waves, we drive the plasma through an external electric field of the form [137]:

$$E_{_D}(x,t) = E_0 \; g(t) \sin[k_0(x - v_\phi t)] \; , \tag{2.32}$$

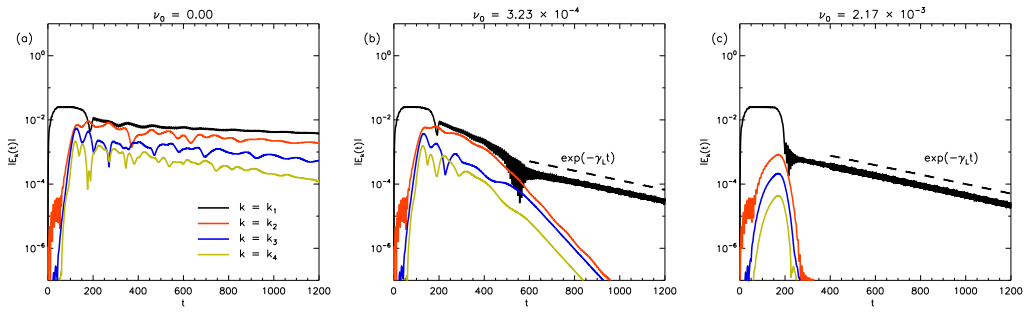

Figure 2.11: (Color online) Time evolution of the first four electric field spectral components for the simulations with $\nu_0 = 0.0$ (a), $\nu_0 = 3.23 \times 10^{-4}$ (b) and $\nu_0 = 2.17 \times 10^{-3}$ (c). The black-dashed curves in panels (b) and (c) indicate the theoretical Landau prediction $\gamma_L \simeq 3.40 \times 10^{-3}$ for Langmuir wave damping rate.

where E_0 is the maximum driver amplitude, $k_0 = 2\pi/L = 0.26$ is the fundamental wavenumber, $v_\phi = 1.42$ and

$$g(t) = \begin{cases} \sin(\pi t/100) & t < 50 \\ 1 & 50 \leq t < 150 \\ \cos[\pi(t-150)/100] & 150 \leq t < 200 \\ 0 & t \geq 200 \end{cases} . \tag{2.33}$$

The external field is turned off after a time at which past experience indicates that optimal trapping of particles is achieved (i.e., an appropriate ratio of an electron trapping period for the external drive). We performed different simulations by varying the value of the plasma parameter g, and consequently of ν_0 ($\nu_0 = 0.00, 3.23 \times 10^{-4}, 2.17 \times 10^{-3}$), keeping fixed $E_0 = 0.05$.

Figure 2.11 shows the evolution of the first four electric field spectral components (with wavenumbers $k_1 = k_0$, $k_2 = 2k_0$, $k_3 = 3k_0$ and $k_4 = 4k_0$), for $\nu_0 = 0.00$ (a), $\nu_0 = 3.23 \times 10^{-4}$ (b) and $\nu_0 = 2.17 \times 10^{-3}$ (c) respectively.

In the collisionless case [Fig. 2.11 (a)], we recover one of the typical features of the KEEN waves [137, 138, 159]. While the driver is turned on, the energy injected into the fundamental wavenumber component (black line) flows also to the higher spectral components (red, blue and yellow solid lines). After the driver has been turned off, the resulting electric signal is composed

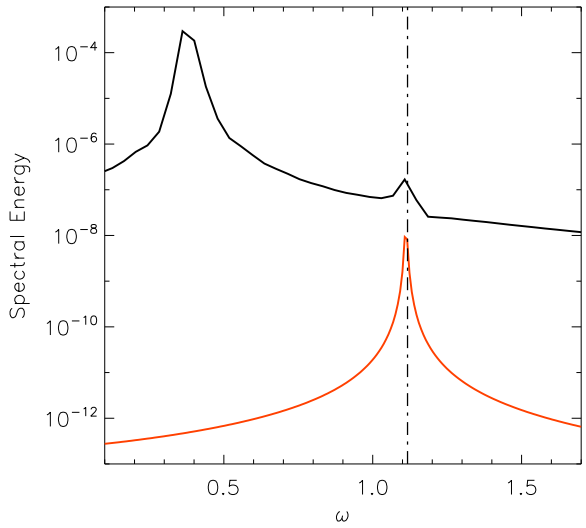

Figure 2.12: (Color online) Spectral energy of the fundamental electric field component as a function of frequency, for the stronger collisional case with $\nu_0 = 2.17 \times 10^{-3}$, computed in the time intervals $0 \leq t \leq 180$ (black curve), and $400 \leq t \leq 1200$ (red curve). The vertical clack-dashed curve indicates the value of the Langmuir frequency of the fundamental wavenumber.

by many wavenumbers, in a stable ratio one with another, thus departing significantly from the purely sinusoidal spatial shape of the driver field.

Figures 2.11 (b)-(c) display the time evolution of the electric field spectral components in two different collisional plasmas, for $\nu_0 = 3.23 \times 10^{-4}$ and $\nu_0 = 2.17 \times 10^{-3}$, respectively.

Beginning with the behavior while under the drive, on comparing the behavior to that without collisions, the behavior seems quite straightforward. For the weakly collisional case of Fig. 2.11 (b), in the initial phase of the system evolution (i.e., up to $t = 200$), when the external driver is on, the excitation of the spectral components does not seem to be significantly affected by collisions i.e., the early parts of Figs. 2.11 (a) and 2.11 (b) look much alike. On the other hand the response of Fig. 2.11 (c) with strong collisions is much weaker.

Turning now to the behavior after the drive has stopped, a significant difference between the damping is apparent between the cases where the

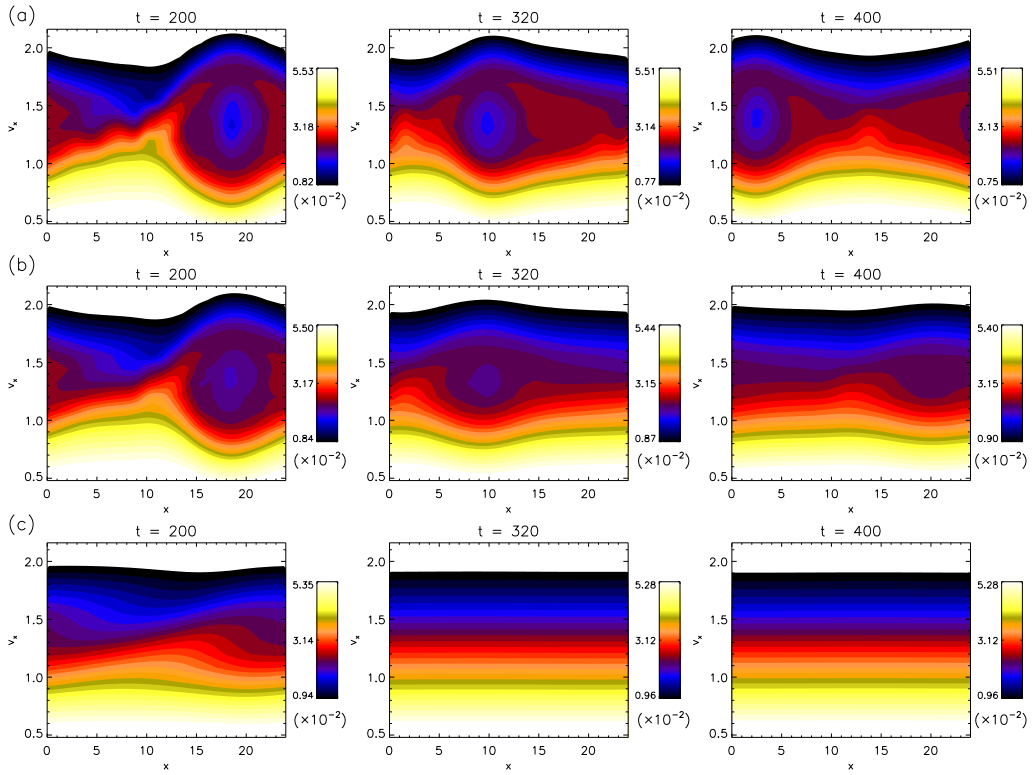

Figure 2.13: $x - v_x$ contour plot of the electron distribution function (zoomed in the velocity range $\simeq v_\phi$), evaluated at $v_y = v_z = 0$, for simulations with $\nu_0 = 0.0, 3.23 \times 10^{-4}, 2.17 \times 10^{-3}$ (top, middle and bottom row, respectively) and at different times $t = 200, 320, 400$ (left, middle and right column, respectively).

damping is zero (Fig. 2.11 (a)), moderate (Fig. 2.11 (b)), and strong (Fig. 2.11 (c)). At the extremes, the collisionless KEEN behavior of Fig. 2.11 (a) with its strongly persistent harmonics is in striking contrast to the highly collisional case of Fig. 2.11 (c) where the fundamental is the only component which survives in the long time limit. For intermediate collision frequency ($\nu_0 = 3.23 \times 10^{-4}$) case of Fig. 2.11 (b), in the time interval $200 \leq t \leq 550$, the higher harmonic electric field components decrease somewhat faster than the fundamental (as one might expect) at roughly constant rates, but then there occurs a fairly sudden and remarkable transition (for $500 \leq t \leq 600$) to a much lower decay rate for the fundamental and an increased decay rate for the higher (2, 3, 4) harmonics. Thus at late times only the fundamental component survives.

These late-time fundamental decay rates recovered for the two collisional cases (Figs. 2.11 (b) and 2.11 (c)) seem almost independent of the collision frequency. Through a careful analysis of the time signals, we realized that the oscillations on the fundamental wavenumber, observed for $t > 600$ in Fig. 2.11 (b) and for $t > 200$ in Fig. 2.11 (c), occur at the Langmuir frequency, which is larger than the frequency of the KEEN waves excited by the driver. The dashed curves in Figs. 2.11 (b)-(c) represent the prediction for collisionless Landau damping rate [160], which fits clearly well the numerical results, for both the intermediate and strong collisional cases. In order to understand the origin of these Langmuir fluctuations, we performed the Fourier analysis of the electric signal, in the time interval in which the driver is still on; this analysis revealed that the Langmuir frequency has been driven by the driver itself, which pumps energy at the KEEN frequency, with an additional small amount of energy at the Langmuir frequency on the fundamental. The excitation of this additional Langmuir oscillation by the driver is due to the fact that the external electric field is turned on and off quite abruptly (with sharp time gradient in its amplitude). These abrupt kicks on the plasma excite Langmuir fluctuations, since they are proper modes of the system. Presumably, a smoother ramping up and down of the driver field (see Ref. [143]) would have eliminated this additional Langmuir oscillation, but it would have required a significantly longer time for the driving process.

To substantiate the conclusions above, in Fig. 2.12, we report the spectral energy of the fundamental component as a function of frequency, for the stronger collisional case with $\nu_0 = 2.17 \times 10^{-3}$, computed in the time intervals $0 \leq t \leq 180$ (black curve), in which the driver is still on, and $400 \leq t \leq 1200$ (red curve), in which the driver is off. As it can be seen in this figure, when the driver is on, the main KEEN frequency peak is observed together with a low energy peak at the Langmuir frequency (vertical dot-dashed black line in the figure); on the other hand, when the driver is off, the KEEN fluctuations are killed by collisions and only the Langmuir peak is visible. Finally, the fact that these Langmuir oscillations decay at the collisionless Landau damping rate suggests that collisions, which strongly affect the evolution of the KEEN fluctuations, are negligible at higher Langmuir phase speeds, where

the particle velocity distribution remains close to a Maxwellian during the simulation.

To conclude this Section, in Fig. 2.13 we show the contour plots of the electron distribution function (evaluated at $v_y = v_z = 0$) in the longitudinal $(x - v_x)$ phase space, for simulations with $\nu_0 = 0.0, 3.23 \times 10^{-4}, 2.17 \times 10^{-3}$ (top, middle and bottom row, respectively) and at different times $t = 200, 320, 400$ (left, middle and right column, respectively). These contour plots clearly show how the phase space trapping structure, which is persistent in the collisionless simulation and sustain the KEEN fluctuations, is smoothed out by collisions as fast as ν_0 increases.

2.4 Summary

To summarize the results presented above, we performed a detailed comparison between the Landau operator [52] and the Dougherty operator [58] by means of Eulerian kinetic simulations of a homogeneous, field-free plasma in a three-dimensional velocity space.

As a first step, by looking at the collisional relaxation processes of a bi-Maxwellian velocity distribution, we have realized that an "ad hoc" time rescaling procedure allows to make the time evolution of parallel and perpendicular temperatures described by the Dougherty operator in Eqs. (2.12)–(2.13) very close to the one obtained when the full Landau integral is employed [Eqs. (2.8)−(2.9)], despite the profound mathematical differences between the two operators. Pushed by these surprising analytical findings, we employed an Eulerian algorithm to simulate numerically the return toward equilibrium of several velocity distributions (bi-Maxwellian, beam distribution, plateau distribution etc.), for which we verified that the Dougherty-Landau time rescaling factor α is the same and does not change with respect to the analytical prediction obtained for the bi-Maxwellian case.

We would like to point out that, since the Dougherty operator does not describe the velocity dependence of the diffusion coefficients in velocity space, we cannot assure that the time-scaling factor we determined does not change in situations where the distribution function is extremely distorted with re-

spect to a Maxwellian one. Therefore, the detailed comparison between Landau and Dougherty collisional operators in full self-consistent simulations will be the subject of future works. However, since the two collisional operators behave in a very similar way for about one Spitzer-Harm time, the Dougherty operator can be employed in a wide range of kinetic simulations to replace the much more complex and computationally demanding Landau operator.

One of these kind of collisional self-consistent simulations have been described in Sect. 2.3, where the propagation of nonlinear electrostatic waves in a weakly collisional plasmas has been analyzed. Electron-electron collisions have been modeled through the Dougherty collisional operator for electron-electron collisions, in full three-dimensional geometry in velocity space. We described numerically the onset and nonlinear saturation of the bump-on-tail instability [155, 156] (in its symmetric form) and the excitation and propagation of the so-called Kinetic Electrostatic Electron Nonlinear waves [137, 138, 159], in situations of intermediate range of plasma collisionality. In this way, we get rid of the restrictive collision-free assumption, keeping, however, the system dynamics far from the strong collisional fluid regime, where the plasma always remains at thermodynamic equilibrium. In other words, the physical regime of interest here is the one where kinetic effects, which tend to drive the system far from the thermodynamic equilibrium, and collisions, which tend to restore the Maxwellian configuration, compete and combine themselves, shaping the particle distribution function in a complex way.

For the case of the symmetric bump-on-tail instability, we noticed that the onset of the instability (and the exponential growth of the wave amplitude) is almost unaffected, for the value of collision frequency chosen in our simulations. On the other hand, the nonlinear saturation phase, in which the fluctuations are maintained at almost constant amplitude thanks to the phase-space deformation of f, is dramatically modified by collisions, which work to smooth out any departure of f from Maxwellian and damp the wave amplitude.

Concerning the simulations of the KEEN waves, we found that, in presence of collisions, the trapping phase space structure created by the driver

field is smoothed out. As a consequence, the KEEN fluctuations are dissipated in time. In the case of intermediate collisionality, the fundamental spectral component and its harmonics (we have shown the first four) survive for a while after the driver is turned off. We noticed that in the long time limit the fundamental component displays a residual energy at the Langmuir frequency and its amplitude decays in time at a rate in good agreement with the collisionless damping rate predicted by Landau in Ref. [160]. As explained previously, this Langmuir fluctuation has been triggered by the external field during the driving process. In the case of stronger collisionality, again fluctuations on the fundamental component appear at the Langmuir frequency in the long time limit, while the higher spectral components at the KEEN frequency are now very rapidly smoothed out by collisions, right after the driver has been turned off. The fact that the late-time decay rate of the fundamental is independent of the collision frequency, being in agreement with the collisionless Landau damping rate, suggests that the wave dissipation due to collisions is less efficient than the Landau damping process at high Langmuir phase speeds, where the particle velocity distribution remains close to a Maxwellian. On the other hand, the presence of (even weak) collisions is critical for the survival of the KEEN fluctuations, since the smoothing of the particle velocity distribution induced by collisions prevent the existence of the KEEN mode itself.

Chapter 3

Collisional effects described in a reduced phase space

So far, collisions have been modeled in the realistic three-dimensional velocity space. However, in this framework, high-resolution numerical simulations cannot be performed for computational reasons. Therefore, another class of collisional operators, which assume a reduced phase space dimensionality, has been introduced. Since collisions naturally work in a three-dimensional velocity space, this assumption is not appropriate from a basic point of view. However, when collisions act on longitudinal electrostatic waves and the system dynamics occurs preferentially in a unique direction, one can quite well describe collisional effects in a reduced one-dimensional velocity space.

Here we restrict to such $1D$–$1V$ phase space and we analyze two different problems: the effects of collisions on the problem of numerical recurrence [Sect. 3.1] and the description of the waves launching process in column of plasma in both collisionless and weakly collisional cases [Sec. 3.2].

Results shown here have been collected in one scientific paper published in *Physics of Plasma* [161], which has been selected as Featured Article in the February 2016 Issue of Physics of Plasmas, while a second paper is still in preparation [162].

3.1 Collisional effects on the numerical recurrence

When the Vlasov-Poisson equations are studied by means of Eulerian numerical simulations, one encounters, for low amplitude fluctuations, the problem of the initial state recurrence. As explained by Cheng et al. [163], the recurrence phenomenon is intimately related to the presence of a free-streaming term in the distribution function and to the filamentation problem [159, 163, 164, 165, 166, 167, 168]. Since the mesh-size of the velocity grid is necessarily finite, the initial state is periodically re-constructed, and thus the electric field exhibits a fake recurrence of the initial state, whose period is $T_{rec} = 2\pi/k\Delta v$, k being the perturbation wavenumber and Δv the numerical grid mesh in velocity space.

In this section, the effects of collisions on the phenomenon of the numerical recurrence are discussed. Collisions are modeled through the Lenard-Bernstein (LB) operator, firstly proposed in 1958 by Lenard and Bernstein [139] as a full three-dimensional velocity space collisional operator. The LB operator is a linear Fokker-Planck collisional operator which belongs, as the Dougherty one [58, 59], to the class of "simplified" collisional operators and both collisional terms can be interpreted as advection-diffusion operators in the velocity space.

Interestingly, the same effect on the spectrum induced by LB collisions has been discussed in Ref. [169] in the context of *spectral deformation*. This is a technique introduced for the Vlasov-Poisson system in [170], where a non-unitary transformation is applied to the linear operator, in such a way that its eigenvalues with nonzero real part remain unchanged, while the continuum of neutral modes is damped. In analogy to the case of LB operator, the Landau damping is recovered as a true eigenmode. Therefore, we suggest that the LB operator might be interpreted as a spectral deformation to the collisionless Vlasov-Poisson system. However, the precise identification of the transformation which is equivalent to the LB operator is left for future work.

The aim of our analysis is to understand if recursive effects or any other

numerical effect associated to limited velocity resolution of Eulerian calculations can be successfully removed by making use of a collisional operator, without increasing the number of gridpoints in the velocity domain (and without altering the physical features of the system evolution). In case of positive response, this would be extremely useful especially for multi-dimensional simulations, where the velocity resolution is limited for computational reasons. We show that, in general, the collision frequency ν which is suitable for preventing recurrence in the linear regime is a function of the perturbation wavenumber: as the wavenumber increases a stronger collisionality is necessary to avoid the onset of the numerical recurrence. Moreover, by focusing on the nonlinear Landau damping and in particular on the formation of a Bernstein-Greene-Kruskal (BGK) nonlinear wave [146, 157], we show that i) the collisionless case is also slightly affected by recurrence and ii) collisional effects become important when the dynamics evolve to the nonlinear stage.

Therefore, it seems impossible to use the LB operator to avoid the numerical recurrence and, simultaneously, preserve the phase space structures developed as in the collisionless case. Of course, in the case of higher velocity resolution, for which the recurrence time is significantly larger than the characteristic time of the physical process of interest (Landau damping, onset of instabilities, generation of nonlinear BGK structures and so on), the use of a collisional operator opportunely tailored to eliminate numerical recurrence does not affect the reliability of the physical results for times smaller than the recurrence time. However, let us remark that this case is not the one of interest in our analysis in which we intentionally choose to have recurrence in the initial stage of the simulations, which typically cannot afford a very fine resolution in velocity space (especially in multi-dimensions). Finally, by exploring the recurrence effect on the bump-on-tail instability [156], we show that the recurrence affects both the linear exponential growth and the nonlinear saturation of the instability by producing a fake growth in the electric field and that, as in the nonlinear Landau damping case, collisional effects are not able to prevent the initial state recurrence without significantly altering the nonlinear structures.

In summary, the purpose of this section is twofold. First, we show how

recursive effect and filamentation, which are usually described in the context of low amplitude fluctuations, can also be problematic in nonlinear phenomena, such as the saturation regime of the bump-on-tail instability. Second, we discuss a useful diagnostic, in terms of expansion of the velocity space into Hermite functions, that allows to better appreciate the effect of an artificial collisional operator in phase space.

Let us summarize the content of the section. In Sec. 3.1.1 the theoretical background of the problem is given and the numerical strategies adopted to approach the solution are explained. Then, in Sec. 3.1.2, the recurrence effects on the Landau damping phenomenon are described in both linear and nonlinear regimes by transforming the Vlasov-Poisson system into Hermite-Fourier coordinates and by means of Eulerian simulations. Moreover, we investigate how collisional effects prevent the recurrence problem but, at the same time, smooth out the nonlinear plasma dynamics features as the system evolves to the nonlinear regime. Then, in Sec. 3.1.3 we analyze the initial state recurrence problem and the collisional effects for the case of the bump-on-tail instability.

3.1.1 Theoretical background and numerical models

Here we consider a quasi-neutral and unmagnetized plasma composed by kinetic electrons and immobile background ions. We assume that only electrostatic interactions occur between particles, therefore the Maxwell system reduces to the Poisson equation. Furthermore, since electron-ion and ion-ion collision frequencies are much smaller than the electron-electron one, we take into account only electron-electron collisions [56]. As introduced above, electron-electron collisions are modeled through the LB collisional operator [139].

The normalized collisional Vlasov-Poisson (VP) equations - where collisions are modeled through the LB collisional operator - in the $1D$–$1V$ (one dimension in physical space and one dimension in velocity space) phase space

configuration reads:

$$\frac{\partial f}{\partial t} + v\frac{\partial f}{\partial x} + \frac{\partial \phi}{\partial x}\frac{\partial f}{\partial v} = \left.\frac{\partial f}{\partial t}\right|_{coll} \tag{3.1}$$

$$- \quad \frac{\partial^2 \phi}{\partial x^2} = 1 - \int f \; dv \; ; \tag{3.2}$$

where $f = f(x, v)$ is the electron distribution function, $\phi(x)$ is the electrostatic potential, defined as $E = -d\phi/dx$ (E is the electric field) and $\partial f/\partial t|_{coll}$ is the LB collisional operator. Due to their inertia, the protons are considered as a motionless neutralizing background of constant density $n_0 = 1$. In previous equations, time is scaled to the inverse electron plasma frequency ω_{pe}, velocities to the initial electron thermal speed $v_{th,e}$; consequently, lengths are normalized by the electron Debye length $\lambda_{De} = v_{th,e}/\omega_{pe}$ and the electric field by $\omega_{pe} m v_{th,e}/e$ (m and e being the electron mass and charge, respectively). For the sake of simplicity, from now on, all quantities will be scaled using the characteristic parameters listed above.

The scaled Lenard-Bernstein [139] collision operator is:

$$\left.\frac{\partial f}{\partial t}\right|_{coll} = \nu \frac{\partial}{\partial v}\left[\frac{\partial f}{\partial v} + v f\right] \tag{3.3}$$

being ν the constant collisional frequency. The LB operator preserves global mass. Moreover, if the distribution function has null average speed $V = 0$ and unitary temperature $T = 1$, being $V = 1/n \int dv f v$, $n = \int dv f$ and $T = 1/n \int dv (v - V)^2 f$ respectively plasma mean velocity, density and temperature, it conserves also momentum and energy.

In the following we analyze the equations system Eqs. (3.1)–(3.2) coupled to Eq. (3.3). For the sake of simplicity, we refer to this system compactly as Eqs. (3.1)–(3.2). Two different analyses have been performed on Eqs. (3.1)–(3.2) and are briefly explained in the following two subsections.

Fourier-Hermite decomposition (Linear analysis)

A very convenient way of studying the properties of the LB operator in the linear regime is by employing an expansion of the linearized distribution func-

tion into a Fourier-Hermite basis. Here, we use the so-called asymmetrically weighted Hermite functions [42, 44, 171]:

$$\Psi_n(\xi) = (\pi 2^n n!)^{-1/2} H_n(\xi) e^{-\xi^2} \tag{3.4}$$

$$\Psi^n(\xi) = (2^n n!)^{-1/2} H_n(\xi), \tag{3.5}$$

where H_n is the n-th Hermite polynomial, defined as

$$H_n(\xi) = (-1)^n e^{\xi^2} \frac{d^n}{d\xi^n} \left(e^{-\xi^2} \right), \tag{3.6}$$

and $\xi = v/\sqrt{2}$. The basis in Eqs. (3.4)–(3.5) has the following properties:

$$\int_{-\infty}^{\infty} \Psi_n(\xi) \Psi^m(\xi) d\xi = \delta_{n,m}, \tag{3.7}$$

$$v\Psi_n(\xi) = \sqrt{n+1}\Psi_{n+1}(\xi) + \sqrt{n}\Psi_{n-1}, \tag{3.8}$$

$$\frac{d\Psi_n(\xi)}{dv} = -\sqrt{(n+1)}\Psi_{n+1}(\xi), \tag{3.9}$$

$\delta_{n,m}$ being the Kronecker delta. Eqs. (3.1)–(3.2) are linearized around an homogeneous equilibrium that, when expanded in Hermite functions, reads $f_0(v) = \sum_{n=0} C_n^{eq} \Psi_n(\xi)$. Note that, for a Maxwellian equilibrium with zero mean velocity, all coefficients C_n^{eq} are null for $n > 0$. The perturbed distribution function $f_1(x, v) = f(x, v) - f_0(v)$ is expanded as:

$$f_1(x, v) = \sum_{n,j} C_{n,j} \Psi_n \left(\frac{v}{\sqrt{2}} \right) e^{\mathrm{i}k_j x}, \tag{3.10}$$

with $k_j = 2\pi j/L$, and L the domain length. By using the orthogonality of the Fourier-Hermite basis, one obtains, for each k_j mode:

$$\frac{dC_{n,j}}{dt} + \mathrm{i}k_j \left(\sqrt{n+1} C_{n+1,j} + \sqrt{n} C_{n-1,j} + \frac{\sqrt{2n}}{k_j^2} C_{0,j} C_{n-1}^{eq} \right) + n\nu C_{n,j} = 0 \tag{3.11}$$

Note that $\Psi_n(\xi)$ is an eigenfunction of the LB operator of Eq. (3.3), with eigenvalue $n\nu$, and thus the use of the rescaling factor in the argument of

the basis in Eqs. (3.4)–(3.5) allows to obtain a rather compact formulation (compare, for instance, with the formulation in [172]). In particular, the linear equation (3.11) can be written in matrix form as:

$$\frac{d\overrightarrow{C_j}}{dt} = \mathbf{A}_j \overrightarrow{C_j}, \tag{3.12}$$

where $\overrightarrow{C_j}$ is the vector defined as $(C_{0,j}, C_{1,j}, C_{2,j}, \ldots)^T$, and the matrix $\mathbf{A}_j$ is defined as

$$\mathbf{A}_j = -\mathrm{i}k_j \begin{pmatrix} 0 & 1 & 0 & & & \\ 1+\sqrt{2}C_0^{eq}/k_j^2 & \nu/\mathrm{i}k_j & \sqrt{2} & 0 & & \\ 2C_1^{eq}/k_j^2 & \sqrt{2} & 2\nu/\mathrm{i}k_j & \sqrt{3} & 0 & \\ \sqrt{6}C_2^{eq}/k_j^2 & 0 & \sqrt{3} & 3\nu/\mathrm{i}k_j & \sqrt{4} & \ddots \\ \ddots & \ddots & \ddots & \ddots & \ddots & \ddots \end{pmatrix} \tag{3.13}$$

The collisionality ν affects only the diagonal entries of the matrix. Once again, this is due to the fact that the Hermite basis is an eigenfunction of the LB operator. Of course, when numerically solving the linear problem in Eq. (3.12), one has to truncate the matrix $\mathbf{A}$, that is, one has to choose the maximum number N_H of Hermite modes in the expansion of Eq. (3.10), by setting $C_{n,j} = 0$ for any $n > N_H$ (other closures have been investigated, see, e.g. [173, 174]). This corresponds to defining the resolution in velocity space. It is precisely the inability to capture increasingly finer scales in velocity space that gives rise to the phenomenon of recurrence in the numerical solutions of Vlasov equation. This becomes particularly clear by looking at the recurrence effect within the framework of the Hermite basis expansion in velocity.

Eulerian Vlasov code (nonlinear analysis)

The other approach consists in the numerical solution of Eqs. (3.1)–(3.2) through a Eulerian code based on a finite difference scheme for the approximation of spatial and velocity derivatives of f over the grid-points. Time evolution of the distribution function is approximated through the splitting scheme first introduced by Filbet et al. [126] [see Refs. [62, 63] for details

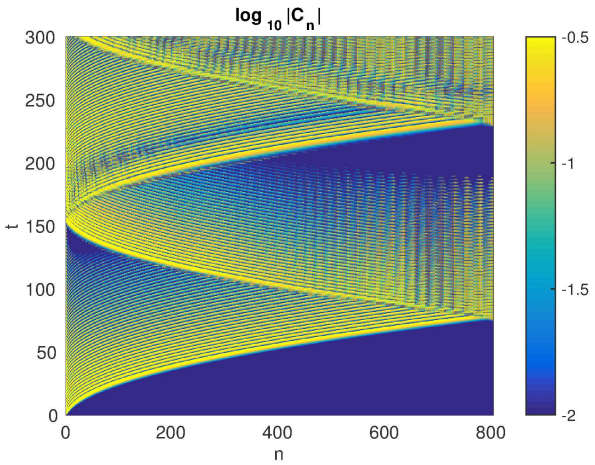

Figure 3.1: (Color online) Temporal evolution of the Hermite coefficients $|C_n|$ (in logarithm scale) as a function of the Hermite mode n and the time t for the collisionless $\nu = 0$ case.

about the numerical algorithm], which is a generalization of the well-known splitting scheme discussed by [163]. We impose periodic boundary conditions in physical space and f is set equal to zero for $|v| > v_{max}$, where $v_{max} = 6v_{th,e}$. Phase space is discretized with N_x grid points in the physical domain and N_v points in the velocity domain. Finally, the time step Δt has been chosen in such a way to respect the Courant-Friedrichs-Levy condition [150] for the numerical stability of time explicit finite difference schemes.

The plasma is initially in an equilibrium state and we perturb the system through an oscillating density perturbation which produces, through the Poisson equation, a perturbative electric field of amplitude δE.

3.1.2 Landau damping

In the present section, recurrence effects and collisional effects on this phenomenon are described for the the case of the Landau damping of a Langmuir wave.

First, we study a collisionless ($\nu = 0$) linear Landau damping case, for the wavenumber $k = k_1 = 2\pi/L = 0.35$ (being $L = 18$), by means of the Fourier-Hermite decomposition with $N_H = 800$. The system is initially perturbed through a spatially sinusoidal electric field perturbation, which translates,

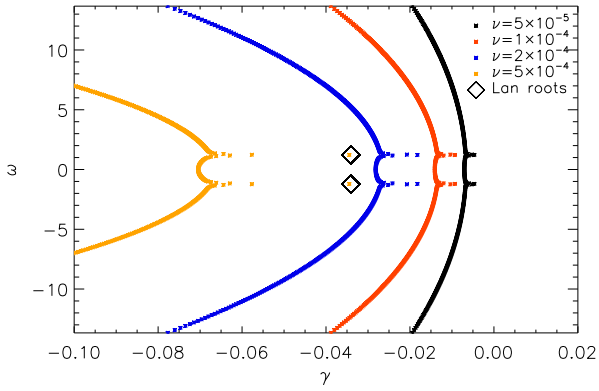

Figure 3.2: (Color online) Spectrum of the matrix $\mathbf{A}$ for four increasing values of collisionality: $\nu = 5 \times 10^{-5}, 1 \times 10^{-4}, 2 \times 10^{-4}, 5 \times 10^{-4}$ respectively in black, red, blue and gold dots. The black squares represent the Landau roots.

in the Fourier-Hermite space, to initialize the vector $\overrightarrow{C_j}$ as $(1, 0, 0, \ldots)^T$ (the electric field is proportional to C_0).

Figure 3.1 shows the temporal evolution of the absolute value of the Hermite coefficients $|C_n|$ in logarithm scale. Since the filamentation in velocity space naturally produces small velocity scales, Hermite coefficients of increasingly higher modes are excited. When the largest mode gets excited, the truncation of the series acts as a reflecting boundary (around time $T \sim 75$), and the perturbation travels back towards lower modes. Around time $T \sim 150$, the electric field damping is abruptly interrupted and a value close to the initial value is restored. Let us note that, although the electric field will not be affected until the recurrence time $T \sim 150$, the distribution function is spuriously altered from time $T \sim 75$, that is when the perturbation reflects on the boundary.

As we mentioned earlier, the effect of a non-null collisionality in the Vlasov-Poisson linear operator is to modify the spectrum of eigenvalues. Landau damping is not anymore due to the phase-mixing of a continuous set of neutral mode. Moreover, for a large enough value of ν, it appears as the least-damped eigenvalue of the system. This is shown in Figure 3.2, where, for the same value of $k = k_1 = 0.35$, we show the spectrum of the matrix $\mathbf{A}$ for four increasing values of collisionality: $\nu = 5 \times 10^{-5}, 1 \times 10^{-4}, 2 \times 10^{-4}, 5 \times 10^{-4}$

(respectively in black, red, blue and gold dots). The damping rate γ and the wave propagation frequency ω are respectively shown on the horizontal and vertical axes of Fig. 3.2. The values corresponding to the theoretical Langmuir roots ($\gamma = \gamma_L = -3.37 \times 10^{-2}$ and $\omega = \pm 1.22$), obtained through the numerical evaluation of the Landau dispersion function roots, are shown as black squares. We emphasize that the spectrum of the matrix $\mathbf{A}$ differs from the spectrum of the infinite-dimensional Vlasov-Poisson-LB operator. In fact, while for the latter the Landau root is a discrete eigenvalue in the limit $\nu \to 0$, Figure 3.2 clearly shows that, in the presence of a finite velocity resolution, a small collisionality acts to distort the discrete representation of the Case-Van Kampen continuum. In other words, a sufficiently large collisionality value (depending on the velocity resolution) is needed in order to recover the Landau root as a discrete mode. Indeed, it is clear that, for $\nu = 5 \times 10^{-4}$ (gold points), the spectrum exhibits two eigenvalues overlapping with the proper Landau roots value and, therefore, the proper Landau damping is restored.

In order to clarify the behavior of the coefficients $|C_n|$ in the case where the collisionality restores the proper Landau damping (i.e. $\nu = 5 \times 10^{-4}$), we show in Fig. 3.3 the temporal evolution of the Hermite coefficients $|C_n|$. Clearly

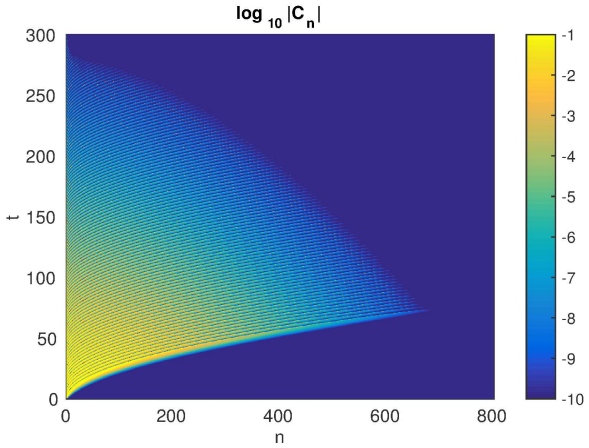

Figure 3.3: (Color online) Temporal evolution of the Hermite coefficients $|C_n|$ as a function of the Hermite mode n and the time t for the collisional $\nu = 5 \times 10^{-4}$ case.

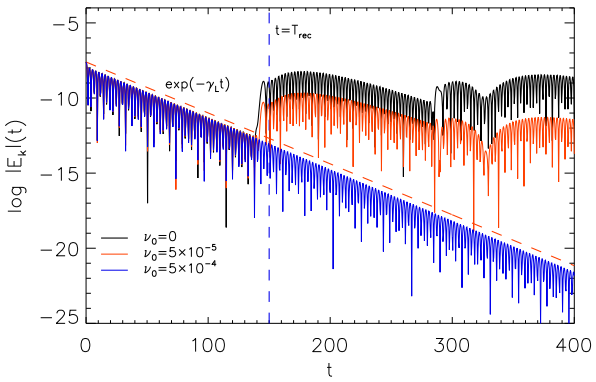

Figure 3.4: (Color online) Temporal evolution of $\log|E_k|(t)$ with $k = k_1$. The black, red and blue lines indicate respectively $\nu = 0$, $\nu = 5\times10^{-5}$ and $\nu = 5\times10^{-4}$. The red and blue dashed lines show respectively the theoretical damping with Landau damping γ_L and the instant time $t = T_{rec}$.

the reflecting effect discussed for Fig. 3.1 has now completely vanished and the electric field damping does not show any recurrence. Since the collisional operator damps the high Hermite modes or, in other words, since collisional effects stop the production of small velocity scales, the velocity filamentation is not correctly captured.

In order to complete our analysis, we numerically solve Eqs. (3.1)–(3.2) through the finite-difference numerical code presented earlier, for different values of the collisional frequency ν. We set the initial sinusoidal density perturbation such that the perturbation electric field amplitude is $\delta E = 10^{-3}$. The phase space is discretized with $N_x = 64$ and $N_v = 101$ points. Let us remark that, with the parameters choice just described, the recurrence time is $T_{rec} = 2\pi/k\Delta v \simeq 150$.

The time evolution of the logarithm of the absolute value of the first Fourier component $k = k_1$ of the electric field $\log|E_k|(t)$ is shown in Fig. 3.4. The black, red and blue lines correspond respectively to the collisionless case ($\nu = 0$), intermediate collisional case ($\nu = 5\times10^{-5}$) and stronger collisional case ($\nu = 5\times10^{-4}$). The last case is the case in which the Landau damping root is recovered in the spectrum shown in Fig. 3.2, thanks to the effect of collisions. The red and blue dashed lines in Fig. 3.4 indicates the

theoretical Landau damping rate $\gamma_L = -3.37 \times 10^{-2}$ and the recurrence time $t = T_{rec} \simeq 150$ respectively.

For the three cases, the electric field spectral component evolution is approximately the same for $t < T_{rec}$ and the electric field is damped at the proper Landau damping rate γ_L. Then, around $t = T_{rec} \simeq 150$, the collisionless and the intermediate collisional cases (black and red solid lines of Fig. 3.4) present a fake "jump" in the signal due to the initial state recurrence problem. On the other hand, in the stronger collisional case $\nu = 5{\times}10^{-4}$ (blue solid line of Fig. 3.4), the recurrence effect disappears and the unphysical "jump" is completely suppressed by collisional effects. It is worth to note that, in this case, the recurrence does not occur neither at times multiples of the recurrence period.

Based on the results presented above, the inclusion of a weakly collisional operator to prevent the numerical recurrence effect might look convenient; however, the consequences of including collisionality into the Vlasov-Poisson system must be investigated with care.

Figure 3.5 shows the difference between the damping rate γ_M of the least damped mode and the damping rate γ_L of the Landau root, as a function of the collisional rate ν, for three different values of $k = 0.35, 0.45, 0.55$, (black,

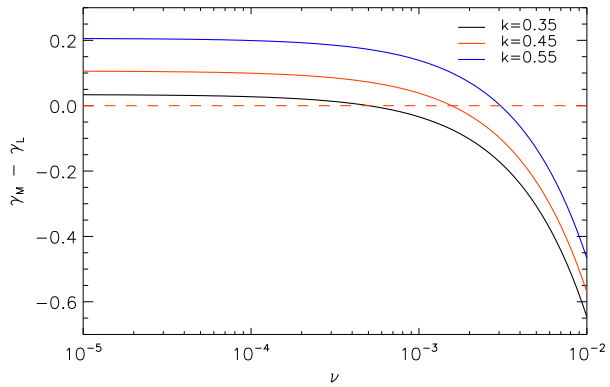

Figure 3.5: (Color online) The black, red and blue lines show the difference between the damping rate γ_M of the least damped mode and the damping rate γ_L of the Landau root, as a function of the collisional rate ν, for three different values of $k = 0.35, 0.45, 0.55$ respectively.

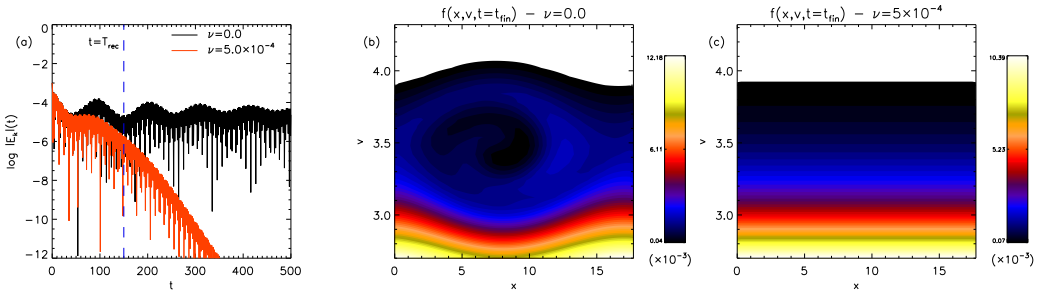

Figure 3.6: (Color online) (a) Temporal evolution of $\log|E_k|(t)$ with $k = k_1$ for the collisionless case (black line) and the collisional $\nu = 5 \times 10^{-4}$ case (red line). The blue dashed vertical line indicates the recurrence period T_{rec}. The distribution function around the phase speed $v = v_\phi$ at the final time instant $f(x, v, t = t_{fin})$ is shown in panels (b)–(c) for the collisionless (b) and collisional (c) case.

red and blue line, respectively). As explained in Figure 3.2, for $\nu \to 0$, and fixed velocity resolution, the Case-Van Kampen spectrum [175, 176] is recovered (see Fig. 3.2), and $\gamma_M \to 0$. The intersection between the red dashed and the solid lines indicates the value of collisionality that is required to recover the correct Landau damping as a discrete eigenmode. Moreover, bearing in mind that both γ_M and γ_L are negative quantities, values above the red-dashed line in the figure indicate that the collisional rate is not large enough to recover the Landau damping as the least damped eigenvalue, while values below the red-dashed line indicate over-damping with respect to the Landau damping. Figure 3.5 clearly indicates that there is not a single value of collisionality that would allow to recover the correct Landau damping for a spectrum of several wavenumbers. Since larger wavenumbers are subject to stronger damping, they would require a larger collisional rate.

Moreover, if the initial field amplitude is increased in order to explore the nonlinear evolution of the Landau damping, the collisionality, which was able of preventing recurrence in the linear simulation, becomes strong enough to smooth the nonlinear physical features of the Landau damping. In order to clarify this point, we perform a simulation with the same parameters of the linear one explained above (see Fig. 3.4) and we increase $\delta E = 10^{-1}$. Figure 3.6 (a) shows the time evolution of $\log|E_k|(t)$ for $k = k_1$ for the collisionless case (black solid line) and for the collisional case $\nu = 5 \times 10^{-4}$ (red solid

line). The blue dashed line in Fig. 3.6 indicates the recurrence period $T_{rec} = 2\pi/k\Delta v \simeq 150$. We remark that this specific value of collisional frequency is the one which prevents recurrence effects in the linear case, still preserving the correct value of Landau damping.

It is clear that, in the non-linear collisionless case, the Landau damping is arrested by nonlinear effects (particle trapping) and, as a consequence, the electric field starts oscillating around a nearly constant saturation level. On the other hand, in the collisional case, the physical scenario changes drastically and the electric field amplitude displays evident collisional damping.

In phase space, nonlinear effects manifest as the generation of a vortical trapping population, moving with velocity close to the wave phase speed ($v_\phi \simeq 3.50$). This is shown in Figs 3.6 (b)–(c) where the contour plots of the distribution function $f(x, v)$ at time $t = 400$ for the collisionless case (b) and for the collisional case (c) are reported. It is clear from the comparison of panels (b) and (c) of Fig. 3.6 that collisions prevent the generation of the phase-space trapping population, since they work to smooth out any deformation of the particle distribution function and to drive the system toward thermal equilibrium. In other words, as soon as kinetic effects produce distortions (and, consequently, sharp velocity gradients) of the particle distribution, collisional effects become more intense to keep the velocity distribution close to a Maxwellian. Therefore, it is quite clear that collisional effects are not able to prevent the recurrence problem without destroying the plasma dynamics characteristics.

In order to understand whether changing the resolution in velocity space [165, 166] affects the physical features of the system, we performed additional simulations in collisionless regime, increasing the number of gridpoints in the velocity domain: $N_v = 101, 201, 401, 1001, 2001, 4001$; $N_v = 101$ [indicated with blue crosses in Figs. 3.7 (a–b)] corresponds to the case depicted in Fig. 3.6.

We computed the following quantities as "proxies" of numerical accuracy:

- The oscillation period T_{osc} of the wave, evaluated in the time interval $t \geq T_{rec}$);

- The time t_{max} where the electric field envelope reaches its first maximum [$\simeq 100$ in Fig. 3.6(a)];
- The oscillation period τ of the electric field envelope, defined as the average of the difference between two consecutive maximum points in the $\log|E_k|(t)$ evolution;
- The saturation electric field $E_{k,sat}$ at which the electric field spectral power saturates.

The quantities T_{osc} and t_{max} (not shown here) do not depend on N_v, the relative variations between the two extremes cases ($N_v = 101$ and $N_v = 4001$) being always smaller than the 1%. On the other hand, in Fig. 3.7 we report the dependence of $E_{k,sat}$ (a) and τ (b) on N_v. Clearly, these two quantities approach a saturation value (red-dashed line) as N_v increases. The relative variations between the values obtained with $N_v = 101$ and the corresponding saturation values (red dashed lines) are about the 4% for $E_{k,sat}$ and 10% for τ. We conclude that even in the nonlinear case shown in Fig. 3.6 the limited resolution in the velocity domain slightly affects the physical evolution of the system. However, as discussed above, adding a collisional operator to eliminate these unphysical effects produces drastic changes in the kinetic aspects of the dynamics with respect to the collisionless case.

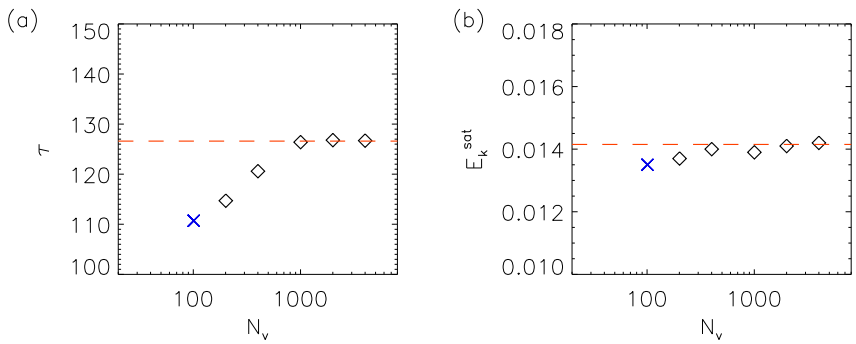

Figure 3.7: (Color online) The oscillation period of the electric field envelope τ (a) and the saturation electric field $E_{k,sat}$ (b) as a function of N_v. The blue crosses indicate the N_v case case depicted in Fig. 3.6.

3.1.3 Bump-on-tail instability

In the current section the recurrence effects on the bump-on-tail instability are described by performing a similar analysis to that performed in the previous Section. The initial distribution function is the following:

$$f_0(v) = \frac{n_0}{(2\pi T_0)^{1/2}} \exp\left(-\frac{v^2}{2T_0}\right) + \frac{n_b}{(2\pi T_b)^{1/2}} \times \left[\exp\left(-\frac{(v-V_b)^2}{2T_b}\right) + \exp\left(-\frac{(v_x+V_b)^2}{2T_b}\right)\right] \tag{3.14}$$

The core density and temperature are respectively $n_0 = 0.98$ and $T_0 = 1$, while the bump density, mean velocity and temperature are $n_b = 0.01$, $V_b = 4$ and $T_b = 0.4$ respectively. Is it clear that $f_0(v)$ represents a Maxwellian distribution function to which two bumps are superimposed at both positive and negative side of the velocity domain. Moreover the velocity symmetry in the velocity shape of $f_0(v)$ guarantees an initial null current. In Hermite space, the parity of $f_0(v)$ translates to having $C_n^{eq} = 0$ for all odd n.

First of all, as performed in Sec. 3.1.2, we study the collisionless ($\nu = 0$) linear evolution of the bump-on-tail instability onset for $k = k_1 = 2\pi/L = 0.25$ (being the plasma length $L = 25$) by perturbing initially the system

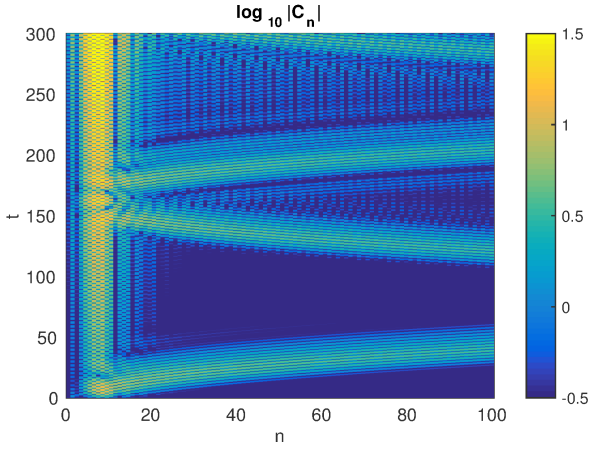

Figure 3.8: (Color online) Temporal evolution of the Hermite coefficients $|C_n|$ as a function of the Hermite mode n and the time t for the collisionless $\nu = 0$ case.

through a spatially sinusoidal electric field perturbation. Here the Hermite modes number is $N_H = 400$. Figure 3.8 shows the temporal evolution of the absolute value of the Hermite coefficients $|C_n|$. Only the first 100 modes are shown, to better appreciate the recurrence on the low order modes. As in Fig. 3.1 for the Landau damping, the filamentation creates small velocity scales and, due to the truncation of the Hermite series - which corresponds, in the Eulerian code, to the presence of a finite velocity grid size - the boundary reflects back the perturbation towards lower modes. The main difference with respect to the Landau damping case is that now there is an eigenmode whose amplitude grows exponentially in time. The eigenmode has a certain structure in Hermite space, and is localized between modes 5 and 10. Once the filamentation bounces back because of the truncation of the series, the unstable eigenmode is perturbed, around time $T \sim 150$. Therefore, in the bump-on-tail case, the recurrence is much more evident as a fake perturbation acting on the unstable eigenmode, rather than on the electric field. In fact, as we show in the following, the recurrence of the electric field is more modest than for the Landau damping case.

In order to clarify how the recurrence acts on the instability onset, we perform some Eulerian simulations where the phase space is discretized with $N_x = 128$ point while N_v is variable in order to change the recurrence period: $N_v = 101$ ($T_{rec} \simeq 200$), $N_v = 201$ ($T_{rec} \simeq 400$) and $N_v = 1001$ ($T_{rec} \simeq 2000$). We perturb the system through a sinusoidal density perturbation whose wavenumber is $k = k_1 = 0.25$. The density perturbation amplitude is $\delta n = 2.51 \times 10^{-6}$ which corresponds to a perturbed electric field of amplitude $\delta E = 10^{-5}$. By evaluating the dispersion function roots of the Vlasov equation we can calculate, for the specific wavenumber, the linear growth rate of the instability $\gamma_I^{th} = 9.20 \times 10^{-3}$ and the wave phase speed $v_\phi = 3.90$.

Figures 3.9 (a)–(b) show respectively the temporal evolution of $\log |E_k|(t)$ with $k = k_1$ and the phase space contour plot at the final time of the simulation $t = t_{fin}$ for the high resolution case ($N_v = 1001$). Clearly the instability is not affected by the recurrence and, in the linear stage, the field amplitude grows up exponentially in accordance with the theoretical prediction [red

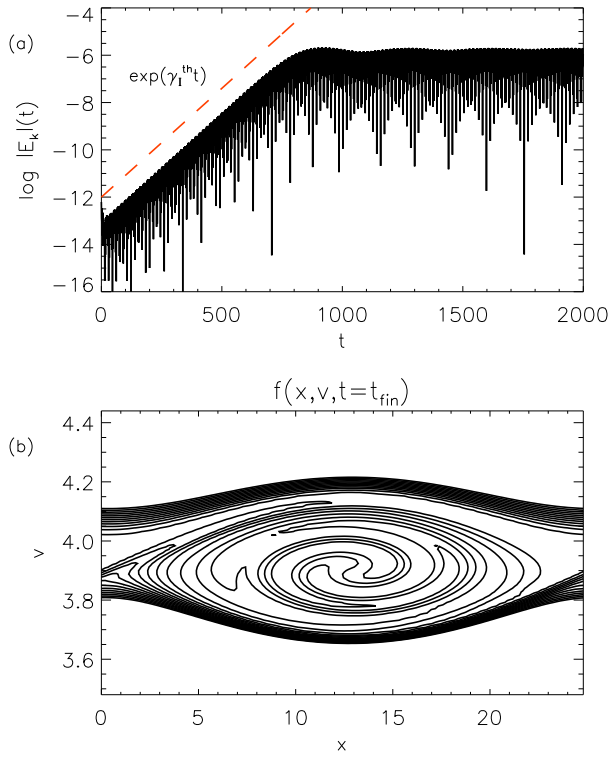

Figure 3.9: (Color online) (a) Temporal evolution of $\log|E_k|(t)$ with $k = k_1$ for the collisionless recurrence-free ($N_v = 1001$) case. The red dashed line represents the theoretical growth expectation $\exp(\gamma_I^{th} t)$. (b) Contour plot of the distribution function around the phase space $v = v_\phi$ at the final time instant $f(x, v, t = t_{fin})$.

dashed line in Fig. 3.9 (a)]. As nonlinear effects become important, the field saturates at a constant value and in the phase space, a BGK-like structure [146, 157] is formed [see Fig. 3.9(b)]. The phase space structure is well-localized around the phase speed $v = v_\phi$ and its width is quite in accordance with the theoretical prediction.

In contrast with the case just shown, when the velocity resolution decreases, recursive effects occur. Panels of Figs. 3.10 show the results of two simulations with resolution $N_v = 101$ (left column) and $N_v = 201$ (right column). For each column, the top panel [Figs. 3.10 (a)–(b)] describes the temporal evolution of $\log|E_k|(t)$, while the center panel [Figs. 3.10 (c)–(d)] displays the quantity $\Delta E_{k\%}$, defined as the relative difference (expressed in

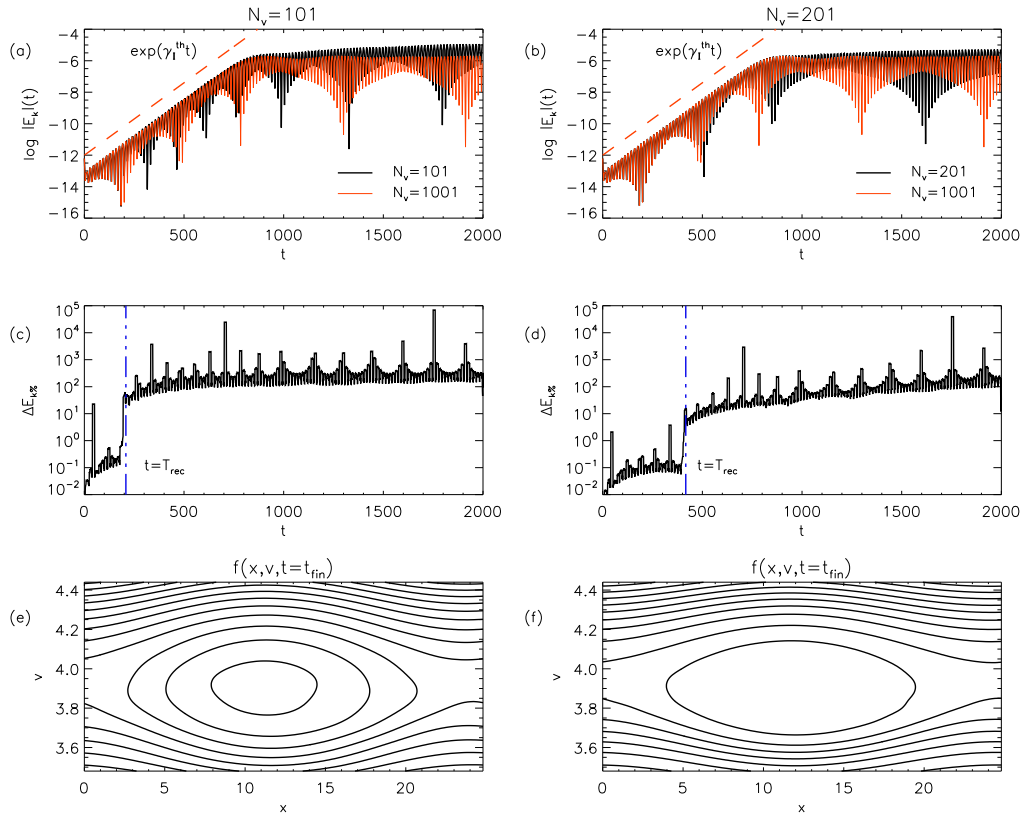

Figure 3.10: (Color online) Recurrence effects on the bump-on-tail instability for the $N_v = 101$ (left column) and $N_v = 201$ (right column) simulations. The top panels (a)–(b) show the temporal evolution of $\log|E_k|(t)$ with $k = k_1$ for the low-resolution case (black line) and for the recurrence-free case (red solid line), while the red dashed line indicates the theoretical growth expectation $\exp(\gamma_I^{th} t)$. The central panels (c)–(d) display the quantity $\Delta E_{k\%}$ (black line) and the recurrence period $t = T_{rec}$ (blue dashed line). Finally the bottom panels (e)–(f) visualize the distribution function contour plot around the phase space $v = v_\phi$ at the final time instant $f(x, v, t = t_{fin})$.

percentage) between $|E_k|(t)$ at a given resolution and $|E_k|(t)$ for the collisionless recurrence-free case. Finally, the bottom contour plot [Figs. 3.10 (e)–(f)] exhibits the distribution function $f(x, v, t = t_{fin})$ at the final time and around the phase speed $v = v_\phi$. Let us remark that, in order to better visualize the phase space structures in Fig. 3.10 (e)–(f), we performed an interpolation of the distribution function over a more resolved grid without altering the physical features of the phase space structure itself.

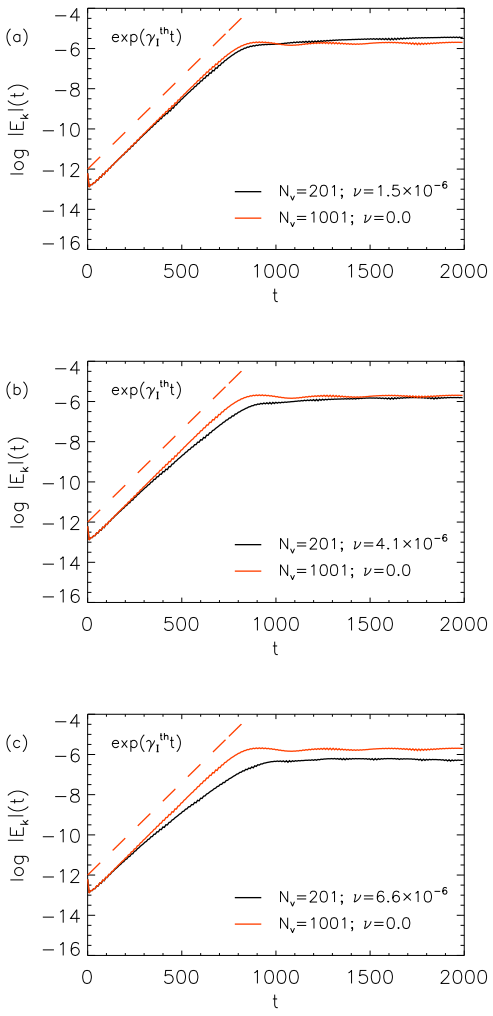

Figure 3.11: (Color online) Temporal evolution (black line) of $\log|E_k|(t)$ with $k = k_1$ for the case $N_v = 201$ and with collisional frequency $\nu = 1.5 \times 10^{-6}$ (a), $\nu = 4.1 \times 10^{-6}$ (b) and $\nu = 6.6 \times 10^{-6}$ (c) respectively. In each panel the red solid line shows the evolution of $\log|E_k|(t)$ for the collisionless recurrence-free ($N_v = 1001$) case while the red dashed line displays the theoretical linear instability growth.

It is clear that the recurrence also manifests in the instability onset. By focusing on the linear stage of the instability growth, the electric field amplitude seems to exponentially increase at a rate in accordance with the theoretical expectations, represented with red dashed lines in Figs. 3.10 (a)–

(b). Moreover, as introduced above, in contrast with the Landau damping case, the recurrence effect does not strongly manifest as a fake jump around the recurrence time $t = T_{rec}$. However, by analyzing the temporal evolution of $\Delta E_{k\%}$ [see Figs. 3.10 (c)–(d)], an abrupt increase of $\Delta E_{k\%}$ is observed around the recurrence period, shown in Figs. 3.10 (c)–(d) with blue dashed lines. This discontinuity is due to recursive effects and it means that, after the recurrence period, the electric field evolution in the case with a lower resolution strongly departs from the recurrence-free case ($\Delta E_{k\%} \simeq 100\%$). Thus, although recursive effects cannot be appreciated in the linear stage of the instability growth by looking directly at Figs. 3.10 (a)–(b) (the scale is logarithmic and a variation about the 100% cannot be easily highlighted), the field evolution is actually disturbed by recurrence.

Furthermore, recurrence phenomena affect the nonlinear evolution of the instability. Effectively, by focusing on Fig. 3.10 (a)–(b), in the case without recurrence the electric field power opportunely saturates at a constant value (red line) while, on the other hand in the cases with recurrence the electric field does not saturate and it continues to slowly increase. Finally, by focusing on the distribution function at the final time instant $t = t_{fin}$ [see Figs. 3.10 (e)–(f)], in both cases a phase space structure is produced around the correct phase speed. By comparing these phase space structures with the hole created in the recurrence-free case [Fig. 3.9 (b)], some differences clearly reveal. First, phase space structures obtained in the cases with recurrence are less resolved compared to the one of the recurrence-free case and this is obviously related to the different velocity grid size: effectively, since the velocity grid size is smaller in the recurrence-free case, finer scales are naturally created compared to the cases at lower resolution. Moreover, the vortex width seems to be slightly wider in the $N_v = 101$ case [Fig. 3.10 (e)] compared to both the collisionless recurrence-free case [Fig. 3.9 (b)] and to the $N_v = 201$ case [Fig. 3.10 (f)]. In other words, since the electric field does not saturate in presence of recursive effects, the phase space structure tends to increase its width.

The effects of the initial state recurrence on the bump-on-tail instability represents a novel and quite unexpected feature in the analysis of the re-

cursive phenomena. Both linear and nonlinear stages of the instability are affected by recurrence: the electric field evolution departs from the evolution in the case without recurrence ($N_v = 1001$) around $t = T_{rec}$. Furthermore the nonlinear saturation, which is properly retained in the case at high resolution, is interrupted by recurrence as the velocity grid size gets larger. Moreover, due to the absence of the electric field saturation, the distribution function shows a vortex properly centered around the right phase speed but whose width tends to be bigger compared to the case without recurrence. Finally, although initial state recurrence phenomena are often related to linear physical problems, here we have found some new and interesting recurrence effect features which occur in the nonlinear regime.

In order to explore if a collisionality described by the LB operator could represent a good way to prevent numerical recurrence in the case of the bump-on-tail instability, we focus on the $N_v = 201$ resolution case ad we perform several collisional simulations by changing the collisional frequency ν.

Figs. 3.11 (a)–(c) display, through black lines, the temporal evolution of $\log|E_k|(t)$ with $k = k_1$ for the cases: $\nu = 1.5 \times 10^{-6}$ (a), $\nu = 4.1 \times 10^{-6}$ (b) and $\nu = 6.6 \times 10^{-6}$ (c). In each panel of Fig. 3.11 red solid lines indicate the evolution in the collisionless case without recurrence [the same shown in Fig. 3.9 (a) and in Figs. 3.10 (a)–(b)] while the red dashed line shows the theoretical expectation for the instability growth curve $\exp(\gamma_I^{th} t)$, being $\gamma_I^{th} = 9.2 \times 10^{-3}$.

As expected, collisions inhibit the instability and tend to restore thermal equilibrium. However in the case $\nu = 1.5 \times 10^{-6}$ [see Fig. 3.11 (a)], collisions weakly affect the electric field evolution which, as in the collisionless case, do not saturate and overtake the recurrence-free case evolution [red line in Fig. 3.11 (a)].

As collisional frequency increases, the electric field evolution tends to be dissipated. In the intermediate case $\nu = 4.1 \times 10^{-6}$ [see Fig. 3.11 (b)], the electric field reaches, at the end of the simulation, almost the same power of the collisionless case without recurrence; however its evolution departs from the reference red curve around $t \simeq 600$, where the recurrence-free case [red

line in Fig. 3.11 (b)] presents a stronger power level than the collisional $N_v = 201$ case [black line in Fig. 3.11 (b)]. On the other hand, in the case $\nu = 6.6 \times 10^{-6}$ [see Fig. 3.11 (c)], a significant difference between the two evolutions appears at even smaller time instants and collisions clearly affect the linear instability regime. In particular, the linear growth rate in the collisional $N_v = 201$ case [black line in Fig. 3.11 (c)] is significantly smaller than the collisionless $N_v = 1001$ case [red line in Fig. 3.11 (c)]. Moreover, as in the collisionless recurrence-free case, at the final stages of the simulation the electric field spectral power exhibits an almost flat behavior at a lower power value compared to the collisionless recurrence-free case.

In order to point out how phase space is affected by collisions, Figs. 3.12 (a)–(c) show the contour plots of the distribution function $f(x, v, t = t_{fin})$ at the final time instant $t = t_{fin}$ and zoomed around the phase speed $v = v_\phi$ for the cases: $\nu = 1.5 \times 10^{-6}$ (a), $\nu = 4.1 \times 10^{-6}$ (b) and $\nu = 6.6 \times 10^{-6}$ (c). As in Fig. 3.10 (e)–(f), even in Fig. 3.12 (a)–(c) we performed an interpolation of the distribution function over a more resolved grid. In all the three cases shown in Fig. 3.12 (a)–(c) a phase space structure is observed around the wave phase speed and its width reduces as collisional frequency increases. Clearly as collisions become stronger, phase space structures are smoothed out and present a smaller size.

We highlight that, as collisional frequency gets bigger, the instability is affected by collisions more intensely. Moreover, since collisions tend to restore the equilibrium, they have been active since the initial stage of the simulation (the initial distribution function is out of equilibrium). Furthermore they remain active until the equilibrium is recovered and incessantly work to smooth out all the wave features (electric field signal and phase space structures). Therefore, at longer times (not shown here), the phase space structures shown in Figs. 3.12 get smaller and disappear, while the electric field signal shown in Figs. 3.11 is dissipated by collisional effects. We conclude that, as in the nonlinear Landau damping case, an artificial collisionality is not able to prevent the initial state recurrence in the bump-on-tail instability onset. In particular we found two different scenarios: collisions are so weak that recurrence is still active or, on the other hand, they affect both

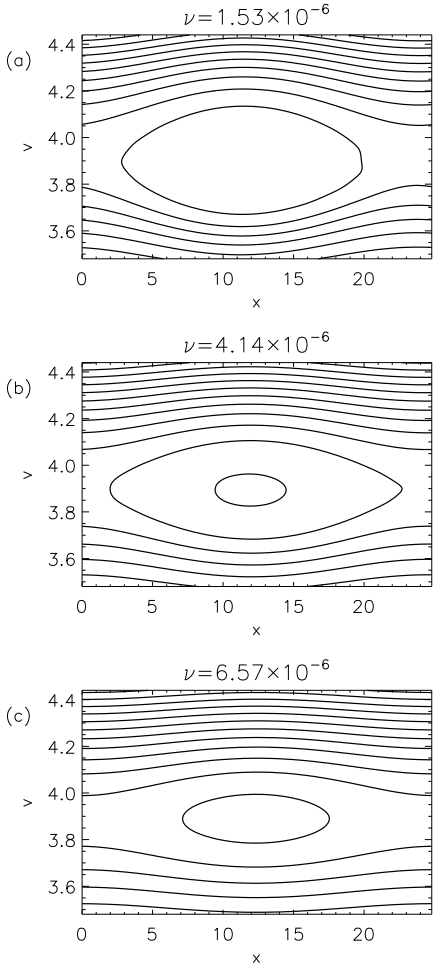

Figure 3.12: (Color online)The distribution function contour plots around the phase space $v = v_\phi$ at the final time instant $f(x, v, t = t_{fin})$ for the case $N_v = 201$ and with collisional frequency $\nu = 1.5 \times 10^{-6}$ (a), $\nu = 4.1 \times 10^{-6}$ (b) and $\nu = 6.6 \times 10^{-6}$ (c).

recurrence effects and physical evolution of the system by deeply smoothing the electric field and the phase space structure.

3.1.4 Summary

In this section we analyzed in detail the problem of the initial state recurrence in a weakly collisional plasma, where electron-electron collisions have been modeled through the Lenard-Bernstein collisional operator [139]. We

focused on two study cases: the Landau damping of a Langmuir wave and the bump-on-tail instability onset. For both cases, the analysis in the linear regime has been performed through the decomposition of the linear Vlasov-Poisson system into the Fourier-Hermite space. In particular, the expansion of the distribution function in terms of Hermite functions separates naturally different velocity scales and it allows to better describe recursive effects and appreciate the role of the collisional operator in phase space. Moreover, the analysis has been extended to the nonlinear regime through a $1D$–$1V$ Eulerian collisional Vlasov-Poisson code, already tested and used in previous works (see Refs. [62, 63]).

Recently some authors (see Refs. [172, 177, 178] and references therein) pointed out that an opportune collisionality can prevent the onset of recursive effects and restore the correct Landau damping. This indication suggested us to investigate whether the inclusion of an artificial collisionality could be used to prevent recurrence in numerical simulations without the loss of physical details due to collisional effects. However, we have shown that the collisional frequency ν which is suitable for preventing numerical recurrence in the linear regime depends on the perturbation wavenumber; furthermore, collisional effects become important when the system evolves to the nonlinear regime and, for the same value of collisionality which prevents recursive effects in the linear stage, any nonlinear wave is strongly dissipated by collisional effects.

Finally, we pointed out that numerical effects associated to the generation of fine velocity scales can modify the physical features of the system evolution even in nonlinear regime. This has been shown by focusing on the nonlinear Landau damping phenomenon and on the bump-on-tail instability both in linear and nonlinear regime. Our results indicate that filamentation-like and recursive effects, often associated with evolution in linear regime, can also be important in the nonlinear case. We also conclude that the addition of a collisional operator, with the aim of preventing the recurrence of the initial state and other numerical effects related to limited resolution in the velocity domain, significantly changes the evolution of nonlinear waves and the corresponding phase space portrait.

3.2 Secondary waves branch in an externally forced plasma

In the present section we describe, by means of Eulerian Vlasov-Poisson simulations, the method adopted for triggering waves in laboratory plasmas devices, like, for example, Penning-Malmberg traps [50, 145, 182]. Plasma waves are usually launched through an external electric potential, localized in a particular region of the plasma column. This driver oscillates in time [$\phi_D \simeq sin(\omega_D t)$, being ω_D the driver pulsation] and it is adiabatically turned on and off to select the waves frequency [50, 145, 179, 180, 181, 182].

On the other hand, when the dynamics of these systems is modeled by means of numerical simulations, external drivers select at the same time pulsation and wavenumber [$E_D \simeq \sin(kx - \omega_D t)$, where $\omega_D/k = v_{\phi,D}$]. As in experimental setups, these external drivers are also turned on and off adiabatically. This kind of drivers has been widely implemented to excite Trivelpiece-Gould (TG) waves, EAWs [143, 144, 183, 184, 185] or KEEN Waves [129, 137, 138, 159] as well as for the analysis of auto-resonance process [186, 187].

The two types of drivers described above present different features: in experiments, the driver is spatially localized while, in simulations, it usually permeates all the computational box. To resolve this discrepancy, we implement in a numerical simulation a more *realistic*, localized driver and analyze the wave triggering process in detail. We consider both the cases of a collisionless and a weakly collisional plasma composed of kinetic electrons and a background of motionless ions. Electron-electron collisions are modeled through the one-dimensional Dougherty operator [58, 59, 62, 63, 134, 135, 136]. In this framework, we study the excitation of linear Langmuir waves and nonlinear EAWs. By focusing on the Langmuir waves case, we describe the basic mechanism which selects frequency and wavenumber of the waves. As we will show in detail in the following, the driver field is composed of a temporal adiabatic function, which selects the mode frequency through a resonance process, and of a spatial localization function exciting several spatial Fourier components. This represents a novel features compared to previous simu-

lations (see Refs. [129, 137, 138, 144, 159, 184, 185]) where only a "single" wavenumber was excited.

Then, we analyze the triggering process of EAWs, which are undamped acoustic-like waves, whose phase speed is about the electron thermal speed ($v_\phi^{EAW} \simeq 1.31 v_{th}$). It is worth to note that the standard Vlasov-Poisson linear theory based on a Maxwellian equilibrium distribution function predicts that these fluctuations are heavily damped. However, Holloway and Dorning [142] showed that, when the equilibrium distribution function presents flat regions with vanishing velocity derivative, undamped EAWs appear as nonlinear solutions of the Vlasov-Poisson system and exhibit Bernstein-Greene-Kruskal modes-like characteristics [146]. Let us also remark that nonlinear modes whose phase speed is close to the thermal speed has been predicted for astrophysical plasmas [29, 188] and recently observed in solar wind data [189, 190].

When we trigger EAWs in our simulations, surprisingly a new branch of nonlinear and non-dispersive waves is observed in the collisionless case beyond the standard EAWs fluctuations. The phase speed of these fluctuations is about $\simeq 0.5 v_{th}$ ($v_\phi^{EAW}/3$) and they are generated by the localized driver, which perturbs the VDF in several phase space regions. Indeed, the VDF exhibits a small bump around $v \simeq 0.5 v_{th}$ as a result of the driver effects, therefore a beam-like instability could cause the onset of these modes.

Moreover we show that, also for small values of collisionality, these secondary waves are not recovered; this suggests that collisions inhibit the formation of small scale structures in the VDF and, hence, the triggering of secondary beam-modes. This is probably the reason why these fluctuations are not routinely observed in laboratory plasma experiments, where a low level of collisionality is always present. It is worth to point out that, despite we analyzed a neutral plasma, the wave launching mechanism is quite general and our considerations could be easily extended to nonneutral plasmas.

The structure of the section is the following: in Sec. 3.2.1 we theoretically analyze the basic equations system and the action of the localized driver and we briefly describe our numerical code. Then, in Sec. 3.2.2, we focus on the triggering of linear Langmuir waves and on the basic frequency resonance

process. Then, in Sec. 3.2.3, we analyze the EAWs launching process in both a collisionless [Sec. 3.2.3] and a weakly collisional [Sec. 3.2.3] plasma.

3.2.1 Theoretical analysis

We consider a plasma composed of kinetic electrons and motionless protons within the electrostatic approximation. Electron-electron collisions are included at the right-hand side of the Vlasov equation through the one-dimensional Dougherty operator [58, 59, 134, 135]. We solve the following dimensionless Dougherty-Poisson (DP) equations, in $1D$–$1V$ phase space configuration:

$$\frac{\partial f}{\partial t} + v\frac{\partial f}{\partial x} + \frac{\partial\left(\phi+\phi_D\right)}{\partial x}\frac{\partial f}{\partial v} = \left.\frac{\partial f}{\partial t}\right|_{coll} \tag{3.15}$$

$$-\frac{\partial^2\phi}{\partial x^2} = 1 - \int f\ dv\ ; \tag{3.16}$$

where $f = f(x,v,t)$ is the electron distribution function, $\phi = \phi(x) = -dE/dx$ is the electrostatic potential (E is the electric field), $\phi_D = \phi_D(x)$ is the external potential driver and $\partial f/\partial t|_{coll}$ is the Dougherty collisional operator. Due to their inertia, protons are considered as a motionless neutralizing background of constant density $n_0 = 1$. In previous equations, time is scaled to the inverse electron plasma frequency ω_{pe}, velocities to the initial electron thermal speed $v_{th,e}$; consequently, lengths are normalized by the electron Debye length $\lambda_{De} = v_{th,e}/\omega_{pe}$ and the electric field by $\omega_{pe}m_e v_{th,e}/e$ (m_e and e being the electron mass and charge, respectively). For the sake of simplicity, from now on, all quantities will be scaled using the characteristic parameters listed above.

The Dougherty collisional operator [58, 59] has the following form:

$$\left.\frac{\partial f}{\partial t}\right|_{coll} = \nu(n,T)\frac{\partial}{\partial v}\left[T\frac{\partial f}{\partial v} + (v-V)\,f\right]\ ; \tag{3.17}$$

here, $\nu(n,T)$ is the collisional frequency:

$$\nu(n,T) = \nu_0 \frac{n}{T^{3/2}} \; ; \; \nu_0 = \frac{g \ln \Lambda}{8\pi} \; ; \tag{3.18}$$

where $g = 1/n\lambda_D^3$ is the plasma parameter, $\ln \Lambda \simeq -\ln g/3$ is the Coulombian logarithm, subscript j indicates the j-th vector component and $n = \int dv f$, $V = 1/n \int dv \; vf$, $T = 1/3n \int dv \; (v-V)^2 f$ are respectively plasma density, mean velocity and temperature. The Einstein convention has been introduced in Eq. (3.17).

The driver shape $\phi_D(x,t)$ is the following:

$$\phi_D(x,t) = \phi_0 \; h(x) g(t) \sin(\omega_D t) \; , \tag{3.19}$$

being respectively

$$g(t) = \left[1 + \left(\frac{t-\tau}{\Delta\tau} \right)^{n_g} \right]^{-1} ; \quad h(x) = \left[1 + \left(\frac{x - x_0}{\Delta x_0} \right)^{n_h} \right]^{-1} \tag{3.20}$$

the temporal $g(t)$ and spatial $h(x)$ adiabatic functions which respectively model the antenna "locality" and the adiabatic turning on and off function of the driver. Since the electrostatic potential is spatially localized, the electric field becomes spread in terms of spatial Fourier components. On the other hand, the temporal function $g(t)$ selects the frequency ω of the plasma modes. Indeed, the Fourier transform of $g(t)$ is localized around the driver frequency ω_D with a width comparable with $1/\Delta\tau$. Therefore, as the driver temporal extension gets bigger, the driver frequency width becomes smaller. In Eqs. (3.20) $x_0 = L/2$, $\Delta x_0 = L/16$ and $n_h = 16$, while the values of τ, $\Delta\tau$ and n_g will be given later in the next section. Eqs. (3.15)–(3.16) are solved with the same methods described in previous section and in Refs. [62, 63]. The phase space is here discretized with $N_x = 256$ gridpoints in the physical domain $D_x = [0, L]$ and $N_v = 12001$ gridpoints in the velocity domain.

In the following sections we describe simulations results about Langmuir waves (Sec. 3.2.2) and EAWs (Sec. 3.2.3). In both cases, the initial condition is a homogeneous Maxwellian without any density perturbation.

3.2.2 Langmuir waves

Here we describe the results of three different simulations, whose parameters are listed in Tab. 3.1. For all the simulations the driver is turned on for a time interval $\Delta\tau = 40\ T$, being T the wave period, while $E_D = 5 \times 10^{-6}$.

SIM	L	$k_1 = k_0 = 2\pi/L$	ω_D	$\omega_D = \omega(k)$
A	26	0.242	1.098	YES, for $k = k_1$
B	26	0.242	1.200	NO, for any k
C	200	0.031		YES, for $k = k_1$

Table 3.1: Parameters of the Langmuir waves simulations.

In the first simulation (SIM A), the driver oscillates at a frequency ω_D which is in resonance with the $\omega(k_1)$ plasma mode frequency, being $\omega(k_1)$ evaluated with a linear numerical solver. Figure 3.13 shows the time evolution of the first two electric field Fourier components $|E_k|(t)$ in black solid ($k = k_1$) and red dashed ($k = k_2$) lines. $|E_{k_2}|(t)$ is reported as an illustrative case for other non-fundamental Fourier components, which exhibit similar behaviors to $|E_{k_2}|(t)$. Yellow vertical lines indicate the time instants $t = \tau_1$ and $t = \tau_2$, corresponding to the times when the driver is set on and off. For the sake of simplicity let us analyze Fig. 3.13 by considering three time periods: $t \leq \tau_1$ (I) , $\tau_1 \leq t \leq \tau_2$ (II) and $t \geq \tau_2$ (III).

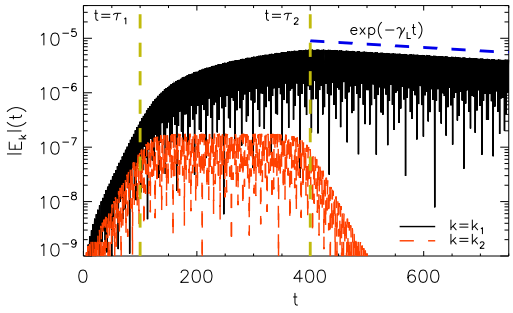

Figure 3.13: (Color online) Time evolution of $|E_k|(t)$ for $k = k_1$ (black line) and $k = k_2$ (red line) relative to SIM A. The two yellow vertical lines indicate the time instants at which the driver is turned on $t = \tau_1$ and off $t = \tau_2$, while the blue dashed line represents the theoretical exponential damping with damping rate γ_L.

When the driver grows up adiabatically (I), several Fourier components increase their powers and $|E_{k_1}|(t)$ overtakes the non-fundamental components. Then, while the driver is on (II), the difference between $|E_{k_1}|(t)$ and the other Fourier components becomes stronger. The power of the fundamental component continues to increase and $|E_{k_1}|(t)$ exhibits a non-flat profile, due to the fact that the plasma is responding to the external driver through the Langmuir wave generation. The other components remain instead at the power level due to the driver. When the driver is turned off (III), only $|E_{k_1}|(t)$ survives and displays an exponential damping, whose coefficient is in agreement with the Landau damping rate $\gamma_L = -1.404 \times 10^{-3}$ [blue dashed curve in Fig. 3.13(a)].

In this case (SIM A) the launching mechanism is quite clear: the external electric field drives several spatial Fourier components but, at the same time, it temporally selects the driving frequency. The driver pulsation is perfectly resonant with the theoretical pulsation of the Langmuir wave $\omega(k)$ with $k = k_1$, therefore the plasma response occurs at a pure Langmuir wave. Other spatial components, which could be excited by the driver spatial localization, are not effectively triggered because they are not resonant with the driver [$\omega(k_j) \neq \omega_D$ for $j \neq 1$].

The second simulation (SIM B) has the same parameters as SIM A except for the driver frequency which is now $\omega_D = 1.20$ [$\omega_D \neq \omega(k_j)$ for all the set of k_j]. Figure 3.14(a) shows the time evolution of the first two electric field Fourier components $|E_k|(t)$ in black solid ($k = k_1$) and red dashed ($k = k_2$) lines. The yellow vertical lines indicate the instants $t = \tau_1$ and $t = \tau_2$, corresponding to the times when the driver is set on and off.

The evolution of non-fundamental components [compare the red curves of Fig. 3.13 and 3.14(a)] is the same of the on-dispersion (SIM A) case, being in both simulations the $k = k_2$ wavenumber not resonant with the driver [$\omega(k_2) \simeq 1.60$]. However, $|E_{k_1}|(t)$ does not increase while the driver is turned on and it remains almost at the driver level. When the driver is turned off, the electric field $|E_{k_1}|(t)$ is damped out at the correct Landau damping rate [blue dashed line in Fig. 3.14 (a)]. It is also significant to evaluate the oscillation peaks of E_k for a given k. Fig. 3.14(b) reports $|E_{k_1}(\omega)|$ shape as a function

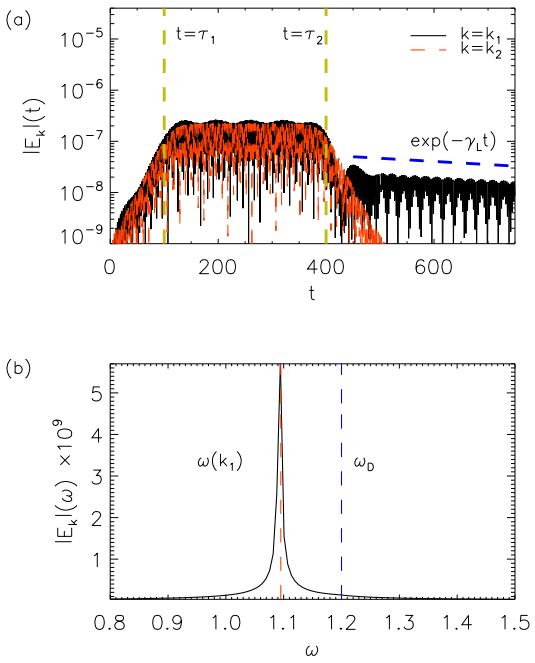

Figure 3.14: (Color online) (a) Time evolution of $|E_k|(t)$ for $k = k_1$ (black line) and $k = k_2$ (red line) relative to SIM B. The two yellow vertical lines indicate the time instants at which the driver is turned on $t = \tau_1$ and off $t = \tau_2$, while the blue dashed line represents the theoretical exponential damping with damping rate γ_L. (b) Oscillation peak of the first Fourier component of the electric field, given by the profile of $|E_k(\omega)|$ as a function of ω. The peaks are evaluated after that the driver has been set off. The blue and red dashed lines represent respectively the driver pulsation ω_D and the "proper" Langmuir wave frequency $\omega(k_1)$.

of ω, being $|E_{k_1}(\omega)|$ the temporal Fourier transform of $E_k(t)$ preformed in the temporal range when the driver is turned off. Clearly $|E_{k_1}(\omega)|$ peaks at the Langmuir mode frequency $\omega(k_1)$. This indicates that, once the driver has been set off, the plasma excites the Langmuir mode with frequency $\omega(k_1)$, thus resulting in a frequency shift from ω_D to $\omega(k_1)$.

To understand the results described above for SIM A and SIM B, we numerically evaluated, for each set of parameters in Tab. A, the Fourier transform of the temporal part of the driver $g(t)\sin(\omega_D t)$:

$$\eta(\omega) = \int_0^\infty dt e^{-i\omega t} \frac{\sin \omega_D t}{1 + \left(\frac{t-\tau}{\Delta\tau}\right)^{n_g}} , \tag{3.21}$$

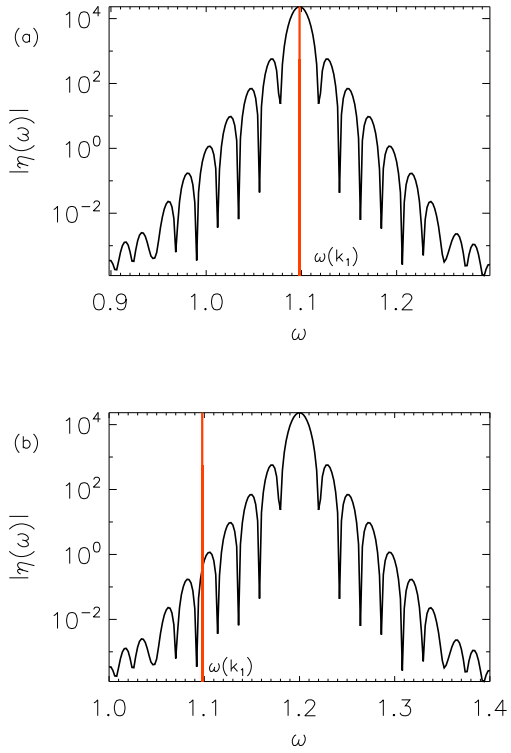

Figure 3.15: (Color online) Absolute value of $\eta(\omega)$ for the SIM A (a) and SIM B (b). The red curves in both panel indicate the "proper" Langmuir frequency $\omega(k_1)$.

which gives information about the frequency window that each wavenumber feels during the driving process. Figures 3.15 (a)–(b) show the profile of $|\eta(\omega)|$ as a function of ω for the on-dispersion (SIM A) case (a) and for the off-dispersion (SIM B) case (b). The red solid lines in Figs. 3.15 (a)–(b) indicates the Langmuir modes frequency. In SIM A, the driver is resonant with the mode frequency $\omega(k_1)$ [see Fig. 3.15(a)], therefore this mode is effectively triggered by the driver. The other modes have pulsation $\omega(k_j)$, being $j > 1$, much different with respect to ω_D (e.g. $\omega(k_2) \simeq 1.60$), therefore they do not fall in the accessible ω window for being excited.

On the other hand, in the off-dispersion (SIM B) case, the driver is not perfectly resonant with any Langmuir mode [see Fig. 3.15(b)]. Therefore the triggering of the $k = k_1$ is less powerful than in the SIM A case because, despite $\omega(k_1)$ falls in a region where $|\eta(\omega)|$ is weak but not exactly null, the

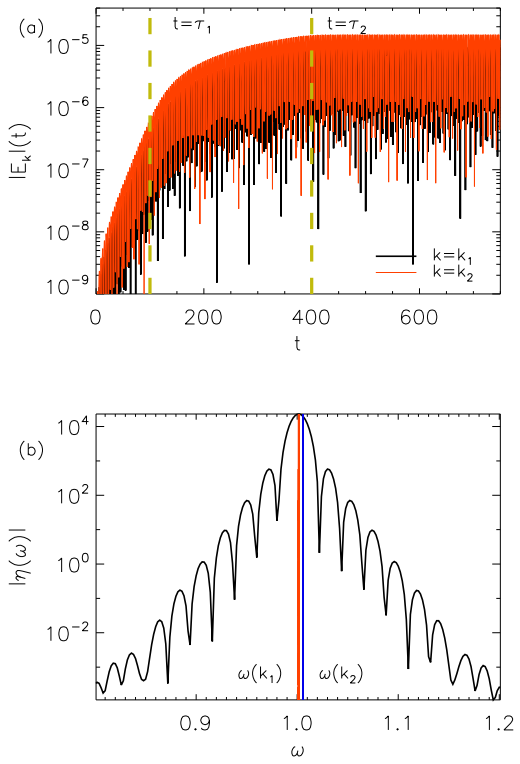

Figure 3.16: (Color online) (a) Time evolution of $|E_k|(t)$ for $k = k_1$ (black line) and $k = k_2$ (red line) relative to SIM C. The two yellow vertical lines indicate the time instants at which the driver is turned on $t = \tau_1$ and off $t = \tau_2$. (b) Absolute value of $\eta(\omega)$ for the same simulation. The red curves indicate the "proper" Langmuir frequencies $\omega(k_1)$ and $\omega(k_2)$.

fundamental wavenumber receives a small amount of energy by the driver.

We also show the results of the third simulation (SIM C), where the plasma length is much bigger compared to SIM A and SIM B and $\omega(k_1) = \omega_D$. Fig. 3.16 (a) reports the temporal evolution of the first two electric field Fourier components $|E_k|(t)$ in black ($k = k_1$) and red ($k = k_2$) solid line. In contrast with previous cases [see Fig. 3.13 and Fig. 3.14(a)], here the second Fourier component, as well as other components not explicitly shown in Fig. 3.16(a), are also excited. This happens because wavenumbers are smaller and closer compared to previous cases, therefore many Langmuir modes [See Fig. 3.16(b) which displays $\omega(k_1)$ and $\omega(k_2)$ respectively in red and blue lines]

are resonant with the driver. These modes are moreover almost undamped because their wavenumbers are small, therefore, when the driver is turned off, $|E_k|(t)$ is almost flat.

The three simulations described above let us understand that the localized driver selects - through the adiabatic temporal function $g(t)$ - a frequency window centered around ω_D, whose width is comparable with $1/\Delta\tau$ and where the energy is non-uniformly pumped. The spatial localizing function

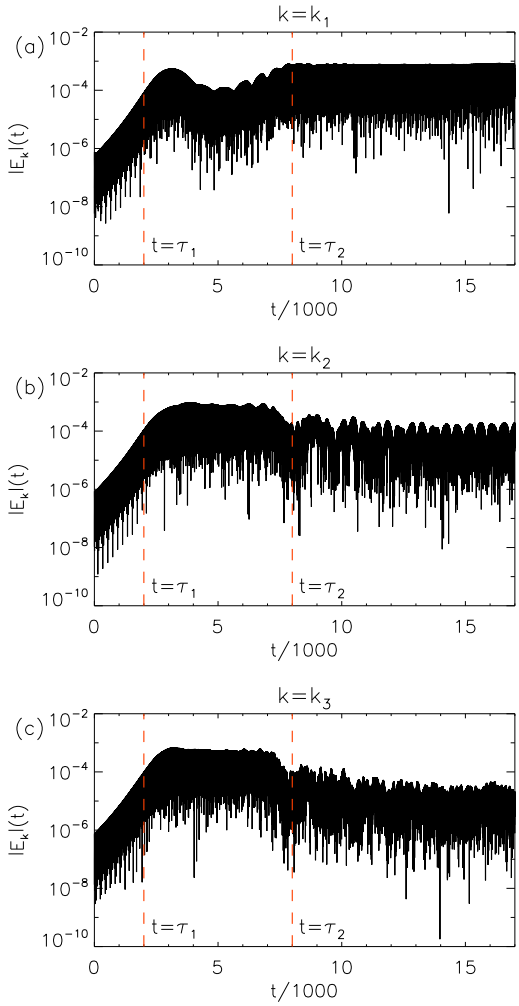

Figure 3.17: (Color online) Time evolution of $|E_k|(t)$: $k = k_1$ (a), $k = k_2$ (b) and $k = k_3$ (c) for the EAWs simulation. In each panel the red dashed lines indicate the temporal instants at which the driver is turned on $t = \tau_1$ and off $t = \tau_2$.

$h(x)$ produces instead the excitation of several wavenumbers. If any Langmuir mode frequency $\omega(k)$, being k one of the discrete wavenumbers that the driver can excite, is resonant with the driving frequency ω_D, the mode is definitively triggered.

3.2.3 Electron-acoustic waves

Here we move to the more complex scenario of EAWs. Indeed, compared to the Langmuir waves case, we show that, since the dispersion relation is of the acoustic type, nonlinear couplings can easily occur and several harmonics are generated along the dispersion relation. Since the driver is strong enough to trigger nonlinear waves (i.e. to modify the VDF), secondary beam-like instabilities are also generated. Moreover, we investigate both the case of collisionless and weakly collisional plasmas.

Collisionless case

Here we analyze the collisionless case by focusing on a simulation where the driver pulsation is $\omega_D = 0.455$ and $L = 20$. The first wavenumber $k_1 = k_0 = 2\pi/L$ (being $L = 20$ the plasma length) corresponds to a on-dispersion EAWs ($\omega_D/k_1 = v_\phi^{EAW} = 1.45$). Moreover, the driver is turned

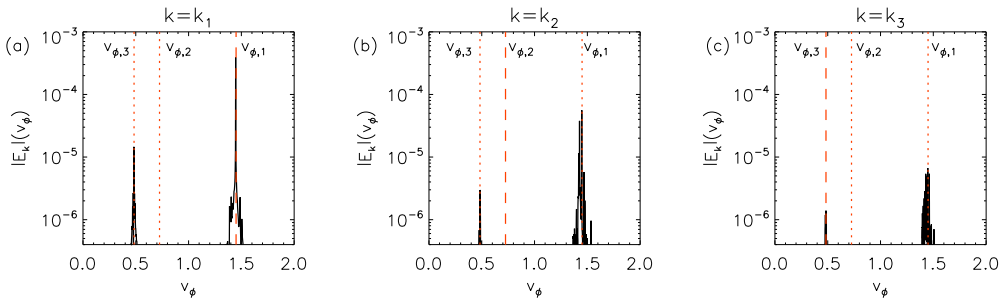

Figure 3.18: (Color online) Oscillation peaks of the first three Fourier components of the electric field given by the profile of $|E_k(v_\phi = \omega/k)|$ as a function of the phase speed $v_\phi = \omega/k$: $k = k_1$ (a), $k = k_2$ (b) and $k = k_3$ (c). The temporal Fourier transform has been performed in the temporal range after that the driver has been set off. Red dashed lines indicate the first three phase speeds which are triggered by the driver.

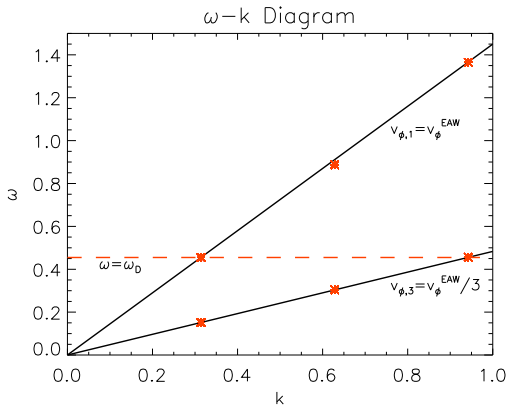

Figure 3.19: (Color online) Oscillation peaks, as showed in Fig. 3.18(a)–(d), of the first three Fourier components of the electric field represented in the k–ω plane through single points. The two black lines displays the line with phase speed $v_{\phi,1} = v^{EAW}$ and $v_{\phi,3} = v^{EAW}/3$, while the red dashed horizontal line shows the driver pulsation $\omega = \omega_D$.

on for $\Delta\tau = 5\tau_{tr}$, being $\tau_{tr} = 2\pi/\sqrt{E_k k}$ the nonlinear trapping time, while $n_g = 10$. The driver amplitude is $E_D = 5 \times 10^{-2}$.

Figures 3.17 (a)–(c) show the temporal evolution of $|E_k|(t)$ being $k = k_1$ (a), $k = k_2$ (b) and $k = k_3$ (c). In each panel of Fig. 3.17, $|E_k|(t)$ rises up for the driver effect, which is turned on between the two red vertical dashed lines $t = \tau_1$ and $t = \tau_2$, and, when the driver is turned off, many electric field spectral components survive.

To understand how the plasma reacts to the driver field, we evaluated the frequency oscillation peaks of E_k for a given k and in the range when the driver is turned off ($t > \tau_2$). Figures 3.18 (a)–(c) show $|E_{k_j}|(v_{\phi,j})$ for $j = 1$ (a), $j = 2$ (b) and $j = 3$ (c) as a function of $v_{\phi,j} = \omega/k_j$. Red vertical lines in Figs. 3.18 represent the first three phase speeds which are triggered by the driver. Indeed, since the driver pulsates at ω_D and excites several wavenumbers, several velocity values are excited: $v_{\phi,j} = v_{\phi,D}/j$, being $v_{\phi,D} = \omega_D/k$. In each panel two peaks located at $v_\phi^{EAW} = v_{\phi,1}$ and $v_{\phi,3} = v_\phi^{EAW}/3$ are recovered, therefore two straight lines with phase speeds v_ϕ^{EAW} and $v_\phi^{EAW}/3$ are populated in the k–ω plane, shown in Fig. 3.19.

It is interesting to point out how the final configuration in the k–ω plane,

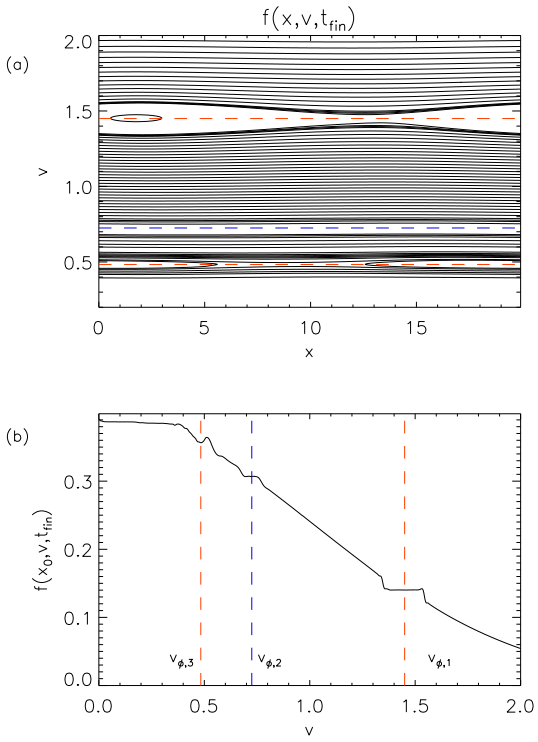

Figure 3.20: (Color online) Panel (a) show the contour plot of the distribution function at the final time $t = t_{fin} = 17000$ $f(x, v, t = t_{fin})$ in the velocity range $v = [0, 2]$ while the panel (b) displays a spatial cut of the distribution function $f(x = x_0, v, t = t_{fin})$ as a function of v. In both panels the red dashed lines indicate the phase speed $v_{\phi,1}$ and $v_{\phi,3}$ - which correspond to oscillation peaks in the electric field - while the blue line shows the phase speed $v_{\phi,2}$ - which is related to a plateau due to the driver but not yet present in the oscillation peaks of the electric field.

shown in Fig. 3.19, is generated. For this reason, we performed the analysis based on $E_k(\omega)$ at different simulation stages. At the beginning, each spatial component oscillates with the driver (along the red dashed line in Fig. 3.19). Then, while the driver is still turned on, the straight line of peaks at v_ϕ^{EAW} is generated. This process can be interpreted as a weakly nonlinear coupling (or secondary harmonics generation) occurring along the EAW branch [191]. Finally, when the driver is turned off, the secondary peaks line at $v_\phi^{EAW}/3$ appears.

The dynamics is extremely complex and, in general, the electric field does

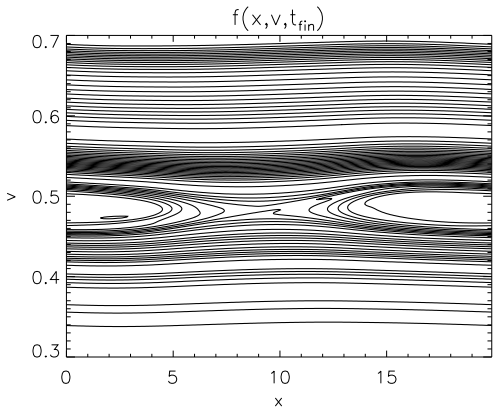

Figure 3.21: (Color online) Zoom of the distribution function contour plot $f(x, v, t = t_{fin})$ in the velocity region $v = [0.3, 0.7]$.

not oscillate just at the EAW phase speed but it exhibits several oscillation peaks. To figure out how the driver and the presence of these peaks model the distribution function in phase space, we show the contour plot of the distribution function $f(x, v, t = t_{fin})$ in the velocity region $v = [0.2, 2]$ in Fig. 3.20 (a), while Fig. 3.20 (b) displays $f(x = x_0, v, t = t_{fin})$ as a function of v being $x_0 = L/4$ and $t_{fin} = 17000$. Red dashed lines in Figs. 3.20 (a)–(b) indicate $v = v_\phi^{EAW}$ and $v = v_\phi^{EAW}/3$, while the dashed blue line shows $v = v_\phi^{EAW}/2$.

The distribution function exhibits the expected EAW BGK-hole, localized at the correct EAW phase velocity, whose width is in accordance with the theoretical expectation [192]. Therefore, as in previous works [144, 185], our driver correctly triggers EAWs. However, other structures are also generated at lower velocities which are not recovered in previous simulation studies, where the usual non-localized has been employed. A flat plateau, which resembles the "off-dispersion" like plateau obtained in Ref. [144, 185], is observed at $v_\phi^{EAW}/2$. Moreover, a large flat top profile is recovered around $v = 0$ whose width is about $\Delta v_{top} = 0.4$. This could be due to the fact that, at small velocities, the driver thickens many excitable phase speeds ($v_\phi \propto 1/k$) and the presence of many phase speeds concentrated in the same phase space region (i.e. many plateaus overlap in this region) may cause a flattening process of the VDF. Furthermore a small BGK-like vortex is localized at

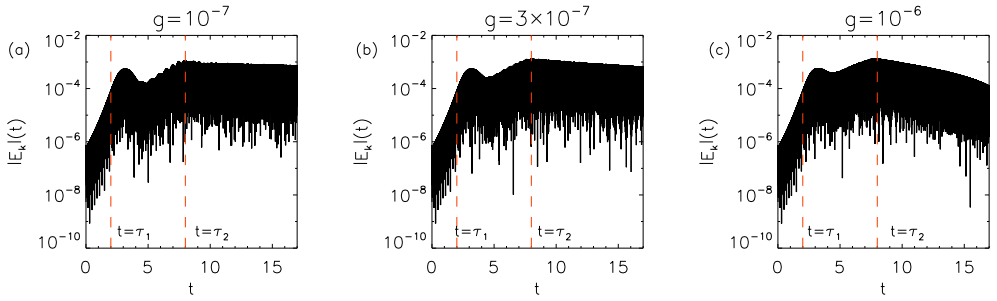

Figure 3.22: (Color online) Time evolution of $|E_k|(t)$, being $k = k_1$, for $g = 10^{-7}$ (a), $g = 3 \times 10^{-7}$ (b) and $g = 10^{-6}$ (c). In each panel the red dashed lines indicate the temporal instants at which the driver is turned on $t = \tau_1$ and off $t = \tau_2$.

$v = v_\phi^{EAW}/3$ (See the zoom of the VDF around $v = v_\phi^{EAW}/3$ showed in Fig. 3.21). Phase space structures showed in Figs. 3.20 are significantly different. The structures connected with electric field oscillations ($v = v_\phi^{EAW}$, $v_\phi^{EAW}/3$) show a BGK-like structure, while the ones due to the driver which instead does not generate a plasma response are flat and homogeneous ($v = v_\phi^{EAW}/2$).

The novel feature of our simulations concerns the presence of an unexpected, secondary, straight line of frequency oscillation peaks in the k–ω plane with phase speed $v_\phi = v_\phi^{EAW}/3$. These fluctuations, which are recovered after that the driver is turned off and are related to a small BGK-like structure in phase space, could be generated by the driver through a beam-like instability. Indeed, the VDF exhibits a a small bump around $v = v_\phi^{EAW}/3 \simeq 0.5$ due to the driver nonlinearity even before the formation of the BGK-like structure at $v_\phi^{EAW}/3$. We suggest that this small bump may generate a beam-like instability, which gives rise in the nonlinear regime to a BGK-like vortex in the distribution function. This bump is present only at $v = v_\phi^{EAW}/3$, therefore the beam-like instability mechanism due to the bump could be in accordance with the observation that suggests the presence of a secondary oscillation peaks series only for $v_\phi = v_\phi^{EAW}/3$.

Collisional case

In order to figure out if, in a weakly collisional plasma, the secondary wave branch survives or is dissipated by collisional effects, here we analyze some

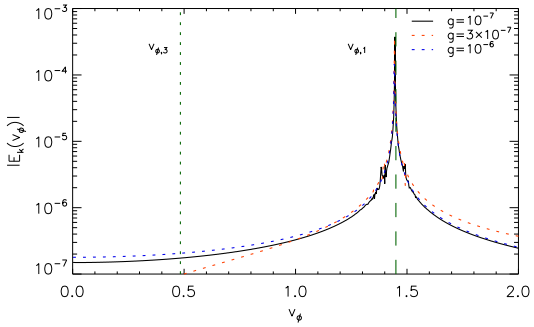

Figure 3.23: (Color online) Frequency oscillation peaks of $|E_k|(t)$, being $k = k_1$, for $g = 10^{-7}$ (black), $g = 3 \times 10^{-7}$ (red) and $g = 10^{-6}$ (blue) represented as a function of the phase speed v_ϕ. The green dashed line displays the EAWs phase speed $v_{\phi,1} = v_\phi^{EAW}$ while the greem dotted line shows the phase speed $v_{\phi,3} = v_\phi^{EAW}/3$.

collisional simulations, where collisions are modeled through the Dougherty operator [See Eq. (3.17) in Sec. 3.2.1]. We show that these secondary fluctuations are not recovered when a small collisionality is introduced, while the EAWs are damped in time. This last feature has been also observed in laboratory experiments [50, 182] and it is qualitatively similar to the Zakharov and Karpman (ZK) collisional damping predicted in Ref. [193]. The values of collisionality considered are in the range $g = [10^{-7}, 10^{-6}]$, which corresponds to realistic situations in a Penning-Malmberg apparatus.

Figures 3.22 (a)–(c) show the temporal evolution of $|E_k|(t)$ ($k = k_1$), for the cases $g = 10^{-7}$ (a), $g = 3 \times 10^{-7}$ (b) and $g = 10^{-6}$ (c). Red lines indicate the time instants when the driver has been turned on (τ_1) and off (τ_2). For $\tau_1 < t < \tau_2$, the evolution in the three cases is quite similar [compare also with Fig. 3.17 (a)]. On the other hand, for $t > \tau_2$, $|E_{k_1}|(t)$ exhibits an exponential damping, with damping rate proportional to the collisional frequency ν_0 and other components (not shown here) display the same qualitative behavior of $|E_{k_1}|(t)$. Damping rates for the cases $g = 10^{-7}$, $g = 3 \times 10^{-7}$ and $g = 10^{-6}$ are respectively $\gamma_C = -2.75 \times 10^{-5}$, $\gamma_C = -7.24 \times 10^{-4}$ and $\gamma_C = -2.27 \times 10^{-4}$. These results systematically differs by the ZK prediction of collisional damping by a factor about $2 \div 3$. However, ZK results have been obtained by assuming that i) the VDF differs from the Maxwellian *only* in the resonance region and ii) the phase speed is much

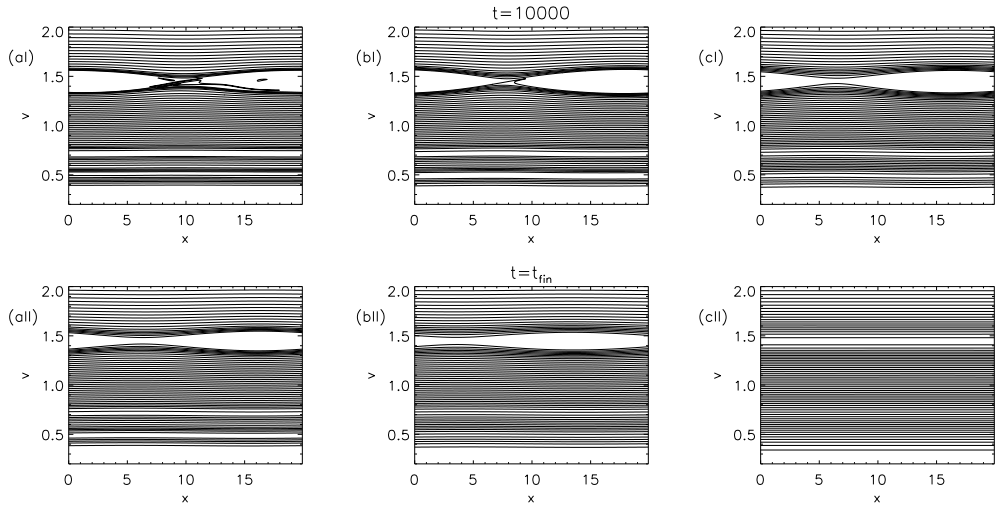

Figure 3.24: (Color online) Left, center and right columns display respectively the contour plots of the distribution function $f(x, v, t)$ for the cases $g = 10^{-7}$ (a), $g = 3 \times 10^{-7}$ (b) and $g = 10^{-6}$ (c) at two time instant $t = 10000$ (top) and at the time instant $t = t_{fin} = 17000$ (bottom).

bigger than the thermal speed and both conditions are not satisfied in our simulations; this fact may explain the quantitative discrepancy between the observed damping and the ZK prediction.

To figure out whether the secondary frequency peaks occur also in the collisional cases, we evaluated $E_k(v_\phi)$ for each case showed in Figs. 3.22(a)–(c) in the time window when the driver is turned off. Figure 3.23 shows $|E_k(v_\phi)|$ as a function of the phase speed $v_\phi = \omega/k$ for the cases $g = 10^{-7}$ (black), $g = 3\times10^{-7}$ (red) and $g = 10^{-6}$ (blue). In each case $|E_k(v_\phi)|$ exhibits a well-defined single peak around the proper EAWs phase speed $v_{\phi,1} = v_\phi^{EAW}$ [green dashed lines in Fig. 3.23]; while the second peak at $v_{\phi,3} = v_\phi^{EAW}/3$ [green dotted lines in Fig. 3.23] is not present. Other spatial wavenumbers (not shown here) exhibit the same behavior.

This characteristic is corroborated through the analysis of the distribution function in phase space. The top panels of Fig. 3.24 display the contour plots of the distribution function $f(x, v, t = 10000)$ in the velocity space region $v = [0.2, 2]$ for the cases $g = 10^{-7}$ (aI), $g = 3 \times 10^{-7}$ (bI) and $g = 10^{-6}$ (cI), while the bottom panels of Fig. 3.24 indicate $f(x, v, t = t_{fin})$, being

$t_{fin} = 17000$ for the cases $g = 10^{-7}$ (aII), $g = 3 \times 10^{-7}$ (bII) and $g = 10^{-6}$ (cII). By comparing the final stages of the collisionless and collisional simulations [compare Figs. 3.24 (aII)–(cII) with Fig. 3.20 (a)], it is easy to establish that the collisional case do not show the small BGK-like structure at $v = v_\phi^{EAW}/3$. Effectively, in correspondence of the small BGK-like structure in Fig. 3.20(a)], in the collisional cases only a small flat and homogeneous area is present, this indicating that collisions prevent the formation of the secondary peaks of oscillations. Furthermore, comparing panels (I) and (II) of Fig. 3.24, one notices that EAW holes tend to be smoothed out by collisional effects, bigger the collisional frequency faster the smoothing due to collisions.

3.2.4 Summary

In this section, we focused on the wave launching process which is commonly adopted to trigger electrostatic fluctuations in laboratory plasmas. This process, which is based on a localized external driver which triggers plasma waves, has been here described in detail by means of Eulerian kinetic simulations. First, by focusing on the triggering of linear Langmuir waves, the basic resonance wave launching mechanism has been analyzed. It is found that the driver non-uniformly pumps energy in a frequency window centered around its pulsation, while, in principle, several wavenumbers can be excited.

Then, we analyzed the case of EAWs. Beyond the excitation of EAWs, a new branch of small amplitude, acoustic-type, nonlinear waves, whose phase speed is $v_\phi = v_\phi^{EAW}/3 \simeq 0.5$, is recovered. These fluctuations may be generated as an effect of a beam-like instability due to the presence of a small bump in the core of the distribution function, generated by the driver nonlinearity. The existence of this secondary waves, in a weakly collisional plasma has been discussed. Also for small values of collisionality - comparable with the collisionality of realistic laboratory apparatus, these fluctuations are suddenly dissipated. The main EAW branch suffers instead an exponential damping, similar to the one observed in experiments.

We remark that our work has two main interesting points. Firstly, since the driver excites several phase speeds, additional wave branches can be ex-

cited. This effect is intimately related to the driver nonlinearity. When the driver acts for enough time or its amplitude is sufficiently big, nonlinear effects generate non-Maxwellian features in the particle VDF. Once plateaus or bumps are generated in the distribution function, other branches of fluctuations can be excited according to Refs. [142, 194]. Secondly, collisions have an essential role into the dissipation of these secondary modes: even for small values of the collisional frequency these secondary fluctuations are not recovered. The presence of collisions in laboratory devices may be the reason why these modes have not been yet observed in laboratory plasmas.

Discussion

We summarize here the main results showed in this part of the thesis which focused on the description of collisional effects in weakly collisional plasmas.

We first showed, by modeling collisions through the fully nonlinear Landau operator, that collisionality can be significant also in a weakly collisional plasma. Indeed, strong velocity space gradients, which naturally develop in the particle distribution function as an effect of wave-particle interactions and - in general - of turbulence cascade, are dissipated much faster than other global non-Maxwellian features. These characteristic dissipation times can be much smaller than the Spitzer-Harm time. This suggests that, when the particle distribution function exhibits fine velocity space structures, collisions can be locally enhanced and could be comparable with other characteristic dynamical times.

However, as described in detail, the computational cost of the Landau operator is significantly high and, nowadays, it is not possible to perform self-consistent simulations where collisions are modeled through this operator. Therefore, simplified collisional operators are routinely adopted. Here, we initially modeled collisions through the Dougherty operator in the full three-dimensional velocity space. We recovered a quite good agreement between the Landau and the Dougherty operators in the relaxation of spatially homogeneous force-free plasmas. Hence, we performed self-consistent electrostatic simulations of a plasma composed of kinetic electrons and immobile protons, in a nonlinear regime and in the case of weak collisionality. By focusing on the onset of the bump-on-tail instability and on the propagation of KEEN waves, we described the competitive role of kinetic processes, which tend to modify the particle VDF, and collisions, which instead tend to restore

the thermal equilibrium.

Then, we restricted to a reduced $1D$–$1V$ phase space where we described two different phenomena. First, we analyzed the role of collisions on the recurrence of the initial state, by showing that the artificial collisionality cannot prevent recurrence without significantly compromise the kinetic features of the solution. Moreover, we pointed out that filamentation-like phenomena, usually associated with linear fluctuations, can play a role even in nonlinear regime.

Finally, we described the method, usually adopted in laboratory plasmas devices, for exciting waves. When triggering Electron Acoustic Waves, a new branch of small amplitude, nonlinear and non-dispersive waves has been also recovered beyond the main EAWs branch. These secondary fluctuations are generated by the external, nonlinear driver and tend to be quickly dissipated when a small collisionality - comparable with the one of laboratory experiments - is considered.

Conclusions

The full comprehension of the dynamics of weakly collisional plasmas such as the solar wind is one of the intriguing challenges for the space plasmas scientific community. The solar wind is a complex, strongly turbulent medium whose dynamics involves several processes at different spatial and temporal scales. The energy is transferred along the spectrum from large, injection scales, where the dynamics is modeled within a fluid approach, towards smaller scales where a kinetic approach is needed. Although kinetic models are often collisionless, one should bear in mind that collisions may have a significant role for properly describing dissipative irreversible processes.

In this thesis we have initially examined the interplay of fluid and kinetic scales by revisiting the Moffatt & Parker problem by means of MHD, Hall MHD and hybrid kinetic numerical simulations. This problem, which concerns the interaction of counter-propagating Alfvénic wave packets, was investigated in the late Seventies in the ideal incompressible MHD case and it is considered the "building-block" scenario for triggering turbulence. Here, by extending the description to the realm of kinetic plasmas, we showed that the introduction of dispersion and kinetic physics makes the dynamics much more complex with respect to the MHD case. Indeed, strong turbulence signatures coexist with a waves-like activity and it is difficult to determine if wave packets attain a full separation after their interaction, as predicted by the Moffatt & Parker theory.

Our simulations concerning the Moffatt & Parker problem suggest that, once kinetic scales are reached, the particle distribution function is strongly affected by wave-particle resonances and kinetic turbulence and, as a natural consequence, its shape is significantly perturbed. This feature is also recov-

ered by means of other kinds of numerical simulations or through solar wind *in-situ* measurements. The presence of these velocity space distortions makes us address a fundamental question, which underlies the results showed in the second part of the thesis. Since collisional effects explicitly depend on velocity space gradients, could these fine structures locally enhance the plasma collisionality, despite it is usually considered far too weak to produce significant effects?

We reported evidences that the collisionality can be effectively enhanced also in a weakly collisional plasmas. Indeed, by modeling collisions through the fully nonlinear Landau operator and focusing on the collisional relaxation of a homogeneous force-free plasma, we showed that fine velocity structures are dissipated much faster (with characteristic times much smaller than the Spitzer-Harm time) than other global non-Maxwellian features. Therefore, when the particle distribution function exhibits strong velocity space gradients, collisions can be effectively enhanced and could be comparable with other characteristic dynamical times. The nonlinearities present in the mathematical form of the Landau operator are also important to properly compare collisional times with other dynamical times.

Performing self-consistent simulation where collisions are modeled with the Landau operator is nowadays problematic for the Landau operator computational cost. Hence, collisions are usually taken into account by means of simplified operators. We here modeled collisions through the Dougherty operator. We established a good comparison between the Landau and the Dougherty operator in the case of the collisional relaxation of a spatially homogeneous force-free plasma, this allowing to perform self-consistent collisional simulations, in the $1D$–$3V$ configuration, regarding the propagation of nonlinear electrostatic waves. Finally, restricting to the $1D$–$1V$ phase space, we analyzed two separate problems: the effects of collisions on the phenomenon of the recurrence of the initial states and the launching problem, namely the methods commonly adopted in laboratory plasmas for triggering waves.

Bibliography

[1] W.M. Elsässer, Phys. Rev. **79**, 183 (1950).

[2] S. Chandrasekhar, Proceedings of the National Academy of Sciences **42**, 273 (1956).

[3] R.S. Iroshnikov, Soviet Astron. **7**, 566 (1964).

[4] R.H. Kraichnan, Phys. Fluids **8**, 1385 (1965).

[5] H.K. Moffatt, *Field Generation in Electrically Conducting Fluids*, (Cambridge University Press, 1978).

[6] E.N. Parker, *"Cosmical magnetic fields: Their origin and their activity."*, (Oxford Univerity Press, 1979).

[7] M. Dobrowolny, A. Mangeney & P. Veltri, Phys. Rev. Lett. **45**, 144 (1980).

[8] M. Dobrowolny, A. Mangeney & P. Veltri, Solar and Interplanetary Dynamics (Springer, Netherlands, 1980).

[9] C.S. Ng & A. Bhattacharjee, The Astrophys. Journal **465**, 845 (1996).

[10] W.H. Matthaeus, G.P. Zank, C.W. Smith & S. Oughton, Phys. Rev. Lett. **82**, 3444 (1999).

[11] A. Verdini, M. Velli & E. Buchlin, The Astrophys. Journal Letters **700**, L39 (2009).

[12] R. Bruno & V. Carbone, Living Rev. Solar Phys. **10**, 1 (2013).

[13] G.G. Howes & K.D. Nielson, Phys. Plasmas **20**, 072302 (22013).

[14] O. Pezzi, T.N. Parashar, S. Servidio, F. Valentini, C.V. Vásconez, Y. Yang, F. Malara, W.H. Matthaeus & P. Veltri, The Astrophys. Journal **834**, 166 (2017).

[15] L. Turner, IEEE Transactions on Plasma Science **14**, 849 (1986).

[16] S. Galtier, J. Plasma Phys. **72**, 712 (2006).

[17] S. Servidio, W.H. Matthaeus & V. Carbone, Phys. Plasmas **15**, 042314 (2008).

[18] F. Sahraoui, S. Galtier & G. Belmont, J. Plasma Phys. **73**, 723 (2007).

[19] O. Alexandrova, V. Carbone, P. Veltri & L. Sorriso-Valvo, The Astrophys. Journal **674**, 1153 (2008).

[20] S.P. Gary, S. Saito & Y. Narita, The Astrophys. Journal **716**, 1332 (2010).

[21] E. Marsch, Living Rev. Sol. Phys. **3(1)**, 1–100 (2006).

[22] J.C. Kasper, A.J. Lazarus & S.P. Gary, Geophys. Res. Lett. **29**, 20 (2008).

[23] B.A. Maruca, J.C. Kasper & S.D. Bale, Phys. Rev. Lett. **107**, 201101 (2011).

[24] B.A. Maruca, S.D. Bale, L. Sorriso-Valvo, J.C. Kasper & M.L. Stevens, Phys. Rev. Lett. **111(24)**, 241101 (2013).

[25] J. He, L. Wang, C. Tu, E. Marsch & Q. Zong, The Astrophys. J. Lett. **800(2)**, L31 (2015).

[26] W. Daughton, V. Roytershteyn, B.J. Albright, H. Karimabadi, L. Yin & K.J. Bowers, Phys. Rev. Lett. **103(6)**, 065004 (2009).

[27] T.N. Parashar, M.A. Shay, P.A. Cassak & W.H. Matthaeus, Physics of Plasmas **16**, 032310 (2009).

[28] E. Camporeale & D. Burgess, The Astrophysical J. **730**, 114 (2011).

[29] F. Valentini, F. Califano, D. Perrone, F. Pegoraro & P. Veltri, Phys. Rev. Lett. **106(16)**, 165002 (2011).

[30] S. Servidio, F. Valentini, F. Califano & P. Veltri, Phys. Rev. Lett. **108(4)**, 045001 (2012).

[31] A. Greco, F. Valentini, S. Servidio & W.H. Matthaeus, Phys. Rev. E **86(6)**, 066405 (2012).

[32] D. Perrone, F. Valentini, S. Servidio, S. Dalena & P. Veltri, The Astrophys. J. **762**, 99 (2012).

[33] F. Valentini, S. Servidio, D. Perrone, F. Califano, W.H. Matthaeus & P. Veltri, Phys. Plasmas **21(8)**, 082307 (2014).

[34] L. Franci, A. Verdini, L. Matteini, S. Landi & P. Hellinger, The Astrophys. J. Lett. **804**, L39 (2015).

[35] S. Servidio, F. Valentini, D. Perrone, A. Greco, F. Califano, W.H. Matthaeus & P. Veltri, J. Plasma Phys. **81(1)**, 325810107 (2015).

[36] F. Valentini, D. Perrone, S. Stabile, O. Pezzi, S. Servidio, R. De Marco, ... & G. Consolini, New Journal of Physics **18(12)**, 125001 (2016).

[37] S.S. Cerri, F. Califano, F. Jenko, D. Told and F. Rincon, The Astrophysical Journal Letters **822**, L12 (2016)

[38] C.K. Birdsall & A.B. Langdon, *Plasma physics via computer simulation* (CRC Press, 2004).

[39] A. Zeiler, D. Biskamp, J.F. Drake, B.N. Rogers, M.A. Shay & M. Scholer, J. Geophys. Res. **107**, 1230 (2002).

[40] F. Valentini, P. Trávníček, F. Califano, P. Hellinger & A. Mangeney, J. Comput. Phys. **225(1)**, 753–770 (2007).

[41] D. Perrone, F. Valentini, S. Servidio, S. Dalena & P. Veltri, The Astrophys. J. **762**, 99 (2013).

[42] E. Camporeale, G.L. Delzanno, G. Lapenta and W. Daughton, Phys. Plasmas **13**, 092110 (2006).

[43] C. Tronci and E. Camporeale, Phys. Plasmas **22**, 020704 (2015).

[44] E. Camporeale, G.L. Delzanno, B.K. Bergen & J. D. Moulton, Comp. Phys. Comm. **198**, 47 (2016).

[45] S. Galtier, J. Geop. Research **113(A1)**, A01102 (2008).

[46] A.A. Schekochihin, S.C. Cowley, W. Dorland, G.W. Hammett, G.G. Howes, E. Quataert & T. Tatsuno, The Astrophys. J. Supp. Series **182**, 310 (2009).

[47] P. Goswami, T. Passot and P.L. Sulem, Phys. Plasmas **12** 102109 (2005).

[48] R. Hernandez & E. Marsch, J. Geop. Research **90(A11)**, 11062–11066 (1985).

[49] O. Pezzi, F. Valentini & P. Veltri, Phys. Rev. Lett. **116**, 145001 (2016).

[50] F. Anderegg, C.F. Driscoll, D.H.E. Dubin & T.M. O'Neil, Phys. Rev. Lett. **102**, 095001 (2009).

[51] M. Affolter, F. Anderegg, D.H.E. Dubin and C.F. Driscoll, Phys. Rev. Lett. **117**, 155001 (2016).

[52] L.D. Landau, Phys. Z. Sowjet. **10**, 154, (1936); translated in "The Transport Equation in the Case of the Coulomb Interaction", *Collected papers of L. D. Landau*, (Pergamon Press, Oxford, 1981).

[53] M.N. Rosenbluth, W.M. MacDonald & D.L. Judd, Phys. Review **107(1)**, 1 (1957).

[54] A. Lenard, Annals Physics **10.3**, 390 (1960).

[55] R. Balescu, Phys. Fluids **3.1**, 52 (1960).

[56] A.I. Akhiezer, I.A. Akhiezer, R.V. Polovin, A.G. Sitenko & K.N. Stepanov, *Plasma electrodynamics (Vol. 1)*, (Pergamon Press, Oxford, 1975).

[57] P.L. Bhatnagar, E. P. Gross & M. Krook, Phys. Rev. **94**, 511 (1954).

[58] J.P. Dougherty, Phys. Fluids **7**, 1788 (1964).

[59] J.P. Dougherty & S.R. Watson, J. Plasma Phys. **1**, 317–326 (1967).

[60] T.M. O'Neil, Phys. Fluids **11**, 2420 (1968).

[61] S. Livi and E. Marsch, Phys. Rev. A **34**, 533 (1986).

[62] O. Pezzi, F. Valentini, D. Perrone & P. Veltri, Phys. Plasmas **20**, 092111 (2013).

[63] O. Pezzi, F. Valentini, D. Perrone & P. Veltri, Phys. Plasmas **21**, 019901 (2014).

[64] O. Pezzi, F. Valentini & P. Veltri, J. Plasma Phys. **81(1)**, 305810107 (2015).

[65] M. Velli, R. Grappin & A. Mangeney, Phys. Rev. Lett **63**, 1807 (1989).

[66] S. Sridhar & P. Goldreich, The Astrophys. Journal **432**, 612 (1994).

[67] P. Goldreich & S. Sridhar, The Astrophys. Journal **438**, 763 (1995).

[68] S. Galtier, S.V. Nazarenko, A.C. Newell & A. Poucket, J. Plasma Phys. **63**, 447 (2000).

[69] K.D. Nielson, G.G. Howes & W. Dorland, Phys. Plasmas **20**, 072303 (2013).

[70] J.W. Belcher & L. Davis Jr., J. Geophys. Res. **76**, 3534 (1971).

[71] W.H. Matthaeus, G.P. Zank, S. Oughton, D.J. Mullan & P. Dmitruk, The Astrophys. J. Letters **523**, L93 (1999).

[72] S. Tomczyk, S.W. McIntosh, S.L. Keil, P.G. Judge, T. Schad, D.H. Seeley & J. Edmondson, Science **317**, 1192 (2007).

[73] S. Tomczyk & S.W. McIntosh, The Astrophys. Journal **697**, 1384 (2009).

[74] R. Bruno, R. Bavassano & U. Villante, J. Geophys. Res. **90**, 4373 (1985).

[75] D. J. McComas, L. Barraclough, H.O. Funsten, J.T. Gosling, E. Santiago-Muñoz, R.M. Skoug, B.E. Goldstein, M. Neugebauer, P. Riley & A. Balogh, J. Geophys. Res. **105**, 419 (2000).

[76] J. He, C. Tu, E. Marsch, C.H.K. Chen, L. Wang, Z. Pei, L. Zhang, C.S. Salem & S.D. Bale, The Astrophys. Journal Letters **813**, L30 (2015).

[77] J. Armstrong, J. Cordes & B. Rickett, Nature **291**, 561 (1981).

[78] G.P. Zank & W.H. Matthaeus, J. Geophys. Res. **97**, 189 (1992).

[79] J.V. Hollweg, J. Geophys. Res. **104**, 14811 (1999).

[80] S.A. Orszag, Stud. Appl Math. **50**, 293 (1971).

[81] S.A. Orszag & G.S. Patterson, Phys. Rev. Lett. **28**, 76 (1972).

[82] R.H. Kraichnan & D. Montgomery, Reports on Progress in Physics **43**, 547 (1980).

[83] S.A. Orszag, in *Fluid Dynamics: Les Houches* ed. by R. Balian and J. L. Peube (Gordon and Breach, New York, 1973), p. 237.

[84] S. Oughton, P. Dmitruk & W.H. Matthaeus, Phys. Plasmas **13**, 2306 (2006).

[85] D.J. Drake, J.W.R. Schroeder, G.G. Howes, C.A. Kletzing, F. Skiff, T.A. Carter & D.W. Auerbach, Phys. Plasmas **20**, 072901 (2013).

[86] G.G. Howes, K.D. Nielson, D.J. Drake, J.W.R. Schroeder, F. Skiff, C.A. Kletzing & T.A. Carter, Phys. Plasmas **20**, 072304 (2013).

[87] D.J. Drake, G.G. Howes, J.R. Rhudy, S.K. Terry, T.A. Carter, C.A. Kletzing, J.W.R. Schroeder & F. Skiff, Phys. Plasmas **23**, 022305 (2016).

[88] P.H. Yoon, L.F. Ziebell, R. Gaelzer & J. Pavan, Phys. Plasmas **19**, 102303 (2012).

[89] P.H. Yoon, Phys. Plasmas **22**, 082309 (2015a).

[90] P.H. Yoon, Phys. Plasmas **22**, 082310 (2015b).

[91] R. Meyrand, S. Galtier & K.H. Kiyani, Phys. Rev. Lett. **116**, 105002 (2016).

[92] A. Barnes, *Space Plasma Physics: The Study of Solar-System Plasmas* (National Academy of Sciences, Washington DC USA, 1979).

[93] Y. Narita, S.P. Gary, S. Saito, K.H. Glassmeier & U. Motschmann, Geophys. Res. Lett. **38**, L05101 (2011).

[94] W.H. Matthaeus, M. Wan, S. Servidio, A. Greco, K.T. Osman, S. Oughton & P. Dmitruk, Philosophical Transaction of the Royal Society of London **373**, 20140154 (2015).

[95] O.W. Roberts & X. Li, Astrophys. J. **802**, 1 (2015a).

[96] O.W. Roberts, X. Li & L. Jeska, Astrophys. J. **802**, 2 (2015b).

[97] C. Perschke, Y. Narita, U. Motschmann & K.H. Glessmeier, Phys. Rev. Lett. **116**, 125101 (2016).

[98] T.N. Parashar, C. Salem, R.T. Wicks, H. Karimabadi, S.P. Gary, & W.H. Matthaeus, J. Plasma Phys. **81**, 905810513 (2015).

[99] O. Pezzi, T.N. Parashar, S. Servidio, F. Valentini, C.V. Vásconez, Y. Yang, F. Malara, W.H. Matthaeus & P. Veltri, J. Plasma Phys, *accepted*.

[100] G.G. Howes, J. Plasma Phys. **81**, 325810203 (2015).

[101] T.N. Parashar, W.H. Matthaeus, M.A. Shay & M. Wan, The Astrophys. J. **811**, 112 (2015).

[102] T.N. Parashar, S. Oughton, W.H. Matthaeus & M. Wan, The Astrophys. J. **824**, 44 (2016).

[103] H. Karimabadi, V. Roytershteyn, W. Daughton & Y. Liu, Space Sc. Rev. **178**, 307 (2013).

[104] M. Wan, W.H. Matthaeus, V. Roytershteyn, H. Karimabadi, T. Parashar, P. Wu & M. Shay, Phys. Rev. Lett. **114**, 175002 (2015).

[105] T.C. Li, G.G. Howes, K.G. Klein & J.M. TenBarge, The Astrophys. J. Lett. **832**, L24 (2016).

[106] C.Vásconez, F. Pucci, F. Valentini, S. Servidio, W.H. Matthaeus, & F. Malara, Astrophys. J. **815**, 7 (2015).

[107] F. Pucci, C.L. Vásconez, O. Pezzi, S. Servidio, F. Valentini, W.H. Matthaeus & F. Malara, J. Geophys. Res. **121**, 1024 (2016).

[108] J.M. Dawson, Rev. Mod. Phys. **55**, 403 (1983).

[109] K. Malakit, P.A. Cassak, M.A. Shay & J.F. Drake, Geophys. Res. Lett. **36**, L07107 (2009).

[110] D. Del Sarto, F. Pegoraro, & F. Califano, Phys. Rev. E **93**, 053203 (2016).

[111] T.N. Parashar & W.H. Matthaeus, The Astrophys. J. **832**, 57 (2016).

[112] W.H. Matthaeus & S.L. Lamkin, Phys. Fluids **29**, 2513 (1986).

[113] W.H. Matthaeus & M.L. Goldstein, J. Geophys. Res. **87**, 6011 (1982).

[114] O. Pezzi, F. Malara, S. Servidio, F. Valentini and P. Veltri, *in preparation.*

[115] N. Aunai, M. Hesse & M. Kuznetsova, Phys. Plasmas **20**, 092903 (2013).

[116] M. Swisdak, Geophys. Res. Lett. **43**, 43 (2016).

[117] E. Marsch, K.H. Muhlhauser, R. Schwenn, H. Rosenbauer, W. Pilipp & F.M. Neubauer, J. Geophys. Res. **87**, 52 (1982).

[118] B.E. Goldstein, M. Neugebauer, J.L. Phillips, S. Bame, J.T. Gosling, D. McComas, Y.M. Wang, N.R. Sheeley & S.T. Suess, Astron. Astrophys. **316**, 296 (1996).

[119] R. Marino, L. Sorriso-Valvo, V. Carbone, A. Noullez, R. Bruno & B. Bavassano, The Astrophys. J. Lett. **667**, L71 (2008).

[120] S.R. Cranmer, W.H. Matthaeus, B.A. Breech & J.C. Kasper, The Astrophys. J. **702**, 1604 (2009).

[121] L Sorriso-Valvo, R. Marino, V. Carbone, A. Noullez, F. Lepreti, P. Veltri, R. Bruno, B. Bavassano & E. Pietropaolo, Phys. Rev. Lett. **99**, 115001 (2007).

[122] F. Sahraoui, M.E. Goldstein, P. Robert & Y.V. Khotyaintsev, Phys. Rev. Lett. **102**, 231102 (2009).

[123] U. Frisch, *Turbulence: the legacy of A.N. Kolmogorov*, (Cambridge University Press, 1995).

[124] L. Spitzer Jr, *Physics of Fully Ionized Gases*, (Interscience Publishers, New York, NY, 1956).

[125] M. Lesur, P.H. Diamond & Y. Kosuga, Phys. Plasmas **21**, 112307 (2014).

[126] F. Filbet & L. Pareschi, J. Comp. Phys. **179(1)**, 1–26 (2002).

[127] A.V. Bobylev & I.F. Potapenko, J. Comp. Phys. **246**, 123–144 (2013).

[128] D.F. Escande, Y. Elskens & F. Doveil, J. Plasma Phys, **81(1)**, 305810101 (2015).

[129] O. Pezzi, F. Valentini & P. Veltri, Phys. Plasmas **22**, 042112 (2015).

[130] A. Banón Navarro, B. Teaca, D. Told, D. Groselj, P. Crandall & F. Jenko, Phys. Rev. Lett. **117**, 245101 (2016).

[131] S.F. Tigik, L.F. Ziebell, P.H. Yoon & E.P. Kontar, Astronomy & Astrophysics **586**, A19 (2016).

[132] C. Villani, *A review of mathematical topics in collisional kinetic theory* **1**, 71–305 (2002).

[133] A. Vaivads, A. Retinó, J. Soucek, Y.V. Khotyaintsev, F. Valentini, C.P. Escoubet *et al.*, J. Plasma Physics **82**, 905820501 (2016).

[134] M. W. Anderson and T.M O'Neil, Phys. Plasmas **14**, 052103 (2007).

[135] M. W. Anderson and T.M O'Neil, Phys. Plasmas **14**, 112110 (2007).

[136] O. Pezzi, F. Valentini & P. Veltri, Euro. Phys. Journal D **68**, 128 (2014).

[137] T.W. Johnston, Y. Tyshetskiy, A. Ghizzo & P. Bertrand, Phys. Plasmas **16(4)**, 042105 (2009).

[138] B. Afeyan, W. H. Savchengo, T. W. Johnston, A. Ghizzo & P. Bertrand, in *Proc. 3rd Int. Conf. on Inertial Fusion Sciences and Applications M034 (Monterey, CA, 2003)*, edited by B. Hammel *et al.* (LaGrange Park, IL: American Nuclear Society) p 213 (2004).

[139] A. Lenard & I.B. Bernstein, Phys. Rev. **112**, 1456 (1958).

[140] O. Pezzi, J. Plasma Phys. *under review.*

[141] L.J. Curtis, H.G. Berry & J. Bromander, Physica Scripta **2(4-5)**, 216 (1970).

[142] J.P. Holloway & J.J. Dorning, Phys. Rev. A **44(6)**, 3856 (1991).

[143] F. Valentini, T.M. O'Neil and D.H.E. Dubin, Phys. Plasmas **13**, 052303 (2006).

[144] F. Valentini, D. Perrone, F. Califano, F. Pegoraro, P. Veltri, P. J. Morrison, and T. M. O'Neil, Phys. Plasmas **19**, 092103 (2012).

[145] A.A. Kabantsev, F. Valentini and C.F. Driscoll, Non-Neutral Plasma Physics VI **862**, 13–18 (2006).

[146] I.B. Bernstein, J.M. Greene & M.D. Kruskal, Phys. Rev. **108(3)**, 546 (1957).

[147] W.H. Matthaeus, S. Oughton, K.T. Osman, S. Servidio, M. Wan, S.P. Gary, M.A. Shay, F. Valentini, V. Roytershteyn & H. Karimabadi, The Astrophys. J. **790**, 155 (2014).

[148] S.P. Gary, *Theory of space plasma microinstabilities*, (New York, Cambridge Univ. Press, 1993).

[149] F.L. Hinton & R.D. Hazeltine, Rev. Mod. Phys. **48**, 239 (1976).

[150] R. Peyret & T.D. Taylor, *Computational Methods for Fluid Flow*, (Springer, New York, 1983).

[151] V.I. Kogan, *Plasma Physics and the Problem of Controlled Thermonuclear Reactions* **1**, 153 (1961).

[152] C.F. Driscoll, F. Anderegg, D.H.E. Dubin & T.M. O'Neil, *New Developments in Nonlinear Plasma Physics, B. Eliasson and P.K. Shukla, eds., AIP Conf. Proc.* **1188**, 272–279 (2009).

[153] A. Mangeney, F. Califano, C. Cavazzoni, P. Travnicek, J. Comput. Phys. **179**, 495 (2002).

[154] F. Valentini, P. Veltri & A. Mangeney, J. Comput. Phys. **210**, 730 (2005).

[155] A. Simon & M. N. Rosenbluth, Phys. Fluids **19**, 1567 (1976).

[156] N.A. Krall & A.W. Trivelpiece, *Principles of Plasma Physics*, (San Francisco Press, San Francisco, CA, 1986).

[157] T.M. O'Neil, Phys. Fluids **8**, 2255 (1965).

[158] F. Valentini, V. Carbone, P. Veltri & A. Mangeney, Phys. Rev. E **71**, 017402 (2005).

[159] Y. Cheng, I. M. Gamba & P. J. Morrison, J. Comput. Phys. **56.2**, 319–349 (2013).

[160] L.D. Landau, J. Phys. U.S.S.R **10**, 25 (1946).

[161] O. Pezzi, E. Camporeale & F. Valentini, Phys. Plasmas **23**, 022013 (2016).

[162] O. Pezzi, T.M. O'Neil and F. Valentini, *in preparation.*

[163] C. Cheng & G. Knorr, J. Comput. Phys. **22.3**, 330–351 (1976).

[164] N.J. Zabusky & M.D. Kruskal, Phys. Rev. Lett. **15.6**, 240–243 (1965).

[165] L. Galeotti & F. Califano, Phys. Rev. Lett **95**, 015002 (2005).

[166] F. Califano, L. Galeotti & F. Pegoraro, Phys. Plasmas **13**, 082102 (2006).

[167] G. Belmont, F. Mottez, T. Chust and S. Hess, Phys. Plasmas **15(5)**, 052310 (2008).

[168] T. Chust, G. Belmont, F. Mottez and S. Hess, Phys. Plasmas **16(9)**, 092104 (2009).

[169] E. Siminos, D. Benisti & L. Gremillet, Phys. Rev. E **83.5**, 056402 (2011).

[170] J.D. Crawford and P.D. Hislop, Annals of Physics **189.2**, 265–317 (1989).

[171] J.W. Schumer & J.P. Holloway, J. Comput. Phys **144**, 626–661 (1998).

[172] C. Black, K. Germaschewksi, A. Bhattacharjee & C.S. Ng, Phys. Plasmas **20.1**, 012125 (2013).

[173] L. Gibelli and B. D. Shizgal, J. Comput. Phys. **219**, 477–488 (2006).

[174] M. L. da Silva Vilelas, *Msc Thesis, Instituto Superior Técnico*, Lisbon (2013).

[175] N.G. Van Kampen, Physica **21.6**, 949–963 (1955).

[176] K.M. Case, Annals Physics **7**, 349–364 (1959).

[177] C.S. Ng, A. Bhattacharjee & F. Skiff, Phys. Rev. Lett. **83.10**, 1974 (1999).

[178] C.S. Ng, A. Bhattacharjee & F. Skiff, Phys. Rev. Lett. **92.6** 065002 (2004).

[179] J. Fajans, E. Gilson and L. Friedland, Phys. Rev. Lett **82**, 4444 (1999).

[180] J. Fajans, E. Gilson and L. Friedland, Phys. Plasmas **6**, 4497 (1999).

[181] W. Bertsche, J. Fajans and L. Friedland, Phys. Rev. Lett. **91**, 265003 (2003).

[182] F. Anderegg, C.F. Driscoll, D.H.E. Dubin, T.M. O'Neil & F. Valentini, Phys. Plasmas **16**, 055705 (2009).

[183] F. Valentini, T.M. O'Neil and D.H.E. Dubin, Nonlinear Sci. and Num. Simulations **13**, 215–220 (2008).

[184] H. Schamel, Phys. Plasmas **20**, 034701 (2013).

[185] F. Valentini, D. Perrone, F. Califano, F. Pegoraro, P. Veltri, P.J. Morrison and T. M. O'Neil, Phys. Plasmas **20**, 034702 (2013).

[186] I. Barth, L. Friedland, E. Sarid and A.G. Shagalov, Phys. Rev. Lett, **103**, 155001 (2009).

[187] L. Friedland and A.G. Shagalov, Phys. Rev. E **89**, 053103 (2014).

[188] F. Valentini, F. Califano, D. Perrone, F. Pegoraro and P. Veltri, Plasma Phys. Control. Fusion **53**, 105017 (2011).

[189] F. Valentini, A. Vecchio, S. Donato, V. Carbone, C. Briand, J. Bougeret and P. Veltri, The Astrophys. Journal Letter **788**, L16 (2014).

[190] A. Vecchio, F. Valentini, S. Donato, V. Carbone, C. Briand, J. Bougeret and P. Veltri, J. Geop. Res. **119(9)**, 7012–7024 (2014).

[191] R. Z. Sagdeev and A. A. Galeev, *Nonlinear plasma theory*, (Benjamin, New York, 1969).

[192] L. De Meio and P.F. Zweifel, Phys. Fluids B **2**, 1252 (1990).

[193] V.E. Zakharov & V.I. Karpman, Sov. Phys. Jetp **16**, 351 (1963).

[194] K. Pommois, F. Valentini, O. Pezzi and P. Veltri, Physics of Plasmas **24**, 012105 (2017).

Scientific contributions

Publications in referred journals

- **O. Pezzi**, F. Malara, S. Servidio, F. Valentini, T.N. Parashar, W.H. Matthaeus and P. Veltri.
  Turbulence in Alfvénic packets collision, submitted to "Physical Review E".

- **O. Pezzi**.
  Solar wind collisional heating, Journal of Plasma Physics **83**, 555830301 (2017).
  Invited Paper for the Journal of Plasma Physics Special Issue in honor of V.C.A. Ferraro.
  http://dx.doi.org/10.1017/S0022377817000368

- **O. Pezzi**, T.N. Parashar, S. Servidio, F. Valentini, C.L. Vasconez, Y. Yang, F. Malara, W.H. Matthaeus and P. Veltri.
  Colliding Alfvénic wave packets in MHD, Hall and kinetic simulations, Journal of Plasma Physics **83**, 905830105 (2017).
  http://dx.doi.org/10.1017/S0022377817000113

- K. Pommois, F. Valentini, **O. Pezzi** and P. Veltri.
  Slow electrostatic fluctuations generated by beam-plasma interaction, Physics of Plasmas **24**, 012105 (2017).
  http://dx.doi.org/10.1063/1.4973829

- **O. Pezzi**, T.N. Parashar, S. Servidio, F. Valentini, C.L. Vasconez, Y. Yang, F. Malara, W.H. Matthaeus and P. Veltri.

Revisiting a classic: the Parker-Moffatt problem, The Astrophysical Journal **834**, 166 (2017).
http://dx.doi.org/10.3847/1538-4357/834/2/166

- F. Valentini, D. Perrone, S. Stabile, **O. Pezzi**, S. Servidio, R. De Marco, M. Marcucci, R. Bruno, B. Lavraud, J. De Keyser, G. Consolini, D. Brienza, L. Sorriso-Valvo, A. Retinó, A. Vaivads, M. Salatti and P. Veltri.
Differential kinetic dynamics and heating of ions in the turbulent solar wind, New Journal of Physics **18**, 125001 (2016).
http://dx.doi.org/10.1088/1367-2630/18/12/125001

- F. Valentini, C.L. Vasconez, **O. Pezzi**, S. Servidio, F. Malara and F. Pucci.
Transition to kinetic turbulence at proton scales driven by large amplitude Kinetic Alfvén fluctuations, Astronomy and Astrophysics **599**, A8 (2017).
http://dx.doi.org/10.1051/0004-6361/201629240

- **O. Pezzi**, F. Valentini and P. Veltri.
Collisional relaxation of fine velocity structures in plasmas, Physical Review Letters **116**, 145001 (2016).
http://dx.doi.org/10.1103/PhysRevLett.116.145001

- F. Pucci, C. Vasconez, **O. Pezzi**, S. Servidio, F. Valentini, W.H. Matthaeus and F. Malara.
From Alfvén waves to kinetic Alfvén waves in an inhomogeneous equilibrium structure, Journal of Geophysical Research: Space Physics **121**, 1024–1045 (2016).
http://dx.doi.org/10.1002/2015JA022216

- **O. Pezzi**, E. Camporeale and F. Valentini.
Collisional effects on the numerical recurrence in Vlasov-Poisson simulations, Physics of Plasmas **23**, 022013 (2016).
Featured Article in the February 2016 Issue of Physics of Plasmas.
http://dx.doi.org/10.1063/1.4940963

- **O. Pezzi**, F. Valentini and P. Veltri.
  Nonlinear regime of electrostatic waves propagation in presence of electron electron collisions, Physics of Plasmas **22**, 042112 (2015).
  http://dx.doi.org/10.1063/1.4919034

- **O. Pezzi**, F. Valentini and P. Veltri.
  Collisional relaxation: Landau versus Dougherty operator, Journal of Plasma Physics **81 (1)**, 305810107 (2015).
  http://dx.doi.org/10.1017/S0022377814000877

- **O. Pezzi**, F. Valentini and P. Veltri.
  Kinetic ion-acoustic solitary waves in collisional plasmas, European Physical Journal D **68 (5)**, 128 (2014).
  http://dx.doi.org/10.1140/epjd/e2014-50121-8

- **O. Pezzi**, F. Valentini, D. Perrone and P. Veltri.
  Erratum: "Eulerian simulations of collisional effects on electrostatic plasma waves" [Phys. Plasmas 20, 092111 (2013)], Physics of Plasmas **21**, 019901 (2014).
  http://dx.doi.org/10.1063/1.4863425

- **O. Pezzi**, F. Valentini, D. Perrone and P. Veltri.
  Eulerian simulations of collisional effects on electrostatic plasma waves, Physics of Plasmas **20**, 092111 (2013).
  http://dx.doi.org/10.1063/1.4821613

Contributions in international conferences

Invited oral presentations

- **O. Pezzi**.
  Da Vincenzo Ferraro ai giorni nostri: un viaggio nella complessitá (e nella bellezza) della fisica dello spazio. Premio Vincenzo Ferraro "Una vita per la scienza" VI edizione, October 8 2016. Sorrento (NA), Italy.

- **O. Pezzi**, F. Valentini, S. Servidio, D. Perrone, A. Greco, K. Osman, F. Califano, W.H. Matthaeus and P. Veltri.
  Kinetic effects in Vlasov turbulent plasmas. Solar Heliospheric and Interplanetary Environment (SHINE), July 5 – 10 2015. Stowe, Vermont, US.

- P. Veltri, F. Valentini, S. Servidio, D. Perrone, **O. Pezzi**, B. Maruca, K. Osman, F. Califano and W.H. Matthaeus.
  Kinetic Kinetic effects in Solar Wind low frequency Turbulence: Vlasov Simulations vs Data Analysis. 100-th Congresso Nazionale, Società Italiana di Fisica, September 22–26 2014. Pisa, Italy. (speaker: P. Veltri)

- P. Veltri, F. Valentini, S. Servidio, D. Perrone, **O. Pezzi**, B. Maruca, F. Califano and W.H. Matthaeus.
  Kinetic Effects in Solar Wind Low Frequency Turbulence: Vlasov Simulations vs data Analysis. Dynamical Processes in Space and Astrophysical Plasmas, March 16–22 2014. Ein Bokek, Dead Sea, Israel. (speaker: P. Veltri)

Oral presentations

- D. Perrone, F. Valentini, S. Servidio, S. Stabile, **O. Pezzi**, L. Sorriso-Valvo, R. De Marco, F. Marcucci, D. Brienza, R. Bruno, B. Lavraud, A. Retinò, A. Vaivads, G. Consolini, J. De Keyser, M. Salatti and P. Veltri.
  Differential kinetic physics of solar-wind minor ions. EGU European Geosciences Union General Assembly 2017, April 23 – 28 2017. Vienna, Austria. (speaker: D. Perrone)

- **O. Pezzi**, S. Servidio, F. Valentini, T.N. Parashar, C.V. Vasconez, Y. Yang, F. Malara, W.H. Matthaeus and P. Veltri.
  Alfvénic wave packet collisions in a kinetic plasma. Arcetri 2016 Workshop on Plasma Astrophysics, October 17 – 20 2016. University of Florence, Florence, Italy.

- **O. Pezzi**, F. Valentini and P. Veltri.
  Collisional relaxation of fine velocity structures in plasmas. SIF 2016, September 26 – 30 2016. Padova, Italy.

- F. Pucci, C.L. Vasconez, **O. Pezzi**, S. Servidio, F. Valentini, W.H. Matthaeus and F. Malara.
  From Alfvén waves to kinetic Alfvén waves in an inhomogeneous equilibrium structure. VLASOVIA 2016, May 30 – June 2 2016. Copanello (CZ), Italy.

- **O. Pezzi**, S. Servidio, T. Parashar, C.V. Vasconez, F. Valentini, F. Malara, W.H. Matthaeus and P. Veltri.
  Collisions of two Alfvénic wave packets: beyond the Moffatt-Parker problem. VLASOVIA 2016, May 30 – June 2 2016. Copanello (CZ), Italy.

- **O. Pezzi**, E. Camporeale and F. Valentini.
  Fine velocity structures collisional dissipation in plasmas. EGU European Geosciences Union General Assembly 2016, April 17 – 22 2016. Vienna, Austria.

- **O. Pezzi**, S. Servidio, T.N. Parashar, Y. Yang, F. Valentini, F. Malara, W.H. Matthaeus and P. Veltri.
  Collisions of two Alfvénic wave packets in a kinetic plasma. Arcetri 2015 Workshop on Plasma Astrophysics, November 9 – 12 2015. University of Florence, Florence, Italy.

- **O. Pezzi**, F. Valentini and P. Veltri.
  Collisional relaxation: Landau versus Dougherty operator. Arcetri 2014 Workshop on Plasma Astrophysics, October 27 – 30 2014. University of Florence, Florence, Italy.

- **O. Pezzi**, F. Valentini and P. Veltri.
  Collisional effects on ion-acoustic solitary waves propagation, International Conference on Plasma Physics (ICPP), September 15 – 19 2014. Lisbon, Portugal.

- **O. Pezzi**, F. Valentini, D. Perrone and P. Veltri.
  Numerical approach to collisional plasmas: collisional effects on electrostatic plasma waves. VLASOVIA, November 25 – 28 2013. Nancy, France.

- F. Valentini, S. Servidio, D. Perrone, **O. Pezzi**, B. Maruca, F. Califano, W. H. Matthaeus and P. Veltri.
  Kinetic effects in the turbulent solar wind: capturing ion physics with a Vlasov code. VLASOVIA, November 25 – 28 2013. Nancy, France. (speaker: F. Valentini).

Poster presentations

- R. De Marco, F. Marcucci, D. Brienza, R. Bruno, G. Consolini, D. Perrone, F. Valentini, S. Servidio, S. Stabile, **O. Pezzi**, L. Sorriso-Valvo, B. Lavraud, J. De Keyser, A. Retinò, A. Fazakerley, R. Wicks, A. Vaivads, M. Salatti and P. Veltri.
  Kinetic features revealed by top-hat electrostatic analysers: numerical simulations and instrument response results. EGU European Geosciences Union General Assembly 2017, April 23 – 28 2017. Vienna, Austria.

- **O. Pezzi**, S. Servidio, F. Valentini, T.N. Parashaar, F. Malara, W.H. Matthaeus and P. Veltri.
  Collisions of two Alfvénic wave packets in a kinetic plasma. AGU Fall Meeting 2016, December 12 – 16 2016. San Francisco, California, US.

- C.L. Vasconez, F. Valentini, **O. Pezzi**, S. Servidio, F. Malara and F. Pucci.
  Numerical study of the transition to kinetic turbulence induced by large-amplitude Kinetic Alfvén fluctuations. AGU Fall Meeting 2016, December 12 – 16 2016. San Francisco, California, US.

- M. Viviani, **O. Pezzi**, F. Valentini and P. Veltri.
  Electrostatic waves in a weakly collisional plasma: analytical and nu-

merical study. VLASOVIA 2016, May 30 – June 2 2016. Copanello (CZ), Italy.

- K. Pommois, G. Brunetti, **O. Pezzi** and F. Valentini.
  Slow electrostatic fluctuations generated by beam-plasma interactions. VLASOVIA 2016, May 30 – June 2 2016. Copanello (CZ), Italy.

- **O. Pezzi**, E. Camporeale and F. Valentini.
  Collisional effects on the numerical recurrence in Vlasov-Poisson simulations. VLASOVIA 2016, May 30 – June 2 2016. Copanello (CZ), Italy.

- **O. Pezzi**, F. Valentini and P. Veltri. *Collisional relaxation of fine velocity structures in plasmas.* VLASOVIA 2016, May 30 – June 2 2016. Copanello (CZ), Italy.

- G. Brunetti, F. Valentini, **O. Pezzi** and P. Veltri.
  A Vlasov-Ampére solver for the simulation of unmagnetized collisionless plasmas with open boundary conditions. VLASOVIA 2016, May 30 – June 2 2016. Copanello (CZ), Italy.

- G. Alí, G. Mascali, **O. Pezzi** and F. Valentini.
  Extended hydrodynamical models for plasmas. VLASOVIA 2016, May 30 – June 2 2016. Copanello (CZ), Italy.

- **O. Pezzi**, T.N. Parashar, S. Servidio, F. Valentini, F. Malara, W.H. Matthaeus and P. Veltri.
  Alfvénic wave packets collision in a kinetic plasma. EGU European Geosciences Union General Assembly 2016, April 17 – 22 2016. Vienna, Austria.

- F. Pucci, C. Vasconez, **O. Pezzi**, S. Servidio, F. Valentini, W.H. Matthaeus and F. Malara.
  From Alfvén waves to kinetic Alfvén waves in an inhomogeneous equilibrium structure. EGU European Geosciences Union General Assembly 2016, April 17 – 22 2016. Vienna, Austria.

- **O. Pezzi**, E. Camporeale and F. Valentini.
  Collisional effects in weakly collisional plasmas: nonlinear electrostatic waves and recurrence phenomena. AGU Fall Meeting 2015, December 14 – 18 2015. San Francisco, California, US.

- **O. Pezzi**, F. Valentini and P. Veltri.
  Nonlinear regime of electrostatic waves propagation in presence of electron -electron collisions. Solar Heliospheric and Interplanetary Environment (SHINE), July 5 – 10 2015. Stowe, Vermont, US.

Other contributes

- F. Valentini, S. Servidio, A. Vecchio, D. Perrone, **O. Pezzi**, B. Maruca, F. Califano, W. H. Matthaeus, K. Osman and P. Veltri.
  Il vento solare: un laboratorio di Fisica dei Plasmi a multi-scala. Internal seminar, April 15th 2014. Unical, Rende (CS), Italy. (speaker: F. Valentini).

- L. Sorriso–Valvo, **O. Pezzi** and T. Alberti.
  L'astrofisica all'Unical: dal Sole allo spazio profondo.
  Giornata dell'Orientamento, April 3rd 2014. Unical, Rende (CS), Italy.